

Accounting for Aerosol Scattering in the Remote
Sensing of Greenhouse Gas

Thesis by
Qiong Zhang

In Partial Fulfillment of the Requirements for the degree of
Doctor of Philosophy

The logo for the California Institute of Technology (Caltech), featuring the word "Caltech" in a bold, orange, sans-serif font.

CALIFORNIA INSTITUTE OF TECHNOLOGY

Pasadena, California

2017

(Defended June 6th, 2016)

To my family.

© 2016

Qiong Zhang

ORCID: 0000-0002-8762-0557

ACKNOWLEDGEMENTS

My study experience at Caltech has been rewarding, challenging, and full of fun. It is almost impossible for me to generate a complete list of the people to whom I want to extend my gratitude.

First of all, I would thank my advisor, Prof. Yuk Yung. Prof. Yung is not only a great mentor in science and research, but also a mentor in life philosophy. I feel lucky to join his group and learn from a broad range of research topics. I also thank my former undergraduate advisor, Prof Yongyun Hu.

This thesis could not have been completed without the generous help from my committee. I thank Prof Paul Wennberg for providing many helpful suggestions on my research. Thank Prof Andy Thompson for showing me the fascinating world of oceanography and advising my second research project on submesoscale dynamics. I learned a lot from Prof Simona Bordini on atmospheric dynamics. Thank Prof Christian Frankenberg for joining my committee on a short notice.

Yuk group has been a great source of help and support in my research. Dr. Run-Lie Shia solved all my problems that other people could not solve. Dr. Sally Newman taught me how atmospheric laboratory measurements work and where the data come from. I benefit a lot from the discussions with Yuk group students Siteng Fan, Peter Gao, Josh Kammer, Pushkar Kopparla, Mike Line, Mike Wong, Xi Xi, and Zhaocheng Zeng. King-Fai Li, Cheng Li and Xi Zhang gave my tremendous help to start my first project at Caltech. Also, I thank JPL

scientists Dr. Stanley Sander, Vijay Natraj, and Shuhui Wang for their help and guidance in my research.

I spent four joyful years with my friends at Caltech. On my first day at Caltech, Cheng Li and Zhihong Tan picked up from LAX and helped me settle down. Senior students like Jinqiang Chen, Da Yang, and Xuan Zhang have been my role models of how to be a successful Caltech PhD. I thank other ESE students in my year, Clement Cid, Ho-Hsuan Wei, and Sally Zhang for many helpful discussions and collaborations in course work and research. Thank my officemates, Dana Anderson, Peters Buhler, Peter Gao, Henry Ngo, and Lu Pan for bringing so much fun. I would also thank Maolin Ci, Liling Gu, Jiaqi Li, and Kevin Linghu for their help in job hunting.

I want to thank our administrative staff in ESE and PS for their help in my study. Thank Irma Black, Liz Boyd, Margaret Carlos, Nora Oshima, and Ulrika Terrones. I also thank Mike Black and Scott Dungan for solving my numerous troubles with computer and software. Thank Laura Kim and Daniel Yoder from Caltech ISP for their help to foreign students. Thank Mandy Casani from Caltech CDC for career and resume consulting.

Finally, I thank my parents for their constant support. This thesis is dedicated to them.

ABSTRACT

This thesis includes three different projects related to the remote sensing of Earth's atmosphere. The first part, comprising Chapter 2 and Chapter 3, focuses on the retrieval of Level 1 product, particularly the effect of aerosol scattering in the remote sensing of greenhouse gases. In Chapter 2, we study the aerosol induced bias in the retrieval of column averaged CO₂ mixing ratios (X_{CO_2}). Ground based remote sensing data from the California Laboratory for Atmospheric Remote Sensing Fourier Transform Spectrometer (CLARS-FTS) are used. We employ a numerical radiative transfer model to simulate the impacts of neglecting aerosol scattering on the CO₂ and O₂ slant column densities (SCDs) operationally retrieved from CLARS-FTS measurements. These simulations show that the CLARS-FTS operational retrieval algorithm likely underestimates CO₂ and O₂ abundances over the LA basin in scenes with moderate aerosol loading. The bias in the CO₂ and O₂ abundances due to neglecting aerosol scattering cannot be canceled by ratioing each other in the derivation of the operational product of X_{CO_2} . We propose a method for approximately correcting the aerosol-induced bias. Results for CLARS X_{CO_2} are compared to the direct-sun X_{CO_2} retrievals from a nearby Total Carbon Column Observing Network (TCCON) station.

In Chapter 3, we explain why large X_{CO_2} retrieval errors are found over deserts in the space borne Orbiting Carbon Observatory-2 (OCO-2) data. We argue that these errors are caused by the surface albedo being close to a critical surface albedo (α_c). Over a surface with albedo close to α_c , increasing the aerosol optical depth (AOD) does not change the continuum radiance. The spectral signature caused by changing the AOD is identical to that caused by changing the absorbing gas column. The degeneracy in the retrievals of AOD and X_{CO_2}

results in a loss of degrees of freedom (DOF) and information content (H). We employ a radiative transfer model to study the physical mechanism of X_{CO_2} retrieval error over a surface with albedo close to α_c . Based on retrieval tests over surfaces with different albedos, we conclude that over a surface with albedo close to α_c , the X_{CO_2} retrieval suffers from a significant loss of accuracy.

The second part, mainly in Chapter 4, focuses on the application of Level 2 product. In this Chapter, we examine the uncertainties in middle atmospheric HO_x chemistry by comparing the Aura Microwave Limb Sound (MLS) OH and HO_2 measurements with the simulations of the Caltech-JPL KINETICS photochemical model. The model using the standard chemical kinetics underestimates OH and HO_2 concentrations in the mesosphere. To resolve the discrepancies, we use MLS OH and HO_2 measurements as benchmark to adjust the involved chemical rate coefficients within reasonable uncertainty ranges with an optimal estimation algorithm. The results show that four key reaction rate constants and the O_2 cross section at Lyman- α (121.6 nm) are the most sensitive parameters for determining the HO_x profiles. We conclude that the rate coefficient of $\text{H} + \text{O}_2 + \text{M} \rightarrow \text{HO}_2 + \text{M}$ requires a very large adjustment beyond the uncertainty limits recommended in the NASA Data Evaluation, which suggests the need for future laboratory measurements. An alternative explanation is that radiative association plays a significant role in this process, i.e. $\text{H} + \text{O}_2 \rightarrow \text{HO}_2 + h\nu$, which has never been measured or computed.

In the Appendix, we put in a Chapter based on my work with Prof. Andrew Thompson on ocean submesoscale turbulence.

PUBLISHED CONTENT AND CONTRIBUTIONS

1. **Zhang, Q.**, K-F. Li, S. Wang, S. P. Sander and Y. L. Yung (2016), Resolving Model-Observation Discrepancy in the Mesospheric and Stratospheric HO_x Chemistry. *Journal of Geophysical Research - Atmosphere*, submitted. Q.Z. participated in the conception of the project, and wrote the manuscript.
2. **Zhang, Q.**, A. F. Thompson, and A. Lazar (2016), Submesoscale Turbulence over a Topographic Slope. *Ocean Modelling*, submitted. Q.Z. did the modelling, analyzed the model output, and wrote a large part of the manuscript.
3. Zeng, Z-C, **Q. Zhang**, J. Margolis, R-L. Shia, S. Newman, D. Fu, K-W. Wong, T. Pongetti, S. P. Sander, P. O. Wennberg, and Y. L. Yung (2016), Investigating Wavelength-Dependent Aerosol Optical Properties Using Water Vapor Slant Column Retrievals from CLARS over the Los Angeles Basin. *Atmospheric Chemistry and Physics*, submitted. QZ did a part of the data analysis.
4. Li, K-F., **Q. Zhang**, K-K. Tung, and Y. L. Yung (2016), Standard Ozone Photochemistry Survives an Observational Challenge on Decadal Time Scales. *Nature Climate Change*, submitted. Q.Z. helped with the modelling of ozone uncertainties.
5. **Zhang, Q.**, R-L. Shia, S. P. Sander and Y. L. Yung (2016), X_{CO₂} Retrieval Error over Deserts near Critical Surface Albedo. *Earth and Space Science*, doi: 10.1002/2015EA000143. Q.Z. participated in the conception of the project, and wrote the manuscript.

6. Wang, S., **Q. Zhang**, L. Millan, K-F. Li, Y. Yung, S. Sander, N. Livesey, M. Santee (2015), First Evidence of Middle Atmospheric HO₂ Response to 27-day Solar Cycles from Satellite Observations. *Geophysical Research Letter*, doi: 10.1002/2015GL065237. Q.Z. did a part of the MLS data analysis and statistical significance test.
7. **Zhang, Q.**, V. Natraj, K-F Li, R-L. Shia, D. Fu, T. J. Pongetti, S. P. Sander and Y. L. Yung (2015), Accounting for Aerosol Scattering in the CLARS Retrieval of Column Averaged CO₂ Mixing Ratios. *Journal of Geophysical Research - Atmosphere*, doi: 10.1002/2015JD023499. Q.Z. participated in the conception of the project, and wrote the manuscript.
8. Xi, X, V. Natraj, R. L. Shia, M. Luo, **Q. Zhang**, S. Newman, S. Sander, and Y. L. Yung (2015), Simulated Retrievals for the Remote Sensing of CO₂, CH₄, CO, and H₂O from Geostationary Orbit. *Atmospheric Measurement Techniques*, doi:10.5194/amtd-8-5809-2015. Q.Z. helped with the model and retrieval algorithm.

TABLE OF CONTENTS

Acknowledgements.....	iii
Abstract	v
Published Content and Contributions.....	vii
Table of Contents.....	ix
List of Figures.....	xi
List of Tables.....	xii
Chapter I: Introduction	2
Chapter II: Accounting for Aerosol Scattering in the CLARS Retrieval of Column Averaged CO ₂ Mixing Ratios	11
Introduction.....	11
Underestimation of SCDs due to aerosol scattering.....	13
Influence of aerosols on the observed radiance.....	17
Measurement bias caused by aerosol scattering.....	20
Bias correction.....	28
Validation.....	35
Discussions and conclusions	40
Appendix: Two-stream analytic model.....	43
Bibliography	48
Chapter III: X _{CO₂} Retrieval Error over Deserts near Critical Surface Albedo	53
Introduction.....	53

X _{CO2} retrieval errors over deserts	55
Radiative transfer modeling	63
Discussions and conclusions	70
Bibliography	74
Chapter IV: Resolving Model-Observation Discrepancy in the Mesospheric and Stratospheric HO _x Chemistry	80
Introduction.....	80
Model and method.....	83
Results.....	92
Discussion and Conclusion	96
Supplementary material.....	102
Bibliography	107
Appendix.....	112

LIST OF FIGURES

Figure 1.1 GHG concentration and emission [<i>IPCC</i> , 2014]	3
Figure 1.2 OCO-2 retrieval algorithm [<i>O'Dell et al.</i> , 2012]	5
Figure 2.1 Schematic figure of CLARS measurement	14
Figure 2.2 Variations of CLARS measured SCD	16
Figure 2.3 Spectra of the CO ₂ absorption band	19
Figure 2.4 Comparison between the simulated and measured SCD	24
Figure 2.5 Simulation results when aerosol scattering is neglected	26
Figure 2.6 Retrieval biases in CO ₂ , O ₂ , and X _{CO₂}	30
Figure 2.7 AOD bias vs. geometry	31
Figure 2.8 AOD bias vs. asymmetry parameter	33
Figure 2.9 AOD bias vs. SSA	34
Figure 2.10 Validation of CLARS West Pasadena measurements	37
Figure 2.11 CLARS West Pasadena XCO ₂ measurements vs. estimates	39
Figure 2.A1 One-line spectra simulated by the analytic model	47
Figure 3.1 Global map of OCO-2 X _{CO₂} retrieval	56
Figure 3.2 Schematic figures of reflection and scattering	57
Figure 3.3 Global map of surface albedo	59
Figure 3.4 Global map of AOD	61
Figure 3.5 Spectra and critical surface albedo	64
Figure 3.6 Jacobians of CO ₂ and AOD in a single line	67
Figure 3.7 X _{CO₂} retrieval error as a function of surface albedo	72

Figure 4.1 Comparison between MLS measurements and model.....	84
Figure 4.2 Jacobians of OH.....	87
Figure 4.3 Jacobians of HO ₂	88
Figure 4.4 Jacobians of the selected reactions	91
Figure 4.5 O ₂ cross section and its jacobians.....	92
Figure 4.6 Jacobians with respect to the radiative association reaction.....	97
Figure 4.7 H ₂ O and O ₃ profiles	98

LIST OF TABLES

Table 2.1 Climatological aerosol compositions.....	21
Table 3.1 Retrieval tests using the 2S-ESS model.....	68
Table 4.1 Model parameter adjustments	93

Chapter 1

INTRODUCTION

Increased understanding of the impacts of greenhouse gases (GHGs) on climate change depends critically on the measurement of their concentrations [IPCC AR5, 2013]. Urban areas, such as the megacity of Los Angeles (LA), California, are immense sources of global GHGs. These areas, which contain more than 50% of the world's population, are contributing at least 70% of fossil fuel CO₂ emissions and a large amount of anthropogenic CH₄ [Duren and Miller, 2012; Kort *et al.*, 2012]. In the past decade, satellite observations such as those from the Scanning Imaging Absorption Spectrometer for Atmospheric Chartography (SCIAMACHY), the Greenhouse Gases Observing Satellite (GOSAT), and the Orbiting Carbon Observatory-2 (OCO-2) have been proposed to measure the global distribution of CO₂ [Bovensmann *et al.*, 1999; Crisp *et al.*, 2004; Kuang *et al.*, 2002; Yokota *et al.*, 2009]. Since CO₂ is well mixed in the atmosphere, retrieval precision up to ~1 ppm is typically required for CO₂ flux inversion [Miller *et al.*, 2007]. Such data could significantly reduce the uncertainties in the regional CO₂ flux estimation [Rayner and Brien, 2001].

According to the IPCC AR5 report, there is very high confidence that current GHG concentrations have exceeded the ice core record in the past 22,000 years. The increase is mostly attributed to the anthropogenic emissions in the industrial era. Figure 1.1 shows the changes of major GHGs over the past two centuries and the

anthropogenic contribution to the total CO₂ emission. To eliminate the uncertainties in the estimation of GHG emission and future climate projections, we must make global accurate measurements and continuously monitor the GHG concentration. For this purpose, remote sensing is an ideal approach due to its high sampling frequency and wide coverage.

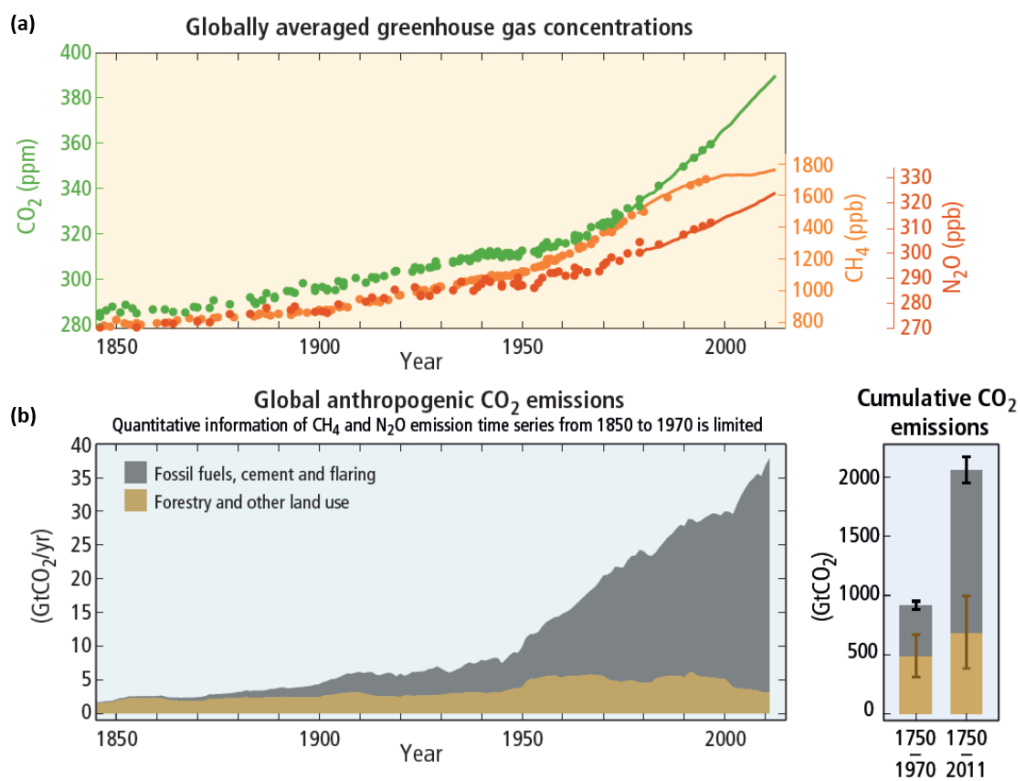


Figure 1.1. (a) Atmospheric concentrations of the greenhouse gases carbon dioxide (CO₂, green), methane (CH₄, orange) and nitrous oxide (N₂O, red) determined from ice core data (dots) and from direct atmospheric measurements (lines). (d) Global anthropogenic CO₂ emissions from forestry and other land use as well as from burning of fossil fuel, cement production and flaring. [IPCC, 2004]

Figure 1.2 illustrates the retrieval algorithm currently used by the OCO-2 mission. The retrieval process starts with Level 1B product, which is the calibrated spectral radiance measured from space. The “pre-screening” process removes data of poor quality or contaminated with large aerosol/cloud optical depth. Then, other external data, such as pointing geometry, atmospheric profile and gas absorption coefficients are used by the radiative transfer model to compute the simulated spectral radiance. In the inverse model, the statevector is updated until the simulated radiance matches the measurement and the retrieval converges. The optimal estimation of the statevector is achieved by minimizing the cost function as in Equation 1.1.

$$\chi^2 = [x_i - x_a]^T \mathbf{S}_a^{-1} [x_i - x_a] + [y - \mathbf{F}(x_i)]^T \mathbf{S}_e^{-1} [y - \mathbf{F}(x_i)] \quad (1.1)$$

where x_a is the statevector, $\mathbf{F}(x)$ is the forward model, y is the measurement, \mathbf{S}_a is the *a priori* covariance matrix, and \mathbf{S}_e is the measurement error covariance matrix [Rodgers, 2000].

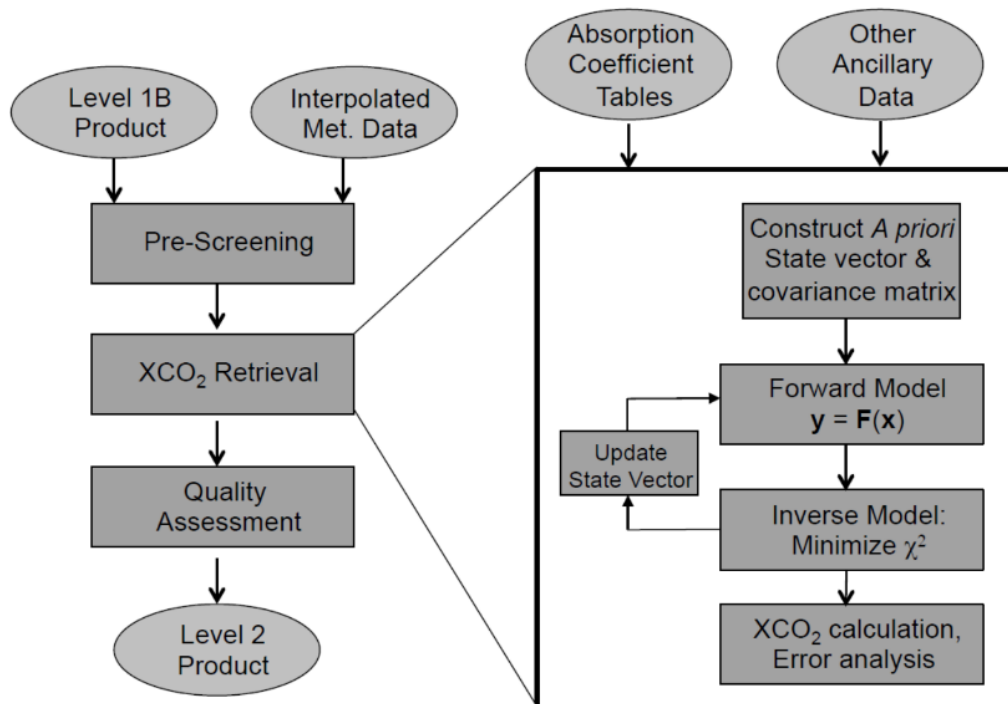


Figure 1.2. OCO-2 retrieval algorithm [O'Dell *et al.*, 2012]. Level 2 product is retrieved from the Level 1B spectra by minimizing the cost function. The forward model in the retrieval algorithm relies on many external parameters such as the absorption coefficient table, observation geometry, and aerosol optical properties.

Aerosol scattering is often considered the major source of error in the remote sensing of GHGs [Aben *et al.*, 2007]. Scattering in the atmosphere could change the photon path distribution, thus altering the apparent absorption of the target trace gas [Oshchepkov *et al.*, 2008]. Operational trace gas retrieval algorithms for space missions often apply simplified aerosol models due to the lack of information to constrain a large number of aerosol parameters [Frankenberg *et al.*, 2012; Guerlet *et al.*, 2013]. To mitigate the impacts of imperfect aerosol/cloud modeling, these retrieval algorithms perform target scene screening that filters out those observations

contaminated by large aerosol and cloud optical depths (AOD/COD). For OCO-2 mission, AOD = 0.3 is a typical threshold [O'Dell *et al.*, 2012]. The filtering is often imperfect as it depends on many parameters such as viewing and solar geometries, AOD, aerosol type, and aerosol height [O'Dell *et al.*, 2012; Oshchepkov *et al.*, 2012]. Over megacities where aerosols often reside in the urban planetary boundary layer (PBL), a large portion of remote sensing measurements from space are usually filtered out by pre- or post-screening [Crisp *et al.*, 2012; Yoshida *et al.*, 2011]. Hence, there exists a need to fill this “gap” in the satellite measurement databases, e.g., the source areas that significantly contribute to the global GHG emissions. Deserts are also associated with large aerosol loading. Previous studies [e.g., Houweing *et al.*, 2005] have suggested potential problems in the retrieval of GHG over such regions.

This thesis studies the effect of aerosol scattering in the remote sensing of GHG using both ground based and space borne measurements. Both ground-based and space-borne measurements are used. Their goal is to understand how aerosol scattering impacts the measurements of trace gas column abundances and mixing ratios, how to correct for the error caused by aerosols, and how aerosol scattering effect interacts with surface properties.

The remote sensing data processing is often divided into two levels. While the next two Chapters focus on the retrieval of Level 1 product, Chapter 4 is a separate section which focuses on the application of Level 2 retrieval product in calibrating a photochemical model. In this Chapter, we compare the Microwave Limb Sounder (MLS) measurements of odd hydrogen (HO_x) species, including hydroxyl radical (OH) and hydroperoxyl (HO_2) with the simulations of the Caltech-JPL KINETICS

photochemical model. HO_x species are of great interests to the climate community because they are important catalysts for the dissociation of O₃ in the middle atmosphere. Our study indicates that accurate measurements of photochemical rate coefficients and molecular cross sections are crucial in simulating stratospheric and mesospheric HO_x chemistry. High quality satellite observations can be used to constrain or retrieve photochemical parameters and help improve our understanding of atmospheric chemistry.

Bibliography:

- Aben, I., O. Hasekamp, and W. Hartmann (2007), Uncertainties in the space-based measurements Of CO₂ columns due to scattering in the Earth's atmosphere, *J Quant Spectrosc Ra*, 104(3), 450-459, doi:DOI 10.1016/j.jqrst.2006.09.013.
- Bovensmann, H., J. P. Burrows, M. Buchwitz, J. Frerick, S. Noel, V. V. Rozanov, K. V. Chance, and A. P. H. Goede (1999), SCIAMACHY: Mission objectives and measurement modes, *J Atmos Sci*, 56(2), 127-150, doi:Doi 10.1175/1520-0469(1999)056<0127:Smoamm>2.0.Co;2.
- Crisp, D., et al. (2004), The orbiting carbon observatory (OCO) mission, *Adv Space Res-Series*, 34(4), 700-709, doi:DOI 10.1016/j.asr.2003.08.062.
- Crisp, D., et al. (2012), The ACOS CO₂ retrieval algorithm - Part II: Global X-CO₂ data characterization, *Atmos Meas Tech*, 5(4), 687-707, doi:DOI 10.5194/amt-5-687-2012.
- Frankenberg, C., O. Hasekamp, C. O'Dell, S. Sanghavi, A. Butz, and J. Worden (2012), Aerosol information content analysis of multi-angle high spectral resolution measurements and its benefit for high accuracy greenhouse gas retrievals, *Atmos Meas Tech*, 5(7), 1809-1821, doi:DOI 10.5194/amt-5-1809-2012.
- Guerlet, S., et al. (2013), Impact of aerosol and thin cirrus on retrieving and validating XCO₂ from GOSAT shortwave infrared measurements, *J Geophys Res-Atmos*, 118(10), 4887-4905, doi:Doi 10.1002/Jgrd.50332.
- Houweling, S., Hartmann, W., Aben, I., Schrijver, H., Skidmore, J., Roelofs, G.J.,

- Breon, F.M., 2005. Evidence of systematic errors in SCIAMACHY-observed CO₂ due to aerosols. *Atmospheric Chemistry and Physics* 5, 3003-3013.
- IPCC (2013), *Climate Change, the Fifth Assessment Report (AR5) of the United Nations Intergovernmental Panel on Climate Change*, Intergovernmental Panel on Climate Change.
- Kuang, Z. M., J. Margolis, G. Toon, D. Crisp, and Y. Yung (2002), Spaceborne measurements of atmospheric CO₂ by high-resolution NIR spectrometry of reflected sunlight: An introductory study, *Geophys Res Lett*, 29(15), doi:Artn 1716Doi 10.1029/2001gl014298.
- Miller, C. E., et al. (2007), Precision requirements for space-based X-CO₂ data, *J Geophys Res-Atmos*, 112(D10), doi:Artn D10314Doi 10.1029/2006jd007659.
- O'Dell, C. W., et al. (2012), The ACOS CO₂ retrieval algorithm - Part 1: Description and validation against synthetic observations, *Atmos Meas Tech*, 5(1), 99-121, doi:DOI 10.5194/amt-5-99-2012.
- Oshchepkov, S., A. Bril, and T. Yokota (2008), PPDF-based method to account for atmospheric light scattering in observations of carbon dioxide from space, *J Geophys Res-Atmos*, 113(D23), doi:Artn D23210Doi 10.1029/2008jd010061.
- Oshchepkov, S., et al. (2012), Effects of atmospheric light scattering on spectroscopic observations of greenhouse gases from space: Validation of PPDF-based CO₂ retrievals from GOSAT, *J Geophys Res-Atmos*, 117, doi:Artn D12305Doi 10.1029/2012jd017505.

Rodgers, C. D. (2000), *Inverse Methods for Atmospheric Sounding: Theory and Practice*, World Scientific Publishing Co. Pte. Ltd.

Yokota, T., Y. Yoshida, N. Eguchi, Y. Ota, T. Tanaka, H. Watanabe, and S. Maksyutov (2009), Global Concentrations of CO₂ and CH₄ Retrieved from GOSAT: First Preliminary Results, *Sola*, 5, 160-163, doi:DOI 10.2151/sola.2009-041.

Yoshida, Y., Y. Ota, N. Eguchi, N. Kikuchi, K. Nobuta, H. Tran, I. Morino, and T. Yokota (2011), Retrieval algorithm for CO₂ and CH₄ column abundances from short-wavelength infrared spectral observations by the Greenhouse gases observing satellite, *Atmos Meas Tech*, 4(4), 717-734, doi:DOI 10.5194/amt-4-717-2011.

Chapter 2

ACCOUNTING FOR AEROSOL SCATTERING IN THE CLARS RETRIEVAL OF COLUMN AVERAGED CO₂ MIXING RATIOS.

2.1. Introduction

To measure GHG concentrations in LA, CLARS-FTS was deployed on the top of Mt. Wilson, looking down at the land surface of target sites in the LA basin [see *Fu et al.*, 2014; *Wong et al.*, 2014 and references therein]. The current CLARS-FTS operational retrieval algorithm (version 1.0) uses measurements of the CO₂ absorption band centered at 1.61 μm to estimate the CO₂ slant column density (SCD) along the line of sight. SCD is defined as the total number of absorbing gas molecules along the optical path per unit area. A modified version of the GFIT program is used in the retrieval [*Fu et al.*, 2014]. The GFIT program was originally used for observing direct sunlight [*Toon et al.*, 1992; *Wunch et al.*, 2011]. Surface reflection is included in the modified version but aerosol scattering is not taken into account. The effect of scattering, on the other hand, is estimated by simultaneously retrieving the O₂ SCD based on measurements of the O₂ absorption band centered at 1.27 μm , assuming that the changes in light path due to aerosol scattering are identical in both the 1.61 μm and 1.27 μm bands. The bias due to aerosol scattering could be mitigated by estimating the column-averaged dry air mole fraction of CO₂ (X_{CO_2}) defined as follows:

$$X_{CO_2} = 0.2095 \frac{SCD_{CO_2}}{SCD_{O_2}} \quad (2.1)$$

This algorithm was designed for retrieving X_{CO_2} in clear sky conditions. However, in the presence of haze, it leads to an underestimation of CO_2 and O_2 SCDs due to the change in photon path length through the boundary layer [Oshchepkov *et al.*, 2012], which is not accounted for in the retrieval. The wavelength and species dependence of aerosol scattering also implies that division by O_2 SCD does not completely remove the aerosol scattering effect in the $1.61 \mu m$ CO_2 absorption band. Therefore, the assumption that aerosol scattering is identical in the two bands leads to an observable bias in the retrieved X_{CO_2} . The CLARS operational algorithm ignores aerosols and instead uses a filter criterion in which data are filtered out if the retrieved and geometric O_2 SCD values differ by more than 10% [Wong *et al.*, 2015]. However, this criterion is somewhat arbitrary. In a megacity where aerosol loading is often non-negligible, it is necessary to evaluate the influence of aerosol scattering on the retrievals of CLARS-FTS measurements.

The aim of this paper is to present the CLARS observations and show the effects of aerosols scattering on the observed radiance and the retrieved absorbing gas abundances. The bias can be understood and mitigated with the help of a full-physics radiative transfer (RT) model. In Section 2.2, we first introduce the CLARS measurements and demonstrate the retrieval bias in the SCDs of CO_2 and O_2 due to neglecting aerosol scattering. In Section 2.3, we show the high resolution spectral signatures of aerosol scattering on the observed radiance using CLARS measurements and a numerical RT model. In Section 2.4, simulations are

performed using CLARS viewing geometries to illustrate how aerosol scattering causes an apparent reduction in the retrieved abundances of trace gases and how wavelength dependence of the scattering causes bias in the X_{CO_2} product. A fast and effective correction approach is presented in Section 2.5, and the results are validated using comparison between CLARS and Total Carbon Column Observing Network (TCCON) measurements in Section 2.6. A discussion of our results and conclusions follows in Section 2.7.

2.2. Underestimation of SCDs due to aerosol scattering

Here we will show the SCD retrieval bias caused by neglecting aerosol scattering. CLARS-FTS has two modes of operation as shown in Figure 2.1 [*Fu et al.*, 2014, supplementary figure 1]: (1) Los Angeles Basin Surveys (LABS) mode using reflected sunlight from the LA basin that undergoes absorption and scattering by trace gases and aerosols below the CLARS site; (2) Spectralon Viewing Observation (SVO) mode using reflected sunlight from a locally positioned Spectralon plate that samples the solar beam above the CLARS site and measures the background GHG abundances in the free troposphere above Mt. Wilson. CLARS-FTS has high sensitivity to the variation of GHGs over the LA basin due to the long light path through the urban planetary boundary layer (PBL) (typically 20 km distance from CLARS site to the LA basin land surface). In the LABS mode, this viewing geometry offers much higher sensitivity to the atmospheric composition within the PBL than a typical satellite geometry but also makes the

measurements more susceptible to the influence of aerosol scattering and absorption.

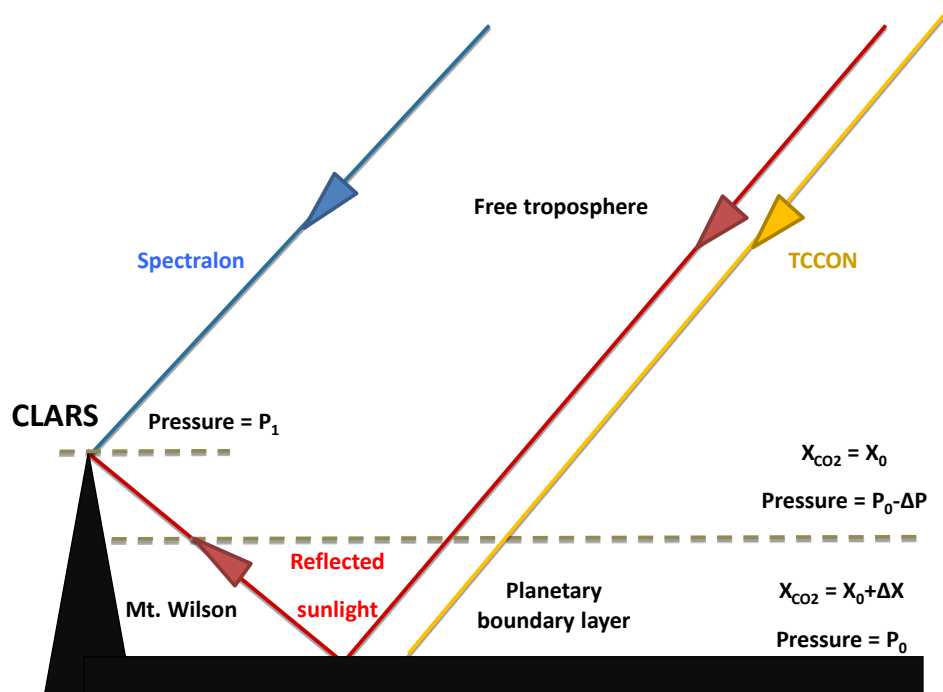


Figure 2.1. Schematic figure of CLARS measurement geometries and validation. The validation method will be presented in Section 2.6. We employ the X_{CO_2} data from the JPL TCCON station (yellow) and CLARS Spectralon (blue) to calculate the mean CO_2 mixing ratio along the West Pasadena reflected light path (red). The background CO_2 mixing ratio is X_0 , and the CO_2 mixing ratio within the PBL is $X_0 + \Delta X$. We assume that the surface pressure is P_0 , the pressure at the top of PBL is $P_0 - \Delta P$, and the pressure at the CLARS instrument is P_1 . P_0 and P_1 are known with high accuracy from the NCEP atmospheric profile.

In the LABS mode, CLARS-FTS points at a programmed sequence of ground target locations in the LA basin. Sample CO_2 SCDs to a target in West Pasadena are shown in Figure 2.2(a). For scenarios over the LA basin with moderate aerosol

loading (aerosol optical depth AOD ~ 0.1 in the $1.61 \mu\text{m}$ band), we obtain a ‘U-shape’ as the SCD of absorbing gas along the line of sight changes from the morning to the afternoon. The data are closer to the 1:1 line in the morning (A-B) and deviate from it as the haze builds up in the afternoon (B-C). For a pure trace gas absorption scenario, i.e. with no aerosol scattering in the atmosphere, we expect the measured SCD to agree with the calculated geometric SCD.

Therefore the data points, such as those in the SVO mode measurements (green "+" points in Figure 2.2), should fall on the 1:1 line. Some systematic errors in the spectroscopic parameters may exist, but their impact on the retrieval is small. For the measurements over West Pasadena, the observed CO_2 SCDs are smaller (by up to 13%) than the geometric ones from the morning to the afternoon. Figure 2.2(b) shows similar deviation (by up to 17%) in the O_2 SCDs. The deviations in CO_2 could arise from diurnal variations (i.e., changes of CO_2 emission rate over the LA basin, etc). However, there are no emission sources or sinks in the LA basin for O_2 . This suggests that the low bias is mainly due to the increase in AOD during the daytime, as indicated by the images recorded by a visible camera that was co-aligned with the CLARS-FTS. Since aerosol scattering has wavelength dependence, we expect the O_2 and CO_2 SCDs to have different deviations from the 1:1 line. Therefore, dividing the CO_2 SCD by the O_2 SCD cannot completely eliminate the bias in X_{CO_2} .

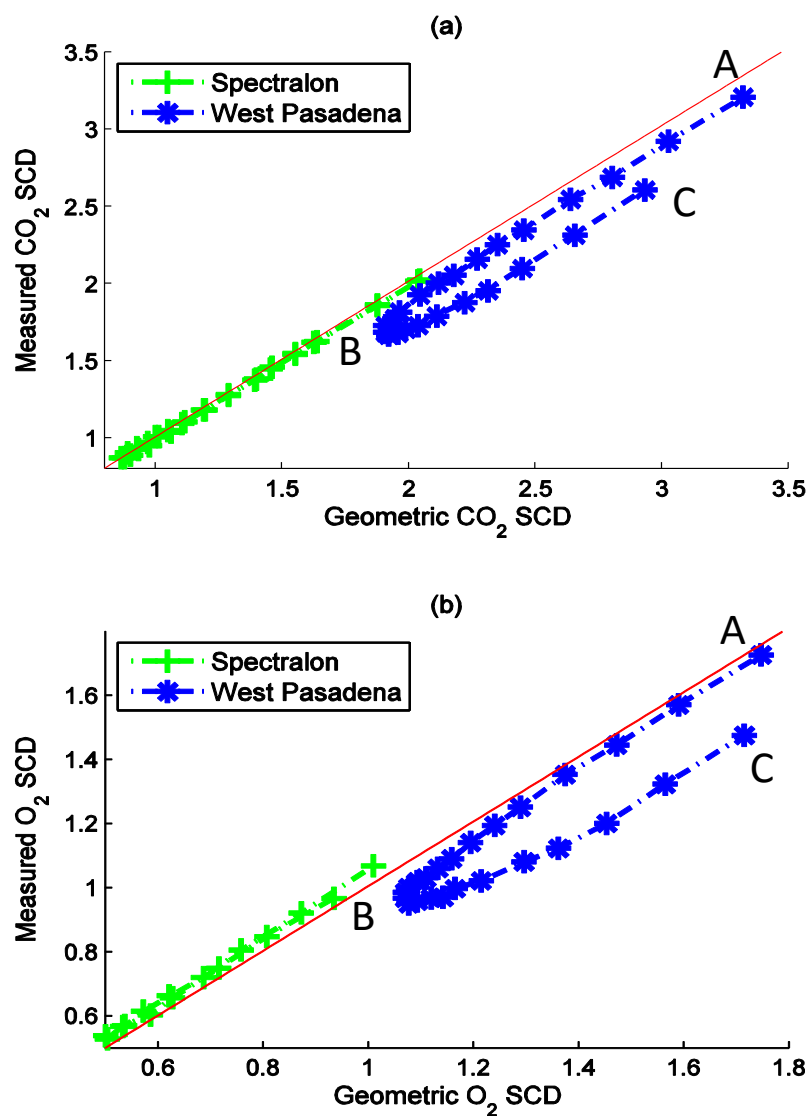


Figure 2.2. Variations of CLARS measured SCD v.s. geometric SCD from the morning to the afternoon, for (a) CO₂ and (b) O₂. A, B and C indicate morning, noon and afternoon. Units for CO₂ and O₂ SCDs are scaled by 10²² and 10²⁵ molecule/cm², respectively. SCD is defined as the total number of molecules along the light path per cm². The units represent abundances of gas molecules in the atmosphere. Geometric SCDs are calculated from the *a priori* atmospheric profiles at Spectralon and West Pasadena. The red lines indicate 1:1 correspondence between measured and geometric SCDs.

2.3. Influence of aerosols on the observed radiance

We simulate the CLARS-FTS spectral radiance using a numerically efficient two-stream-exact single scattering (2S-ESS) RT model [*Spurr and Natraj, 2011*], where the RT calculation is done analytically except for the boundary value problem (which is also done using a simple and fast pentadiagonal solver rather than typical matrix inversion techniques). The 2S-ESS RT model is also different from a typical two-stream model in that the singly scattered radiation is computed exactly (using all scattering phase function moments), the two-stream approximation is used only for the multiply scattered radiation. The exact single scattering calculation mitigates biases due to the severe phase function truncation inherent to the two-stream approximation. In this model, the *a priori* atmospheric profile has 70 layers from the surface up to 70 km, derived from NCEP-NCAR reanalysis data [*Kalnay et al., 1996*]. Absorption coefficients for all absorbing gases are obtained from the HITRAN database [*Rothman et al., 2008*]. We calculate the optical depth for each layer using the Reference Forward Model [*Dudhia et al., 2002*], and then simulate the reflected radiance observed by the CLARS-FTS. We assume the surface reflection to be Lambertian with a surface albedo of 0.23, as measured for West Pasadena [*Fu et al., 2014*]. The model takes into consideration Rayleigh scattering by air molecules. The viewing zenith angle, a constant parameter, is 83.1° for the target scene over West Pasadena. The solar zenith angle (SZA) and relative azimuth angle (AZA) at a given time can be calculated as a function of latitude, time and solar declination angle. In the forward model, we convolve the simulated radiance using the CLARS-FTS instrument line shape (ILS)

with full width at half maximum (FWHM) = 0.022 cm^{-1} [Fu *et al.*, 2014]. The spectral resolution is adjustable and the current operational value is 0.06 cm^{-1} . The corresponding instrument maximum optical path difference is 5.0 cm. The signal to noise ratio (SNR) is 300. Gaussian white noise is added to the simulated spectra.

Figure 2.3 (a) and (b) shows synthetic spectra in the $1.6\mu\text{m}$ CO_2 absorption band with different CO_2 abundances and AODs in the PBL. The spectra from the 2S-ESS RT model have been validated against a full-physics RT model VLIDORT [Spurr, 2006], which provides radiances with accuracy higher than the 2S-ESS RT model. In the presence of aerosol, the absorption lines move upward in the core and wing regions. The FWHM of the spectral lines in Figure 2.3(b) shows that the apparent absorption becomes weaker as AOD increases. Intuitively, this is because aerosol scattering shortens the photon path length and reduces absorption within the PBL. The effect is similar to decreasing CO_2 abundance in the atmosphere (Figure 2.3a), as the spectral differences in Figures 2.3 (a) and (b) have almost the same shapes. In the high-resolution CLARS-FTS spectra, this feature can be resolved for individual absorption lines. In Figure 2.3(c), two measurements from CLARS-FTS on 23 March 2013 are shown. The measurements are made in the morning (clear) and in the afternoon (hazy) with nearly identical SZAs. The AOD is estimated based on images from a co-boresighted visible camera. The spectral lines measured in the hazy scenario (red line in Figure 2.3c) move inward and show weaker absorptions, compared with the ones measured in the clear scenario (blue line in Figure 2.3c). This change in photon path length is observed in both the CLARS-FTS measured spectra

(Figure 2.3c) and the simulations (Figure 2.3b). Similarly, the same features are also apparent in the spectra of the O₂ absorption bands.

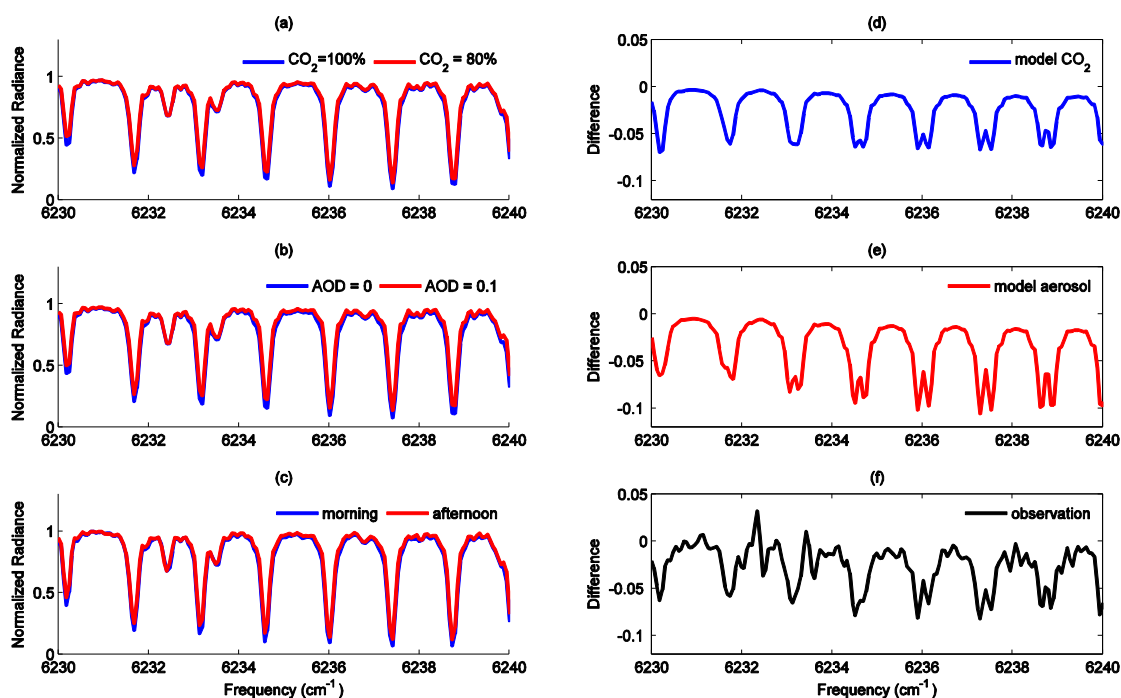


Figure 2.3. Spectra of the CO₂ absorption band. (a) Normalized radiance from the numerical model with different CO₂ abundances. CO₂ abundance is adjusted by multiplying a constant scale factor (80%) to the atmospheric profile. (b) Normalized radiance from the numerical model with different AODs in the PBL. (c) Measurements of normalized radiance from CLARS instrument on 23 March 2013. Measurements in the morning and in the afternoon have similar SZAs (65.16° vs. 64.46°) but different AODs. The right panels (d) ~ (f) are corresponding differences between the spectra in the left panels. Differences in panel (d) and (e) are proportional to the Jacobians of CO₂ scaling factor and AOD.

These features indicate that local aerosol scattering leads to a reduction in apparent absorption. Using normalized spectra, the equivalent effects in the apparent absorption, either caused by reducing absorbing gas abundance or by aerosol

scattering in the PBL, are difficult to distinguish. In a model without aerosol scattering, all the changes in line width are attributed to changes in gas abundance. We assume that the daily gas abundance variations in the LA region are much smaller than that observed in Figure 2.2 (especially for O₂). The model explains the changes in retrieved SCDs from CLARS-FTS as the AOD increases from the morning to the afternoon (Figure 2.2). The effect of aerosol scattering also increases as the SZA becomes larger in the afternoon.

To explain the differences in spectra, we also developed a one-line absorption model for CO₂ and O₂ (Appendix 2.1). Taking CO₂ as an example, Figure 2.A1 shows the calculated reflectance. In this case, the apparent absorption becomes weaker after normalization (by the maximum value of the radiance) as shown in Figure A.1 (b) for $\omega_0 = 0.99$. This suggests that the gaseous absorption is reduced by aerosol scattering. The magnitude of this effect depends on the SSA and aerosol phase function. We also calculate the reflectance with $\omega_0 = 0.2$ as shown in Figures 2.A1 (a) and 2.A1 (c). The reflectance decreases with AOD, but after normalization, we can still see the line-filling. In Figure 4(d), we obtain similar line-filling effects by reducing the concentration of CO₂ in the calculation and setting AOD in the PBL to zero. For an O₂ absorption line centered at $\nu_0 = 7863.4 \text{ cm}^{-1}$, all the features are similar in general (not shown here).

2.4. Measurement bias caused by aerosol scattering

In order to quantify the influence of aerosol scattering on the GHG retrievals and simulate the bias observed by CLARS-FTS, we assume nonzero AOD evenly

distributed in the PBL and use the 2S-ESS model to generate synthetic spectral radiance data. In a forward model with the same configuration, AOD is set to zero and held constant. The forward model is used to fit the synthetic spectra. This approach approximately simulates the influence of neglecting aerosol scattering on the retrieved SCDs. We also neglect the effect of water vapor. The fitting process employs the Levenberg-Marquardt (LM) algorithm [Rodgers, 2000]. The iteration in this algorithm is:

$$\mathbf{x}_{i+1} = \mathbf{x}_i + [(1 + \gamma)\mathbf{S}_a^{-1} + \mathbf{K}_i^T \mathbf{S}_e^{-1} \mathbf{K}_i]^{-1} \{ \mathbf{K}_i^T \mathbf{S}_e^{-1} [\mathbf{y} - \mathbf{F}(x_i)] - \mathbf{S}_a^{-1} [\mathbf{x}_i - \mathbf{x}_a] \} \quad (2.2)$$

where \mathbf{x}_a is the *a priori* state vector, \mathbf{y} is the measured spectral radiance, \mathbf{S}_a is the *a priori* covariance matrix, \mathbf{S}_e is the spectral radiance noise covariance matrix, \mathbf{K} is the Jacobian matrix, $\mathbf{F}(\mathbf{x})$ is the forward model and γ is the parameter determining the size of each iteration step. The synthetic measurements cover 25 cm^{-1} wide spectral regions in both the 1.27 μm (O_2) and 1.61 μm (CO_2) absorption bands. The state vector elements to be adjusted are the scaling factors for O_2 and CO_2 abundances. In this study, we set \mathbf{S}_a to be 10% for both O_2 and CO_2 SCD simulations. The results are not sensitive to the value of the *a priori* constraints.

To simulate the observed 'U-shape' as shown in Figure 2.2, AOD data are taken from measurements of the AERosol RObotic NETwork (AERONET) station at Caltech on 23 March 2013 [Holben *et al.*, 1998; Holben *et al.*, 2001]. AERONET measurements cover the wavelength range from 340 to 1020 nm. However, neither the CO_2 nor the O_2 near-infrared band used in our study is included in the AERONET measurements. To calculate the AOD in these two bands, we use the Angstrom exponent law to extrapolate the data [Seinfeld and Pandis, 2006]

$$\frac{\tau}{\tau_0} = \left(\frac{\lambda}{\lambda_0} \right)^{-\kappa} \quad (2.3)$$

where λ_0 and τ_0 are the reference wavelength and the corresponding AOD, and $\kappa = 0.78$ is the Angstrom exponent. Seven wavelengths from 340nm to 1020nm are used in the regression. The AOD in the CO₂ band starting at 1607 nm is 0.0708, while the AOD in the O₂ band starting at 1264 nm is 0.0854. These values are obtained from AERONET by extrapolation.

Aerosol properties in the LA basin are obtained from simulations using the Weather Research and Forecasting [WRF; *Skamarock et al., 2005*] model. The Modal Aerosol Dynamics Model/Secondary Organic Aerosol Module (MADE/SORGAM) [*Ackermann et al., 1998; Schell et al., 2001*] is used to obtain specific values for 5 aerosol types (black carbon, organic carbon, sulfate, coarse and accumulation mode sea salt). The aerosol single scattering properties are computed using the Meerhoff Mie code [*Derooij and Vanderstap, 1984*], with size distribution parameters taken from the Optical Properties of Clouds and Aerosols [OPAC; *Hess et al., 1998*] database. Table 2.1 shows the typical aerosol composition (as percentages of total optical depth) and optical parameters in this region. In the forward model, we vary the SZA and AZA to simulate different measurements from the morning to the afternoon (7:00 am to 5:00 pm). We assume that the total AOD increases from zero to the value measured by AERONET station at 4:48 pm. The temporal variation of AOD is simulated by an idealized function as shown in Equation (2.4).

$$\tau_s = \frac{AOD}{2} + \frac{AOD}{2} \tanh\left(\frac{H}{30^\circ}\right) \quad (2.4)$$

where H is the hour angle varying linearly from -75° (7:00 am) to 75° (5:00 pm). The AERONET measurement of AOD at 4:48 pm is used to constrain Equation (2.4).

Table 2.1. Climatological aerosol composition and optical properties in the LA region.

	Organic	Seasalt (accum)	Seasalt (coarse)	Soot	Sulfate
percentage	4.9%	31.7%	38.1%	7.9%	17.4%
SSA	0.872	0.998	0.985	0.040	0.999
g	0.55	0.79	0.82	0.15	0.69

[Ackermann *et al.*, 1998; Schell *et al.*, 2001]

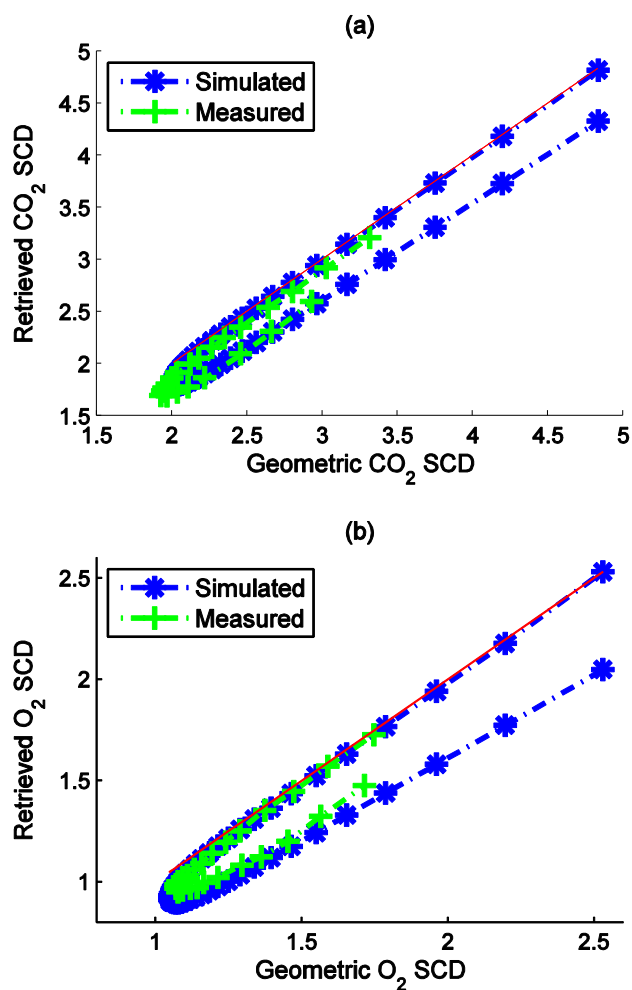


Figure 2.4. Comparison between the simulated and measured SCD daily variations on 23 March 2013 in West Pasadena for (a) CO₂ SCD and (b) O₂ SCD. Units for the CO₂ and O₂ SCDs are scaled as in Figure 2. The red lines indicate 1:1 correspondence between measured and geometric SCDs.

The simulated variations of CO₂ and O₂ SCD are shown in Figure 2.4 and match the CLARS observations. Furthermore, the 'U-shape' of the O₂ SCD also shows a larger low bias than that for the CO₂ SCD for the same aerosol conditions.

This demonstrates that aerosol scattering is the cause of the low bias in the CO₂ and O₂ SCD. SCD biases caused by aerosol scattering are not equal in the two absorption bands and therefore cannot be removed by the ratioing in the calculation of X_{CO2}.

The retrieval bias in the SCDs due to neglecting aerosol scattering can be estimated using the Rodgers method [Rodgers, 2000], as shown in Equation (2.5)

$$\Delta SCD = \mathbf{G}\mathbf{K}_b \cdot \tau_s \quad (2.5)$$

where ΔSCD is the fractional SCD retrieval bias; \mathbf{K}_b is the Jacobian of radiance with respect to AOD τ_s ; $\mathbf{G} = \mathbf{S}_a \mathbf{K}^T (\mathbf{K} \mathbf{S}_a \mathbf{K}^T + \mathbf{S}_e)^{-1}$ is the gain matrix, or the sensitivity of the SCD retrieval to the observed radiance. This method provides a linear estimate of the aerosol influence on the SCD retrieval bias. In the O₂ absorption band, $\mathbf{G}\mathbf{K}_b = -1.94$, $\tau_s = 0.1$ corresponds to a SCD retrieval deficit of 19.4%; in the CO₂ absorption band, $\mathbf{G}\mathbf{K}_b = -1.81$, $\tau_s = 0.1$ corresponds to a SCD retrieval deficit of 18.1%. The bias analysis shows that a typical AOD of 0.07~0.08 causes biases in the CO₂ and O₂ SCD retrieval of up to 13~17%, consistent with the U-shape shown in Figure 2.2. The SCD bias for O₂ is larger than that for CO₂ at the same AOD. As a result, X_{CO2} calculated according to Equation (2.1) would exhibit a high bias.

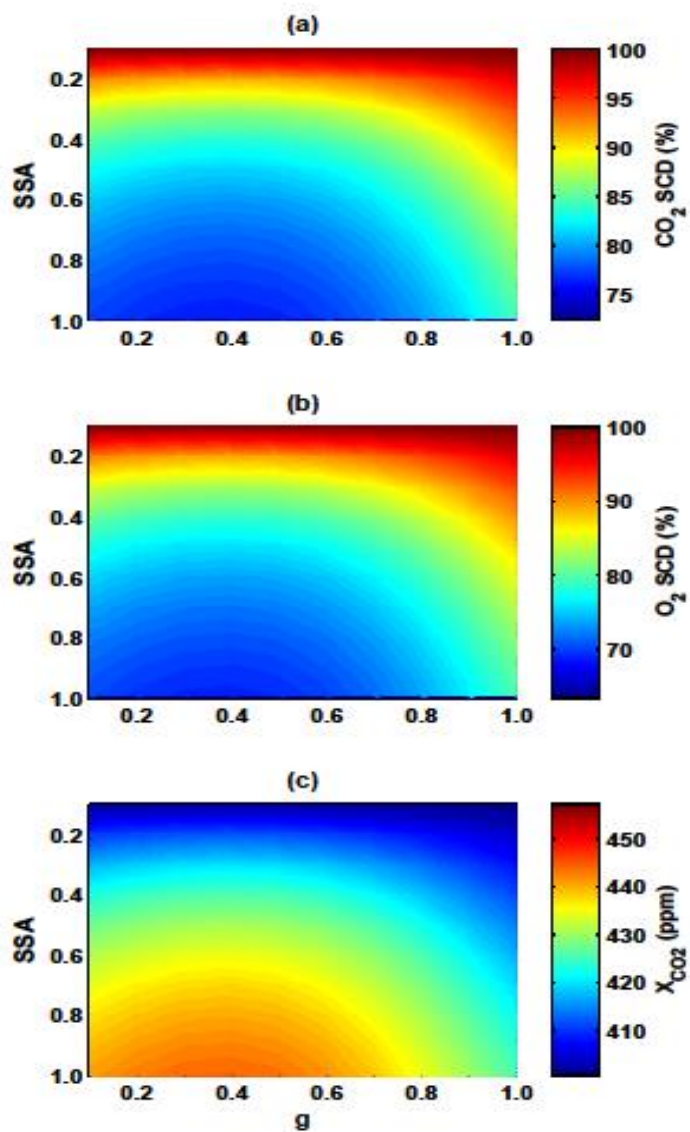


Figure 5. Simulation results when aerosol scattering is neglected for (a) CO₂ SCD (b) O₂ SCD and (c) X_{CO2}. Effects of different kinds of aerosols are investigated in the SSA-g parameter space with AOD = 0.1 (in the CO₂ absorption band). SCD simulation results are displayed in percentage, 100% corresponds to the true value. The true value of X_{CO2} is 400.8 ppm. Biases are measured as the deviation from the true value. We use a fixed viewing geometry in the simulations, with SZA = 45.2°, VZA = 83.1°, and AZA = 9.7°.

It is also of interest to study the measurement bias caused by different kinds of aerosols. For non-isotropic aerosol scattering, we explore the measurement bias in the single scattering albedo-asymmetry parameter space, as shown in Figure 2.5. We assume that the aerosol scattering has a Henyey-Greenstein type phase function [Henyey and Greenstein, 1941] with single scattering albedo (SSA) ω_0 and asymmetry parameter g . The AOD is kept constant at 0.1 (in the CO₂ band). We find that the simulated SCDs are always less than the geometric SCD calculated from the true atmospheric profile. This indicates that aerosol scattering reduces the apparent absorption in the normalized radiance, as described in Section 2.3. When calculating X_{CO2} using Equation (2.1) without taking the wavelength dependence into account, the mean mixing ratio would be over-estimated. At constant AOD, the biases in X_{CO2} and SCDs depend on both the SSA and the asymmetry parameter. The retrieval bias increases with ω_0 , and decreases with g . By using the delta-Eddington approximation [Wiscombe, 1977], we can get the equivalent isotropic AOD τ_s' and SSA ω' for the forward peaked scattering as shown in Equations (6) – (7) [Goody and Yung, 1989; Liou, 2002].

$$\tau_s' = (1 - f)\tau_s \quad (2.6)$$

$$\omega' = \frac{1 - f}{1 - f\omega} \omega \quad (2.7)$$

where f is the fraction of scattered energy residing in the forward peak. In the delta-Eddington approximation, f is typically taken to be g^2 [Joseph et al., 1976].

Therefore, a more forward-peaked phase function ($g > 0$) leads to smaller aerosol scattering as well as smaller measurement bias.

2.5. Bias correction

With the 2S-ESS model currently in place, it is straightforward to correct the aerosol induced bias in CLARS X_{CO_2} retrievals. Previous studies have demonstrated that the retrieval bias for X_{CO_2} can be greatly mitigated when simple aerosol parameters are incorporated into the retrieval algorithm [Butz *et al.*, 2009; Guerlet *et al.*, 2013]. However, these methods rely on calibrated radiances; for CLARS-FTS, calibration of the absolute radiance is currently unavailable. Using only relative radiances, the retrieval using a full-physics model would face the problem of degeneracy, as presented in Section 2.3. In this study, a fast and effective scaling approach is developed to correct for the bias in X_{CO_2} , as shown in Equation (2.8). The aim is to correct the GFIT retrieval using an empirical relationship between the O_2 SCD and X_{CO_2} retrieval biases gained from a full-physics model, so that we can avoid running computationally expensive retrievals.

$$X_{CO_2} = 0.2095 \frac{SCD_{CO_2}}{SCD_{O_2} \cdot f(b_{O_2})} \quad (2.8)$$

In Equation (2.8), rather than making the assumption that aerosol induced biases in the O_2 and CO_2 SCDs are the same (Equation 2.1), we assume that the biases in the two absorption bands are different. The difference is measured by a correction factor $f(b_{O_2})$ and this factor is only dependent on the bias in O_2 SCD, b_{O_2} (one minus O_2 scaling factor). If Equation (2.1) is a first-order correction, which

mitigates the bias in X_{CO_2} by ratioing CO_2 SCD with O_2 SCD, Equation (2.8) incorporates a second-order correction, which is expected to produce relatively accurate X_{CO_2} values even in the presence of moderate to high aerosol loading.

In Figure 2.6, we calculate the one-to-one relationship between the bias in O_2 SCD, b_{O_2} and the X_{CO_2} correction factor, $f(b_{\text{O}_2})$. The model set-up is the same as in Section 2.4. Climatological aerosol properties in the LA region are used and the viewing geometry is fixed as appropriate for a measurement in West Pasadena. Synthetic data with different AODs are generated. A forward model in which AOD is set to be zero is employed to simulate the retrieval by GFIT. Figure 2.6 (a) shows the retrieval biases in O_2 SCD, CO_2 SCD, and X_{CO_2} as a function of AOD when a simple model like GFIT is applied. A scaling factor of unity corresponds to the true value. The scaling factors for the O_2 SCD (red) and X_{CO_2} (black) can be used to set up an empirical relationship between the O_2 SCD bias and the X_{CO_2} correction factor in Figure 2.6 (b).

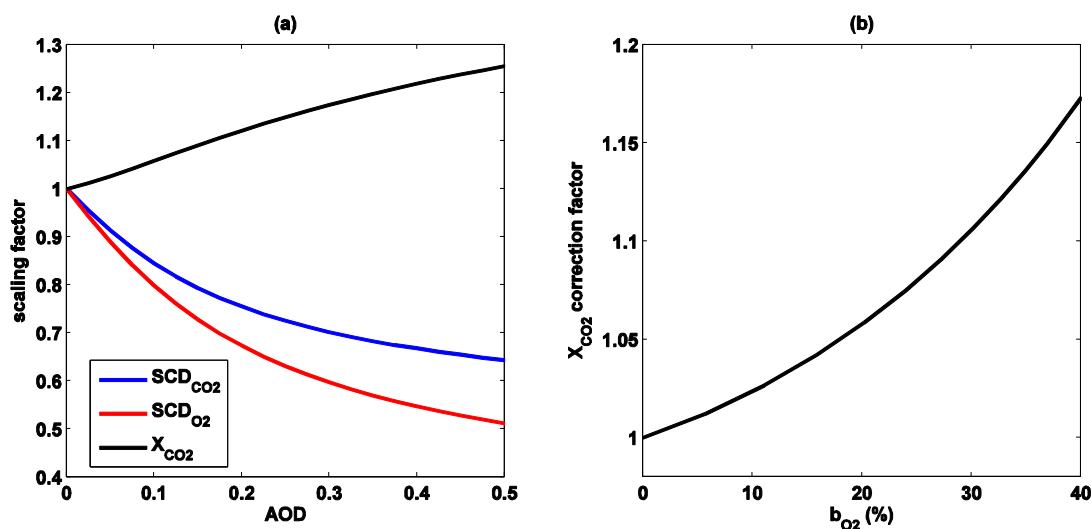


Figure 2.6. (a) Retrieval biases in CO₂ SCD (blue), O₂ SCD (red), and X_{CO₂} (black) caused by different AOD. Retrieval biases are measured by the deficit/excess in scaling factors. In the simulations, each layer in the atmospheric profile is multiplied by the constant scaling factor. Scaling factor = 1 corresponds to the true value. Climatological aerosol parameters in the LA region (Table 1) are used. We use the same viewing geometry as that in Figure 2.5. (b) X_{CO₂} correction factor $f(b_{O_2})$ as a function of O₂ SCD bias.

Using this approach, we can infer the bias in X_{CO₂} from the difference between the measured O₂ SCD and the geometric O₂ SCD. Then, the inferred bias can be used as a scaling factor to correct the X_{CO₂} retrieval result from GFIT. This approach is reasonable because we can get very accurate estimation of the surface pressure from NCEP or ECWMF reanalysis data. The O₂ mixing ratio in the atmosphere is almost constant as 0.2095. It is estimated that the error in the surface pressure *a priori* information for a space-borne mission is below 1 hPa, with 4 hPa as a pessimistic estimate when the uncertainty in topography is considered [O'Dell *et al.*, 2012]. For CLARS-FTS, the target sites are known locations. Therefore, the surface pressure uncertainties should be even smaller than that for a satellite measurement. A surface pressure error of 4 hPa leads to a 0.4% error in the O₂ SCD, which then translates to a 1.6 ppm error in the X_{CO₂} (Equation 1).

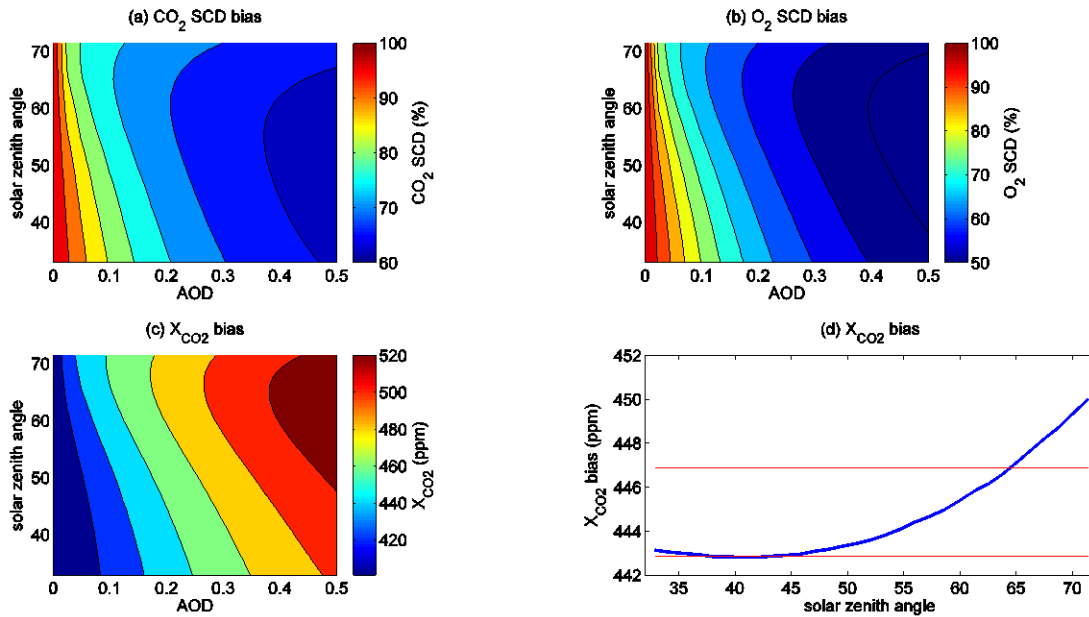


Figure 2.7. Simulation results when aerosol scattering is neglected for: (a) CO₂ SCD, (b) O₂ SCD and (c) X_{CO2}. Combined effect of AOD and viewing geometry is investigated. SCD simulation results are displayed in percentage, 100% corresponds to the true value. The true value of X_{CO2} is 400.8 ppm. Biases are measured as the deviation from the true value. We vary the solar zenith angle from 32.9° (noon) to 72.5° (late afternoon). Relative azimuth angle is also changed correspondingly in the calculation but not shown in figure labels. (d) X_{CO2} for the contour line of $b_{O_2} = 30\%$ (O₂ SCD scaling factor = 0.7). Red lines indicate ± 2 ppm variation.

It is crucial to show that the X_{CO2} correction factor $f(b_{O_2})$ is only a function of the O₂ SCD bias and not influenced by other parameters such as geometry, aerosol phase function, and aerosol SSA. In other words, if we observe a deficit in the measured O₂ SCD, the bias in X_{CO2} can be inferred irrespective of other parameters. Otherwise, $f(b_{O_2})$ would become a multi-variable function and require extensive computation in a multi-dimensional parameter space. In Figure 2.7, we test the combined effect of geometry and AOD on the O₂ SCD, CO₂ SCD and X_{CO2}.

Intuitively, both a larger AOD and a larger SZA would enhance scattering and increase biases in the O₂ and CO₂ SCD retrievals. The scattering angle, which is a function of SZA, AZA, and VZA, also matters if the scattering phase function is not isotropic. To test whether $f(b_{O_2})$ is influenced by geometry, we find the X_{CO₂} values in Figure 2.7(c) corresponding to the 70% O₂ SCD contour in Figure 2.7(b), and plot them as a function of SZA in Figure 2.7(d). If $f(b_{O_2})$ is a function independent of viewing geometry, we would expect to see a straight line, since all the X_{CO₂} scaling factors along the line corresponds to the same O₂ SCD bias ($b_{O_2} = 30\%$). The line in Figure 2.7(d) is not absolutely straight, but the variations are small. The error in X_{CO₂} due to the assumption that $f(b_{O_2})$ is independent of viewing geometry would be within ± 2 ppm, if the solar zenith angle is smaller than 65° (red lines in Figure 2.7d). Note that an O₂ SCD bias of 30% is very large. We rarely observe such a large bias in the CLARS observations even though it has very high sensitivity to aerosol scattering. For a typical CLARS viewing geometry at noon, a 30% O₂ SCD bias indicates a local AOD larger than 0.2 in the 1.61 μm CO₂ band, or equivalently an AOD larger than 0.4 in the O₂ A-band.

The same method is applied to analyze whether $f(b_{O_2})$ is influenced by the aerosol scattering phase function and SSA, as shown in Figures 2.8 and 2.9. In order to test the sensitivity of the X_{CO₂} correction factor to the aerosol phase function, we employ the Henyey-Greenstein phase function. In Figure 2.8, the combined effects of the phase function asymmetry factor and AOD are tested. The asymmetry parameter g varies from 0 to 1. The SSA is held constant at 0.95 for all simulations. The viewing geometry is fixed as appropriate for an observation in the afternoon,

with $\text{SZA} = 45.2^\circ$, $\text{VZA} = 83.1^\circ$, and $\text{AZA} = 9.7^\circ$. According to the Delta-Eddington approximation, a larger g would reduce the effect of scattering. In Figure 2.8(d), we find that the error in X_{CO_2} due to the assumption that $f(b_{02})$ is independent of the aerosol phase function is within ± 1 ppm, if g is smaller than 0.9.

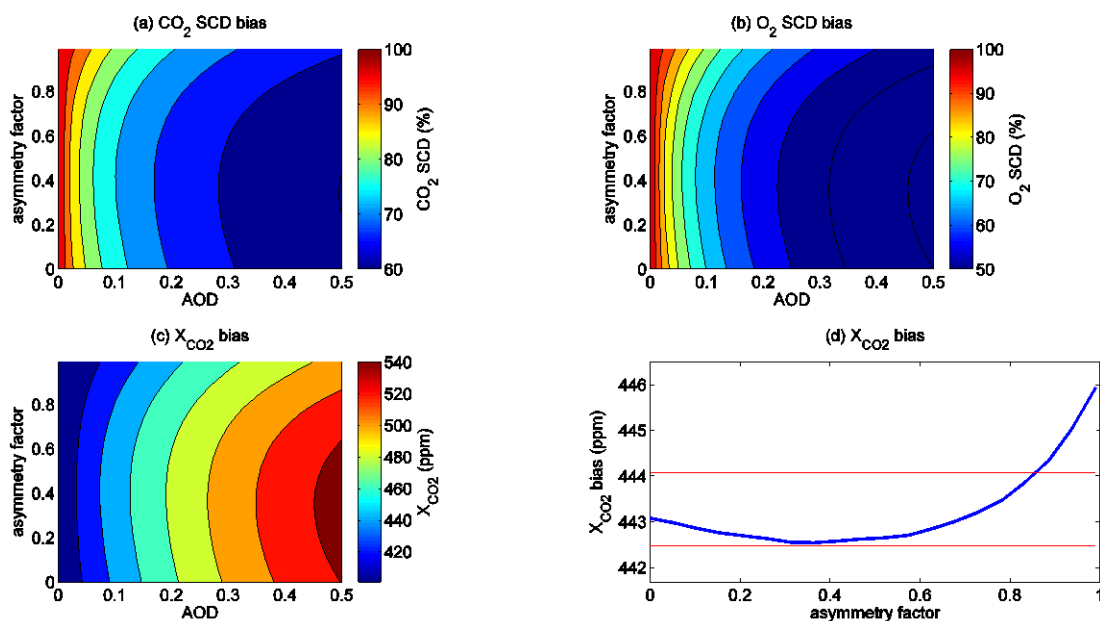


Figure 2.8. Same as Figure 2.7, but for the combined effect of AOD and asymmetry parameter in the scattering phase function. Red lines indicate ± 1 ppm variation.

In Figure 2.9, we fix the asymmetry factor g at 0.75 and explore the sensitivity of $f(b_{02})$ to the aerosol SSA. The same viewing geometry is used in the calculation as that in Figure 2.8. Figure 2.9(d) demonstrates that the error in X_{CO_2} correction due to the assumption that $f(b_{02})$ is independent of aerosol SSA is within ± 1 ppm, if the SSA is larger than 0.2.

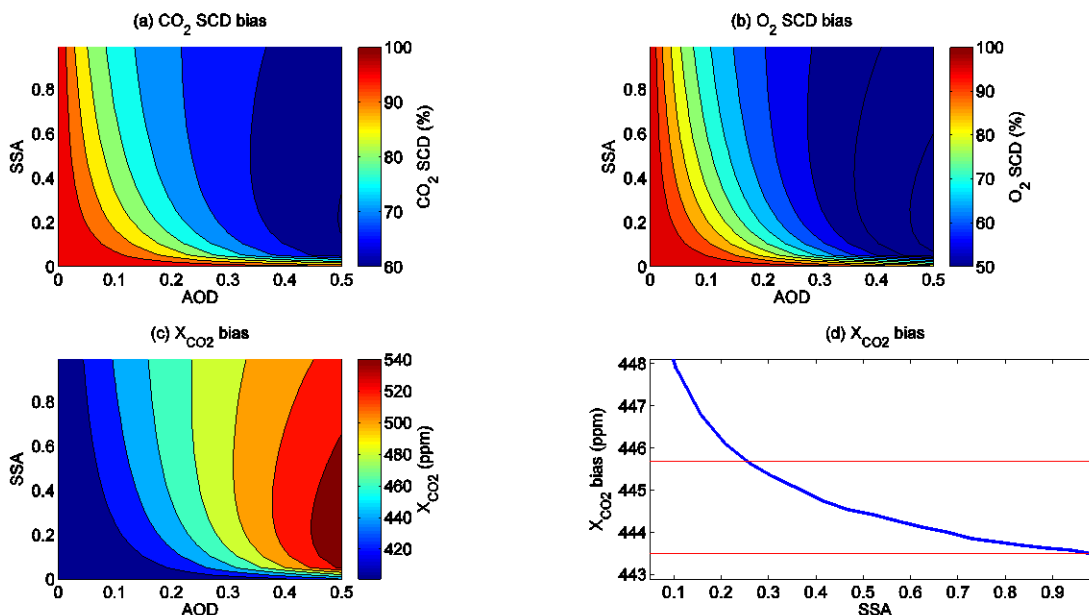


Figure 2.9. Same as Figure 2.7, but for the combined effect of AOD and SSA. Red lines indicate ± 1 ppm variation.

Several factors contribute to the uncertainty of this scaling correction approach. Here we have studied the errors due to uncertainties in surface pressure estimation (σ_{pre}), viewing geometry (σ_{geo}), scattering phase function (σ_g), and aerosol SSA (σ_{SSA}). Assuming that these four effects are independent and uncorrelated, a simple error estimate would be $\sigma = \sqrt{\sigma_{pre}^2 + \sigma_{geo}^2 + \sigma_g^2 + \sigma_{SSA}^2}$, which results in a value of 2.9 ppm. In this study, other parameters such as surface albedo and Angstrom coefficient are assumed to be known from external sources. As we will see in the next section, this approach significantly reduces the aerosol-induced bias in the X_{CO2} product.

2.6. Validation

To test the effectiveness of the bias correction approach, we need to compare the corrected CLARS X_{CO_2} time series against a benchmark. Measurements from CLARS have a long light path through the PBL. Therefore, it is very hard to validate the CLARS X_{CO_2} product using aircraft measurements. TCCON measures the total column average X_{CO_2} from the surface to the top of atmosphere and is often used to validate satellite X_{CO_2} retrievals [Wunch *et al.*, 2011]. The TCCON station at JPL is very close to the CLARS West Pasadena target site in both the horizontal and vertical directions. We employ the JPL TCCON data as the ground truth to validate the CLARS X_{CO_2} measurements. However, the comparison is not straightforward. CLARS X_{CO_2} measurements have a much larger contribution from the PBL than TCCON or a typical satellite (Figure 2.1). In megacities with large CO_2 emissions, X_{CO_2} in the PBL is often higher than that in the free troposphere. Therefore, we expect the CLARS X_{CO_2} measurements to be higher than those from TCCON. Fortunately, we also have CLARS Spectralon measurements to constrain the X_{CO_2} in the free troposphere. The CLARS Spectralon viewing mode takes direct sun measurements similar to TCCON. For most of the daytime, the PBL top is below the CLARS site and the spectralon measurements are not influenced by aerosol scattering [Newman *et al.*, 2013].

We use a simple two-box model to calculate the CO_2 mixing ratio along the CLARS West Pasadena light path, as shown in Figure 2.1. We assume that the CO_2 mixing ratio is X_0 and $X_0 + \Delta X$ in the free troposphere and the PBL, respectively. Pressures at the surface, the top of the PBL, and the CLARS instrument are P_0 , $P_0 -$

ΔP , and P_1 , respectively. Using this simple model, the JPL TCCON station measurements (TCC), CLARS Spectralon measurements (SPC), and estimated CLARS West Pasadena measurements (WP) can be calculated using Equation (2.9) – (2.11).

$$SPC = X_0 \quad (2.9)$$

$$TCC = X_0 + \Delta P \Delta X / P_0 \quad (2.10)$$

$$WP = X_0 + \frac{\Delta P \Delta X [1 / \cos(SZA) + 1 / \cos(VZA)]}{P_0 / \cos(SZA) + (P_0 - P_1) / \cos(VZA)} \quad (2.11)$$

If the viewing geometries of both TCCON and CLARS West Pasadena measurements are known, we can solve for WP and calculate the estimated average CO_2 mixing ratio along the CLARS light path in West Pasadena, as shown in Equation (2.12):

$$WP = \frac{(TCC - SPC) \cdot [P_0 / \cos(SZA) + P_0 / \cos(VZA)]}{P_0 / \cos(SZA) + (P_0 - P_1) / \cos(VZA)} + SPC \quad (2.12)$$

This method is not sensitive to the PBL height so long as the PBL is below the CLARS site. There are several assumptions made here. First, we assume that the PBL height is uniform in both the incoming solar and outgoing viewing directions. Second, the X_{CO_2} in the PBL and the free troposphere is well mixed and horizontally uniform. We also neglect the spatial differences between the TCCON JPL station and the CLARS West Pasadena target site.

In Figure 2.10, CLARS and TCCON measurements on March 23, 2013 are shown. In the left panel, TCCON X_{CO_2} measurements are shown in red and CLARS Spectralon X_{CO_2} measurements are shown in green. The expected average X_{CO_2}

along the CLARS light path in West Pasadena (black) is calculated according to Equation (2.12) using both TCCON and CLARS Spectralon measurements. The blue curve shows the CLARS operational X_{CO_2} product without any correction. It is clear that in the afternoon, CLARS X_{CO_2} retrievals show a high bias of up to 20 ppm due to aerosol scattering, consistent with the analysis in Figure 2.5.

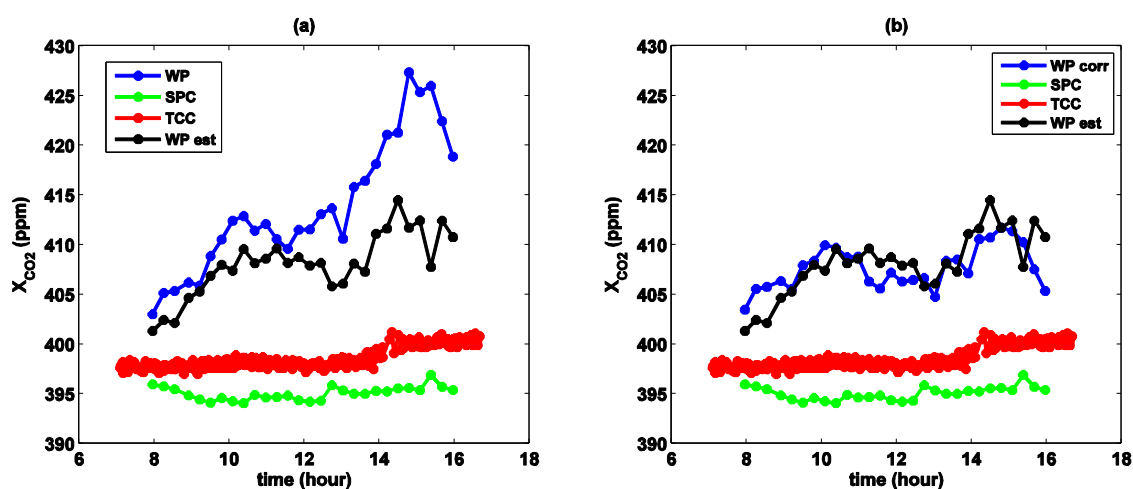


Figure 2.10. Validation of CLARS West Pasadena measurements. Data on March 23, 2013 are shown. Green curves represent the CLARS Spectralon X_{CO_2} data (SPC). Red curves represent the JPL TCCON station X_{CO_2} data (TCC). Black curves represent the estimation of X_{CO_2} along the CLARS viewing light path at West Pasadena (WP est). In Panel (a), the blue curve represents the CLARS operational X_{CO_2} product in West Pasadena retrieved by GFIT (WP). In Panel (b), the blue curve represents the corrected CLARS X_{CO_2} product using our proposed approach (WP corr).

In the right panel of Figure 2.10, the green, red, and black curves are the same as those in the left panel, representing CLARS Spectralon, TCCON, and estimated CLARS West Pasadena measurements. The blue curve is the corrected CLARS West Pasadena measurement using the scaling approach proposed above. We first

determine the O_2 SCD bias from the difference between the geometric and measured O_2 SCDs (e.g., Figure 2.2). Then, the corresponding X_{CO_2} correction factor $f(b_{O_2})$ can be found from Figure 2.6(b). We finally divide the GFIT operational X_{CO_2} product (blue curve in the left panel) by this correction factor and get the corrected X_{CO_2} measurements (blue curve in the right panel). The aerosol induced bias in X_{CO_2} is significantly reduced by making the correction. The root mean square (RMS) of the discrepancies between the black and blue curves in Figure 2.10 (b) is 2.4 ppm, which is below our error estimate. As shown in Figure 2.10, CLARS-FTS has excellent sensitivity to boundary layer X_{CO_2} enhancement, which makes it particularly useful to study emissions in a megacity. The estimated error for this proposed correction approach is larger than that for a satellite-based measurement (e.g. OCO-2 [O'Dell *et al.*, 2012]), mainly because CLARS-FTS has high sensitivity to aerosol scattering and we are studying hazy scenarios in a megacity. However, the precision is good enough for analyzing the temporal and spatial variability of X_{CO_2} in the LA basin.

CLARS measurements on other hazy days show similar features as Figure 2.10. When aerosol scattering is neglected, the X_{CO_2} retrieval typically shows a high bias. The bias can be significantly reduced when we apply the correction approach based on the O_2 SCD. In Figure 2.11, we test all available CLARS West Pasadena measurements in 2013 when concurrent JPL TCCON measurements are available. The RMS of discrepancies between the X_{CO_2} measurements and the estimates (Equation 2.12) is reduced from 9.1 ppm to 3.4 ppm by the proposed correction approach. The correlation coefficient between the X_{CO_2} measurements and

estimates also rises from 0.56 to 0.80 as a result of the correction. The approach proposed in this study only aims to correct the X_{CO_2} retrieval bias caused by aerosol scattering. There are other factors that potentially contribute to the discrepancy between the corrected CLARS measurements and the estimates using Equation (2.12). For example, the assumptions that the PBL height is uniform and that CO_2 is well mixed in the PBL may not hold in some cases.

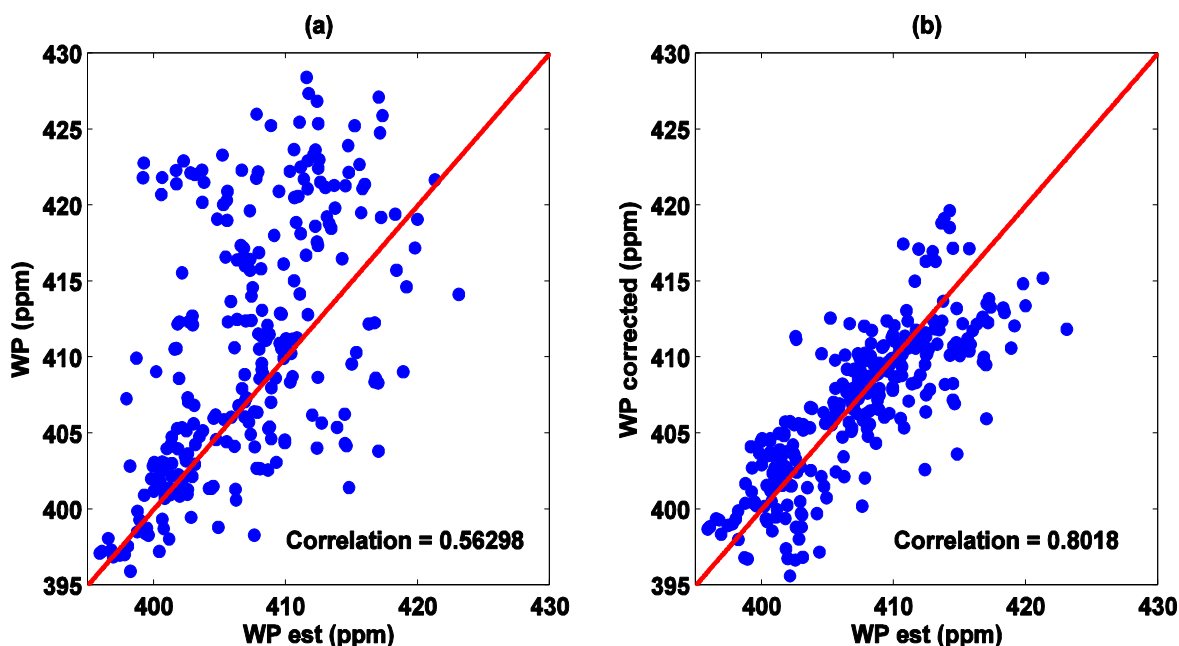


Figure 2.11. Scatter plot of CLARS West Pasadena X_{CO_2} measurements against the estimates (WP est) based on Equation (2.12). (a) CLARS measurements (WP) retrieved by GFIT, which totally neglects aerosol scattering. (b) Corrected measurements (WP corrected) using our proposed method. The red line in each panel shows the 1:1 relationship. Without correction, the correlation coefficient between the CLARS West Pasadena measurements and the estimates based on Equation (2.12) is 0.56. After the correction, the correlation coefficient rises to 0.80. The displayed data are from 9 separate days of observations and include 274 separate data points.

2.7. Discussions and conclusions

Assuming that the aerosols are evenly distributed in the PBL, the CLARS-FTS retrieved SCD shows a low bias regardless of the value of aerosol SSA and phase function asymmetry parameter. An examination of CLARS-FTS measurements (similar to Figure 2.2) on other hazy days also confirms that the retrievals of CO₂ and O₂ SCDs are less than the geometric estimates without exception. This is mainly due to the unique observation geometry of the CLARS-FTS instrument. The CLARS site is very low in altitude. Only the aerosols within the PBL strongly influence the observed reflected spectral radiance. For a typical satellite viewing geometry, if the surface is bright and the aerosol/cloud layer is high, scattering could also enhance photon path length, resulting in an increased apparent absorption.

Aerosol scattering has wavelength dependence. Therefore, ratioing CO₂ and O₂ SCDs cannot totally cancel the bias in the X_{CO2} product. The X_{CO2} bias can be mitigated by simply filtering the data based on the criterion that O₂ SCD bias < 10%, as demonstrated in *Wong et al.* [2015].

We propose an effective and fast approach to correct the aerosol induced bias in the X_{CO2} retrieval using non-calibrated reflected solar radiance. The approach is potentially applicable to other ground based instruments dedicated to measuring greenhouse gas abundances. X_{CO2} could first be retrieved using a simple and fast model, such as GFIT, which allows for non-calibrated radiance but does not account for aerosol scattering. The bias in the X_{CO2} product caused by aerosol scattering can be reduced based on the difference between the measured and geometric O₂ SCDs.

This approach offers a much higher accuracy than a simple ratioing between the O₂ and CO₂ SCDs. Since GFIT is much simpler and faster than most of the full-physics models, this approach is numerically efficient and particularly applicable to massive data processing when computational resources are limited.

The correction accuracy could be further improved by incorporating another parameter, other than the bias in the O₂ SCD, into the empirical relationship. In this study, we use a fixed Angstrom coefficient to constrain the wavelength dependence of AOD between the 1.61 μm CO₂ band and the 1.27 μm O₂ band. This not a serious problem in this study since the CO₂ and O₂ bands are close to each other. However, the error caused by an inaccurate Angstrom coefficient would increase if the O₂ A band (0.76 μm) were used in the retrieval. For a typical CLARS-FTS measurement with AOD = 0.1 in the CO₂ absorption band, a ±0.1 variation in the Angstrom coefficient results in a ±0.0029 variation in the O₂ absorption band AOD, which translates into 2 ppm bias in X_{CO₂}. In principle, we can set up a two-variable empirical function $f(b_{O_2}, \kappa)$ to correct for the bias in X_{CO₂}, where κ is the AOD Angstrom coefficient. This would require additional information on the AOD wavelength dependence. Surface albedo is another important parameter as incorrect albedos in the CO₂ and O₂ absorption bands could potentially lead to biases in the X_{CO₂} products. For CLARS instrument, surface albedo can be measured on a clear day with reference to the spectra from the Spectralon.

The CLARS mountaintop remote sensing observations of greenhouse gases in an urban source region provide a heretofore unavailable dataset to study the effects of aerosols on high-precision trace gas retrievals. Since these data are diurnally

resolved over a wide range of solar zenith and viewing angles and aerosol loadings, they provide for a critical comparison between the retrieved SCD daily variations from CLARS-FTS measurements and the model simulations constrained by AERONET data. The framework developed here provides a means to compare the CLARS results with reference data from simultaneous TCCON observations, which are relatively immune to aerosol extinction.

There are potential applications of CLARS-FTS measurements for the OCO-3 CO₂ mission [Eldering *et al.*, 2014]. OCO-3 employs an agile pointing system, thus permitting a city mode, which maps an area approximately 60 km × 60 km at high resolution (~5.5 km in nadir view from 400 km altitude). This observing mode, combined with the low-inclination orbit of the International Space Station (ISS), which precesses in local time, is ideal for detecting and quantifying the spatial variability of fossil fuel emissions in rapidly developing urban centers. The measurements from CLARS-FTS provide the capability of spatially mapping the GHGs in the LA basin, whose emissions vary in complex temporal/spatial multimodal cycles. This unique spatial mapping capability of CLARS-FTS measurements, which helps in validating OCO-3 measurements under urban environments, is not available from the existing TCCON measurements. In addition, it is possible to generalize our work to include other species such as CH₄ and CO. Our results can also be used to improve the retrieval algorithm for the ESA TROPOspheric Monitoring Instrument (TROPOMI) mission [Veefkind *et al.*, 2012].

Appendix 2.1: Two-stream analytic model

A.2.1.1. Influence of aerosols on radiance

We solve a simplified radiative transfer equation without the source term as shown in equation (2.A1) to explain the change of radiance due to aerosols [Goody and Yung, 1989; Liou, 2002]. We assume that the scattering is isotropic and the single scattering albedo ω_0 is a constant. In this equation I is the radiance, τ is the optical depth and $\mu=1/\cos(\theta)$, where θ is the viewing zenith angle or the SZA. This approximation is accurate only to the first order. We neglect the term associated with the incoming solar irradiance and assume that it is the same as the isotropic diffusive flux at the top of the atmosphere.

$$\mu \frac{\partial I(\tau, \mu)}{\partial \tau} = I(\tau, \mu) - \frac{1}{2} \omega_0 \int_{-1}^1 I(\tau, \mu) d\mu \quad (2.A1)$$

Separating upward and downward streams using two-stream approximation as

$$\bar{\mu} \frac{dI^+(\tau, \bar{\mu})}{d\tau} = I^+(\tau, \bar{\mu}) - \frac{1}{2} \omega_0 [I^+(\tau, \bar{\mu}) + I^-(\tau, -\bar{\mu})] \quad (2.A2)$$

$$-\bar{\mu} \frac{dI^-(\tau, -\bar{\mu})}{d\tau} = I^-(\tau, -\bar{\mu}) - \frac{1}{2} \omega_0 [I^+(\tau, \bar{\mu}) + I^-(\tau, -\bar{\mu})] \quad (2.A3)$$

we can solve for general solutions as below, where $I^+(\tau) = I^+(\tau, \bar{\mu})$, $I^-(\tau) = I^-(\tau, \bar{\mu})$.

$$I^+(\tau) = (1 - \bar{\mu}\rho)c_1 e^{-\rho\tau} + (1 + \bar{\mu}\rho)c_2 e^{\rho\tau} \quad (2.A4)$$

$$I^-(\tau) = (1 + \bar{\mu}\rho)c_1 e^{-\rho\tau} + (1 - \bar{\mu}\rho)c_2 e^{\rho\tau} \quad (2.A5)$$

$$\rho^2 = \frac{1 - \omega_0}{\bar{\mu}^2} \quad (2.A6)$$

$$\bar{\mu} = \frac{1}{\sqrt{3}} \quad (2.A7)$$

Applying the boundary conditions to account for the reflection at the surface, where α is the surface albedo and F is the incoming solar flux,

$$(1 + \bar{\mu}\rho)c_1 + (1 - \bar{\mu}\rho)c_2 = \frac{1}{2\pi} F \quad (2.A8)$$

$$(1 - \bar{\mu}\rho)c_1 e^{-\rho\tau_1} + (1 + \bar{\mu}\rho)c_2 e^{\rho\tau_1} = \alpha[(1 + \bar{\mu}\rho)c_1 e^{-\rho\tau_1} + (1 - \bar{\mu}\rho)c_2 e^{\rho\tau_1}] \quad (2.A9)$$

we can get the two-stream general solution with surface albedo at arbitrary optical depth

$$I^+(\tau) = \frac{1}{2\pi} F \frac{[\omega_0 - \alpha(1 - \bar{\mu}\rho)^2]e^{\rho(\tau_1 - \tau)} - [\omega_0 - \alpha(1 + \bar{\mu}\rho)^2]e^{-\rho(\tau_1 - \tau)}}{[(1 + \bar{\mu}\rho)^2 - \alpha\omega_0]e^{\rho\tau_1} - [(1 - \bar{\mu}\rho)^2 - \alpha\omega_0]e^{-\rho\tau_1}} \quad (2.A10)$$

$$I^-(\tau) = \frac{1}{2\pi} F \frac{[(1 + \bar{\mu}\rho)^2 - \alpha\omega_0]e^{\rho(\tau_1 - \tau)} - [(1 - \bar{\mu}\rho)^2 - \alpha\omega_0]e^{-\rho(\tau_1 - \tau)}}{[(1 + \bar{\mu}\rho)^2 - \alpha\omega_0]e^{\rho\tau_1} - [(1 - \bar{\mu}\rho)^2 - \alpha\omega_0]e^{-\rho\tau_1}} \quad (2.A11)$$

At the top and bottom, emergent radiances are shown by equation (2.A13)-(2.A14).

$$I^+(0) = \frac{1}{2\pi} F \frac{[\omega_0 - \alpha(1 - \bar{\mu}\rho)^2]e^{\rho\tau_1} - [\omega_0 - \alpha(1 + \bar{\mu}\rho)^2]e^{-\rho\tau_1}}{[(1 + \bar{\mu}\rho)^2 - \alpha\omega_0]e^{\rho\tau_1} - [(1 - \bar{\mu}\rho)^2 - \alpha\omega_0]e^{-\rho\tau_1}} \quad (2.A13)$$

$$I^-(\tau_1) = \frac{2\bar{\mu}\rho F}{\pi} \frac{1}{[(1 + \bar{\mu}\rho)^2 - \alpha\omega_0]e^{\rho\tau_1} - [(1 - \bar{\mu}\rho)^2 - \alpha\omega_0]e^{-\rho\tau_1}} \quad (2.A14)$$

The non-dimensional value of reflectance is calculated in equation (2.A15).

$$R(\tau_1, \omega_0) = \frac{[\omega_0 - \alpha(1 - \bar{\mu}\rho)^2]e^{\rho\tau_1} - [\omega_0 - \alpha(1 + \bar{\mu}\rho)^2]e^{-\rho\tau_1}}{[(1 + \bar{\mu}\rho)^2 - \alpha\omega_0]e^{\rho\tau_1} - [(1 - \bar{\mu}\rho)^2 - \alpha\omega_0]e^{-\rho\tau_1}} \quad (2.A15)$$

A.2.1.2. One-line spectra

Only pressure broadening is considered in this model as Doppler and natural broadenings are weak in the troposphere where most of the absorption occurs [Goody and Yung, 1989]. The atmosphere is divided into two layers: a free troposphere with absorption only and a PBL with absorption and scattering. We define the pressure at the top of PBL to be P_1 . In this model, P_1 is defined to be 800 hPa.

The absorption coefficient of a Lorentzian absorption line shape is

$$k = S \frac{\alpha_L}{\pi} \frac{1}{\alpha_L^2 + (\nu - \nu_0)^2} \quad (2.A16)$$

where $\alpha_L = \alpha_L^0(p/p_0)$ is half-width of the line at the half-maximum [Liou, 2002], p is the pressure and α_L^0 is the line width at the reference pressure p_0 . The optical depth of the free troposphere is given by

$$\tau_1 = \tau_{1a} = \frac{S\chi}{\pi mg} \int_0^{P_1} \frac{Ap}{(Ap)^2 + (\nu - \nu_0)^2} dp = \frac{S\chi}{2\pi mgA} \ln \frac{P_1^2 + [(\nu - \nu_0)/A]^2}{[(\nu - \nu_0)/A]^2} \quad (2.A17)$$

where S is the line strength constant, $A = \alpha_L/p = \alpha_L^0/p_0$. The two constants A and S can be obtained from the HITRAN database [Rothman *et al.*, 2008]. In this model, for the CO₂ absorption line $\nu_0 = 6243.9 \text{ cm}^{-1}$, $S = 1.52 \times 10^{-23} \text{ cm}$, $A = 7.2 \times 10^{-7} \text{ cm}^{-1} \text{ Pa}^{-1}$. χ is the volume mixing ratio of the absorbing gas (CO₂). We set χ to be 400 ppm for CO₂. In the equation $m = 4.8 \times 10^{-26} \text{ kg}$ is the mean molecular weight of air, g is 9.8 m/s^2 . Note that $mg = 4.7 \times 10^{-21} \text{ cm}^2 \text{ Pa}$ is a constant. Transmittance of the free troposphere is

$$T_1 = e^{-\tau_1} \quad (2.A18)$$

In the PBL, the total optical depth is

$$\tau_{2a} = \frac{S\chi}{\pi mg} \int_{P_1}^{P_s} \frac{Ap}{(Ap)^2 + (\nu - \nu_0)^2} dp = \frac{S\chi}{2\pi mgA} \ln \frac{P_s^2 + [(\nu - \nu_0)/A]^2}{P_1^2 + [(\nu - \nu_0)/A]^2} \quad (2.A19)$$

$$\tau_2 = \tau_{2a} + \tau_s \quad (2.A20)$$

$$\gamma = \frac{\tau_s}{\tau_{2a} + \tau_s} = \frac{\tau_s}{\tau_2} \quad (2.A21)$$

where $P_s = 1030$ hPa is the surface pressure. According to equation (2.A17), at the center of the absorption line where $\nu = \nu_0$, we have a singular point with infinite absorption optical depth. In the calculation, most of the channels are away from the singular point ($|\nu - \nu_0| > 0.001 \text{cm}^{-1}$) where Lorentzian line shape is still a good approximation. This problem can be avoided in a more realistic line shape. The parameter γ is defined to be the ratio of AOD in the PBL to the total optical depth in this layer. We can modify the radiative transfer equation as

$$\mu \frac{dI(\tau, \mu)}{d\tau} = I(\tau, \mu) - \frac{1}{2} \omega_0 \gamma \int_{-1}^1 I(\tau, \mu) d\mu \quad (2.A22)$$

Repeating the calculations of the two-stream approximation, we can get the reflectance of the PBL as equation (2.A23).

$$R_2 = \frac{[\omega_0 \gamma - \alpha(1 - \bar{\mu}\rho)^2]e^{\rho\tau_2} - [\omega_0 \gamma - \alpha(1 + \bar{\mu}\rho)^2]e^{-\rho\tau_2}}{[(1 + \bar{\mu}\rho)^2 - \alpha\omega_0 \gamma]e^{\rho\tau_2} - [(1 - \bar{\mu}\rho)^2 - \alpha\omega_0 \gamma]e^{-\rho\tau_2}} \quad (2.A23)$$

Finally, what we observe as the reflectance at the level of CLARS instrument is

$$R = T_1 \cdot R_2 = e^{-\tau_1} \cdot \frac{[\omega_0 \gamma - \alpha(1 - \bar{\mu}\rho)^2]e^{\rho\tau_2} - [\omega_0 \gamma - \alpha(1 + \bar{\mu}\rho)^2]e^{-\rho\tau_2}}{[(1 + \bar{\mu}\rho)^2 - \alpha\omega_0 \gamma]e^{\rho\tau_2} - [(1 - \bar{\mu}\rho)^2 - \alpha\omega_0 \gamma]e^{-\rho\tau_2}} \quad (2.A24)$$

where τ_1 , τ_2 and γ are wavelength dependent. In this study, both the solar zenith angle and the viewing zenith angle are set to be zero. To incorporate the variation of solar zenith angle θ , we assume in each layer the optical depth

$$\tau_i(\theta) = \frac{\tau_i(0)}{\cos(\theta)} \quad (2.A25)$$

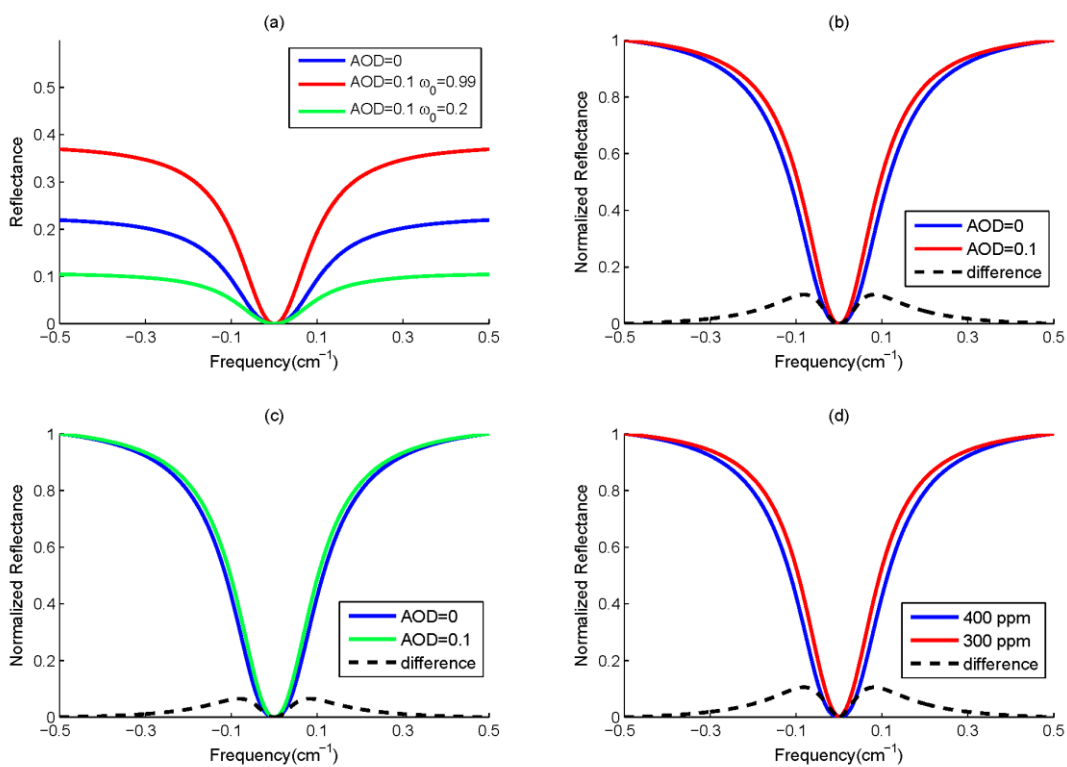


Figure 2.A1. One-line spectra simulated by the analytic model for a CO₂ absorption line. (a) Absolute reflectance with different AOD and ω_0 in the PBL. (b) Normalized reflectance with different AOD in the PBL, $\omega_0=0.99$. (c) Same as (b), $\omega_0=0.2$. (d) Normalized reflectance with different CO₂ concentrations, AOD = 0. The central frequency $\nu_0 = 6243.9 \text{ cm}^{-1}$ has been subtracted. Black dashed line shows the difference between the two spectra.

Bibliography:

- Ackermann, I. J., H. Hass, M. Memmesheimer, A. Ebel, F. S. Binkowski, and U. Shankar (1998), Modal aerosol dynamics model for Europe: Development and first applications, *Atmos Environ*, 32(17), 2981-2999, doi:Doi 10.1016/S1352-2310(98)00006-5.
- Butz, A., O. P. Hasekamp, C. Frankenberg, and I. Aben (2009), Retrievals of atmospheric CO₂ from simulated space-borne measurements of backscattered near-infrared sunlight: accounting for aerosol effects, *Appl Optics*, 48(18), 3322-3336.
- Derooij, W. A., and C. C. A. H. Vanderstap (1984), Expansion of Mie Scattering Matrices in Generalized Spherical-Functions, *Astron Astrophys*, 131(2), 237-248.
- Dudhia, A., P. E. Morris, and R. J. Wells (2002), Fast monochromatic radiative transfer calculations for limb sounding, *J Quant Spectrosc Ra*, 74(6), 745-756, doi:Pii S0022-4073(01)00285-0Doi 10.1016/S0022-4073(01)00285-0.
- Eldering A. , S. K., Matthew Bennett (2014), The Orbiting Carbon Observatory-3 (OCO-3) Mission: An Overview, paper presented at AGU Fall Meeting, San Francisco, California.
- Fu, D., T. J. Pongetti, J. F. L. Blavier, T. J. Crawford, K. S. Manatt, G. C. Toon, K. W. Wong, and S. P. Sander (2014), Near-infrared remote sensing of Los Angeles trace gas distributions from a mountaintop site, *Atmos Meas Tech*, 7(3), 713-729, doi:DOI 10.5194/amt-7-713-2014.
- Goody, R. M., and Y. L. Yung (1989), *Atmospheric Radiation: Theoretical Basis*,

Second Edition, Oxford University Press.

Guerlet, S., et al. (2013), Impact of aerosol and thin cirrus on retrieving and validating XCO₂ from GOSAT shortwave infrared measurements, *J Geophys Res-Atmos*, 118(10), 4887-4905, doi:Doi 10.1002/Jgrd.50332.

Hess, M., P. Koepke, and I. Schult (1998), Optical properties of aerosols and clouds: The software package OPAC, *B Am Meteorol Soc*, 79(5), 831-844, doi:Doi 10.1175/1520-0477(1998)079<0831:Opoaac>2.0.Co;2.

Holben, B. N., et al. (1998), AERONET - A federated instrument network and data archive for aerosol characterization, *Remote Sens Environ*, 66(1), 1-16, doi:Doi 10.1016/S0034-4257(98)00031-5.

Holben, B. N., et al. (2001), An emerging ground-based aerosol climatology: Aerosol optical depth from AERONET, *J Geophys Res-Atmos*, 106(D11), 12067-12097, doi:Doi 10.1029/2001jd900014.

Joseph, J. H., W. J. Wiscombe, and J. A. Weinman (1976), Delta-Eddington Approximation for Radiative Flux-Transfer, *J Atmos Sci*, 33(12), 2452-2459, doi:Doi 10.1175/1520-0469(1976)033<2452:Tdeaftr>2.0.Co;2.

Kalnay, E., et al. (1996), The NCEP/NCAR 40-year reanalysis project, *B Am Meteorol Soc*, 77(3), 437-471, doi:Doi 10.1175/1520-0477(1996)077<0437:Tnyrpt>2.0.Co;2.

Liou, K. N. (2002), *An Introduction to Atmospheric Radiation, Second Edition*, Academic Press.

Newman, S., et al. (2013), Diurnal tracking of anthropogenic CO₂ emissions in the Los Angeles basin megacity during spring 2010, *Atmos Chem Phys*, 13(8),

4359-4372, doi:DOI 10.5194/acp-13-4359-2013.

O'Dell, C. W., et al. (2012), The ACOS CO₂ retrieval algorithm - Part 1: Description and validation against synthetic observations, *Atmos Meas Tech*, 5(1), 99-121, doi:DOI 10.5194/amt-5-99-2012.

Oshchepkov, S., et al. (2012), Effects of atmospheric light scattering on spectroscopic observations of greenhouse gases from space: Validation of PPDF-based CO₂ retrievals from GOSAT, *J Geophys Res-Atmos*, 117, doi:Artn D12305Doi 10.1029/2012jd017505.

Rodgers, C. D. (2000), *Inverse Methods for Atmospheric Sounding: Theory and Practice*, World Scientific Publishing Co. Pte. Ltd.

Rothman, L. S., et al. (2009), The HITRAN 2008 molecular spectroscopic database, *J Quant Spectrosc Ra*, 110(9-10), 533-572, doi:DOI 10.1016/j.jqsrt.2009.02.013.

Schell, B., I. J. Ackermann, H. Hass, F. S. Binkowski, and A. Ebel (2001), Modeling the formation of secondary organic aerosol within a comprehensive air quality model system, *J Geophys Res-Atmos*, 106(D22), 28275-28293, doi:Doi 10.1029/2001jd000384.

Seinfeld, J. H., and S. N. Pandis (2006), *Atmospheric Chemistry and Physics: From Air Pollution to Climate Change, Second Edition*, 1224 pp., JOHN WILEY & SONS, INC.

Spurr, R., J. de Haan, R. van Oss, and A. Vasilkov (2008), Discrete-ordinate radiative transfer in a stratified medium with first-order rotational Raman scattering, *J Quant Spectrosc Ra*, 109(3), 404-425, doi:DOI

10.1016/j.jqsrt.2007.08.011.

Spurr, R., and V. Natraj (2011), A linearized two-stream radiative transfer code for fast approximation of multiple-scatter fields, *J Quant Spectrosc Ra*, 112(16), 2630-2637, doi:DOI 10.1016/j.jqsrt.2011.06.014.

Spurr, R. J. D. (2006), VLIDORT: A linearized pseudo-spherical vector discrete ordinate radiative transfer code for forward model and retrieval studies in multilayer multiple scattering media, *J Quant Spectrosc Ra*, 102(2), 316-342, doi:DOI 10.1016/j.jqsrt.2006.05.005.

Toon, G. C., C. B. Farmer, P. W. Schaper, L. L. Lowes, and R. H. Norton (1992), Composition Measurements of the 1989 Arctic Winter Stratosphere by Airborne Infrared Solar Absorption-Spectroscopy, *J Geophys Res-Atmos*, 97(D8), 7939-7961.

Veefkind, J. P., et al. (2012), TROPOMI on the ESA Sentinel-5 Precursor: A GMES mission for global observations of the atmospheric composition for climate, air quality and ozone layer applications, *Remote Sens Environ*, 120, 70-83, doi:DOI 10.1016/j.rse.2011.09.027.

Wiscombe, W. J. (1977), Delta-M Method - Rapid yet Accurate Radiative Flux Calculations for Strongly Asymmetric Phase Functions, *J Atmos Sci*, 34(9), 1408-1422, doi:Doi 10.1175/1520-0469(1977)034<1408:Tdmrya>2.0.Co;2.

Wong, K. W., D. Fu, T. J. Pongetti, S. Newman, E. A. Kort, R. Duren, Y. K. Hsu, C. E. Miller, Y. L. Yung, and S. P. Sander (2015), Mapping CH₄ : CO₂ ratios in Los Angeles with CLARS-FTS from Mount Wilson, California, *Atmos*

Chem Phys, 15(1), 241-252, doi:DOI 10.5194/acp-15-241-2015.

Wunch, D., G. C. Toon, J. F. L. Blavier, R. A. Washenfelder, J. Notholt, B. J. Connor, D. W. T. Griffith, V. Sherlock, and P. O. Wennberg (2011), The Total Carbon Column Observing Network, *Philos T R Soc A*, 369(1943), 2087-2112, doi:DOI 10.1098/rsta.2010.0240.

X_{CO₂} RETRIEVAL ERROR OVER DESERTS NEAR CRITICAL SURFACE ALBEDO

3.1. Introduction

The Orbiting Carbon Observatory-2 mission (OCO-2) was launched in July 2014 to measure the concentration of CO₂ accurately from space. OCO-2 was designed to map the global column-averaged CO₂ dry-air mixing ratio (X_{CO₂}) in order to characterize CO₂ sources and sinks on regional scales [Kuang *et al.*, 2002; Crisp *et al.*, 2004]. The OCO-2 instrument features high precision, small footprint, and global coverage. It is ideal for studying the global carbon cycle. Since CO₂ is well mixed in the atmosphere, CO₂ flux inversion typically requires retrieval accuracy up to 1 ppm [Miller *et al.*, 2007]. Such data could significantly reduce the uncertainties in the regional CO₂ flux estimation [Rayner and Brien, 2001]. However, any X_{CO₂} retrieval errors larger than the accuracy requirement would lead to significant biases in the flux inversion.

Aerosol scattering is often considered the major source of error in the remote sensing of greenhouse gases [Aben *et al.*, 2007]. Scattering in the atmosphere could change the photon path distribution, thus altering the apparent absorption of the target trace gas [Oshchepkov *et al.*, 2008]. There are many recent studies on the CO₂ retrieval errors related to aerosol scattering. For example, Houweling *et al.* [2005] examined the Scanning Imaging Absorption Spectrometer for Atmospheric

Chartography (SCIAMACHY) CO₂ retrieval and found a bias of up to 10% over the Sahara Desert. *Uchino et al.* [2012] compared the Greenhouse Gases Observing Satellite (GOSAT) retrievals with Total Carbon Column Observing Network (TCCON) and lidar measurements over Tsukuba, and identified high-altitude aerosols and thin cirrus clouds as the major sources of error.

The surface albedo has often the most significant effect on the reflected radiance observed at top of atmosphere even in the presence of aerosol scattering. The concept of critical surface albedo (α_c) was first proposed by *Fraser and Kaufman* [1985]. Intuitively, increasing AOD could either increase or decrease the top of atmosphere reflectance as the aerosols appear to be brighter (such as sulfate) or darker (such as soot) than the surface. The critical surface albedo is defined as the albedo where the derivative of the top of atmosphere radiance with respect to AOD is equal to zero in the continuum [*Seidel and Popp*, 2012]. In the continuum, clear sky gaseous absorption optical depth is zero. A surface with albedo close to α_c could cause large errors in the retrieval of AOD from space, since the radiance measurement loses sensitivity to the variation of AOD. The concept of critical surface albedo has been extensively applied in the retrieval of surface and aerosol properties [e.g. *Banks et al.*, 2013; *Sayers et al.*, 2013]. However, it is less well known in the field of greenhouse gas retrieval. While aerosols are hard to detect over a surface with albedo close to α_c , they can change the photon path length and therefore influence the retrieval of greenhouse gas column abundances.

The aim of this paper is to test the hypothesis that the OCO-2 X_{CO₂} retrieval errors over desert regions are due to the albedo being close to the critical surface

albedo. In Section 3.2, we examine the OCO-2 version 7 data to identify regions with large X_{CO_2} retrieval errors. In Section 3.3, we employ a two-stream-exact single scattering (2S-ESS) radiative transfer model to study the physical mechanism of the X_{CO_2} retrieval errors over a surface with albedo close to α_c . A discussion of our results follows in Section 3.4.

3.2. X_{CO_2} retrieval errors over deserts

In this section, we study the OCO-2 retrieval error over desert regions where surface albedos are high. Online Version 7r data are used in the study (<http://oco.jpl.nasa.gov/science/ocodatacenter/>). In the OCO-2 dataset, retrieval quality is labeled with two ‘flags’: 0. 'Passed internal quality check'; 1. 'Failed internal quality check'. In Figure 3.1, we plot all the X_{CO_2} retrievals in April 2015. Currently, OCO-2 gathers as many as 72,000 spectra on the sunlit side of any single orbit, or 24 per second [Mandrake *et al.*, 2014]. Monthly data are enough for global coverage. By comparing Figure 3.1a and Figure 3.1b, we find that most of the data points that fail to pass the quality check are located over desert regions such as the Sahara Desert and Central Asia. X_{CO_2} retrievals over these regions show significant low biases compared with surrounding areas. Since the deserts are unlikely to be a significant sink of CO_2 , X_{CO_2} retrieval bias over these regions appears to be an artifact.

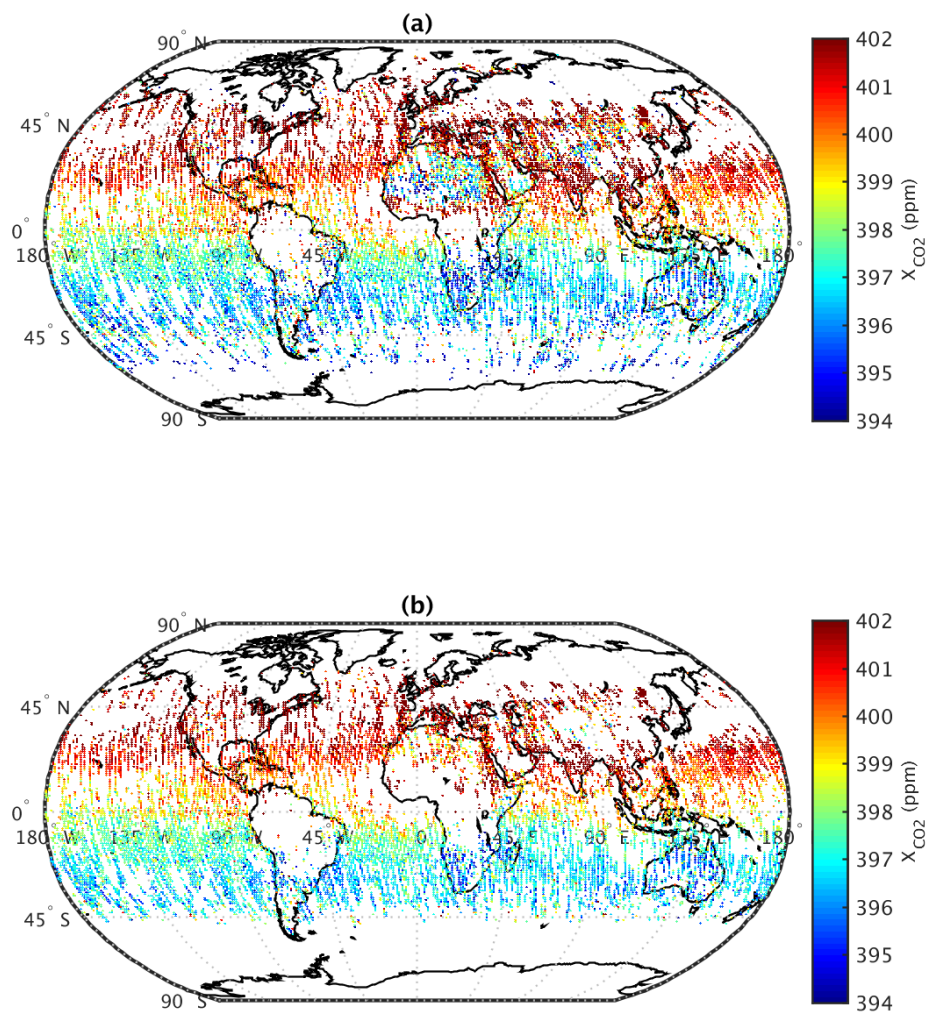


Figure 3.1 Global map of OCO-2 XCO₂ retrieval in April 2015. (a) All the data points are displayed. In OCO-2 retrievals, data qualities are labeled with 'flag' 0 and 1: 0. 'Passed internal quality check'; 1. 'Failed internal quality check'. (b) Only the data points labeled with 'flag 0' are displayed.

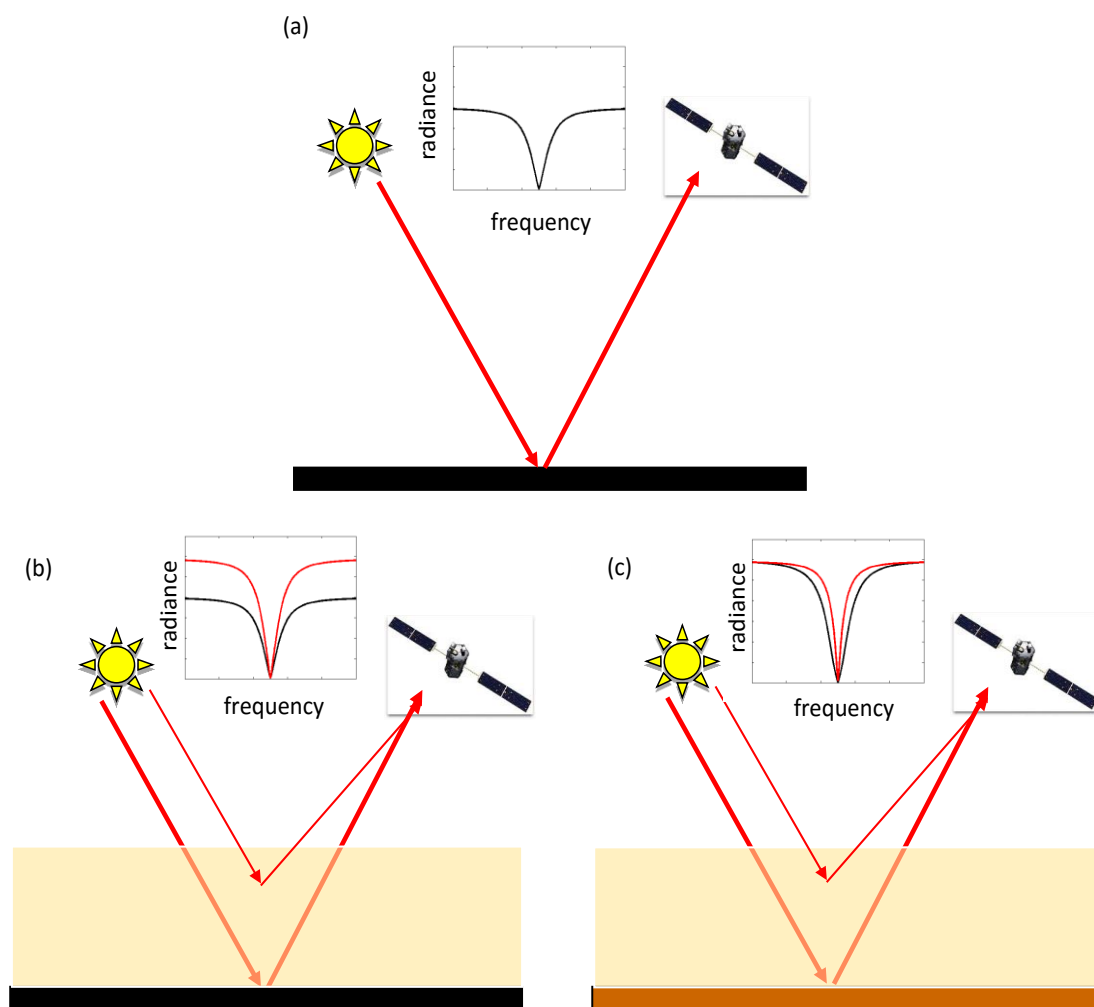


Figure 3.2 Schematic figures of reflection and scattering over surfaces with difference albedos. The small window at the top of each panel shows the one-line absorption spectra. Black spectra represent the reflection in a clear scenario over a dark surface. Red spectra represent the reflection and scattering in a hazy scenario. (a) Clear scenario, $AOD = 0$. (b) Scattering over a dark surface. (c) Scattering over a surface with albedo close to α_c .

We will examine the hypothesis that the retrieval errors over desert regions are due to the albedo being close to the critical surface albedo. The concept of critical surface albedo is explained in Figure 3.2. The three panels represent (a) clear scenario, (b) scattering over a low albedo surface, and (c) scattering over a surface with albedo close to α_c . Schematic figures of one-line spectra are also shown in each panel. Intuitively, bright aerosols over a dark surface would increase the radiance in the continuum, as shown in Figure 3.2b. The presence of such aerosols is very easy to detect from the shift of the continuum radiance. However, over a critical surface albedo region, as shown in Figure 3.2c, increasing the AOD does not change the absolute radiance in the continuum. Aerosols can cause changes in the photon path length through the atmosphere, thereby modifying the apparent absorption. The net result is the filling-in of the absorption lines, while the continuum remains the same. This effect is the same for all absorption lines. Quantitatively, it can be derived from our analytic model presented in Chapter 2. We will demonstrate in the next section that over such a surface with albedo close to α_c , the effect of changing AOD is almost the same as that caused by changing absorbing gas column abundance. Over such regions, the interference between aerosol scattering and CO₂ absorption will cause degeneracy in the retrieval of AOD and CO₂, leading to a large error in the X_{CO₂} retrieval.

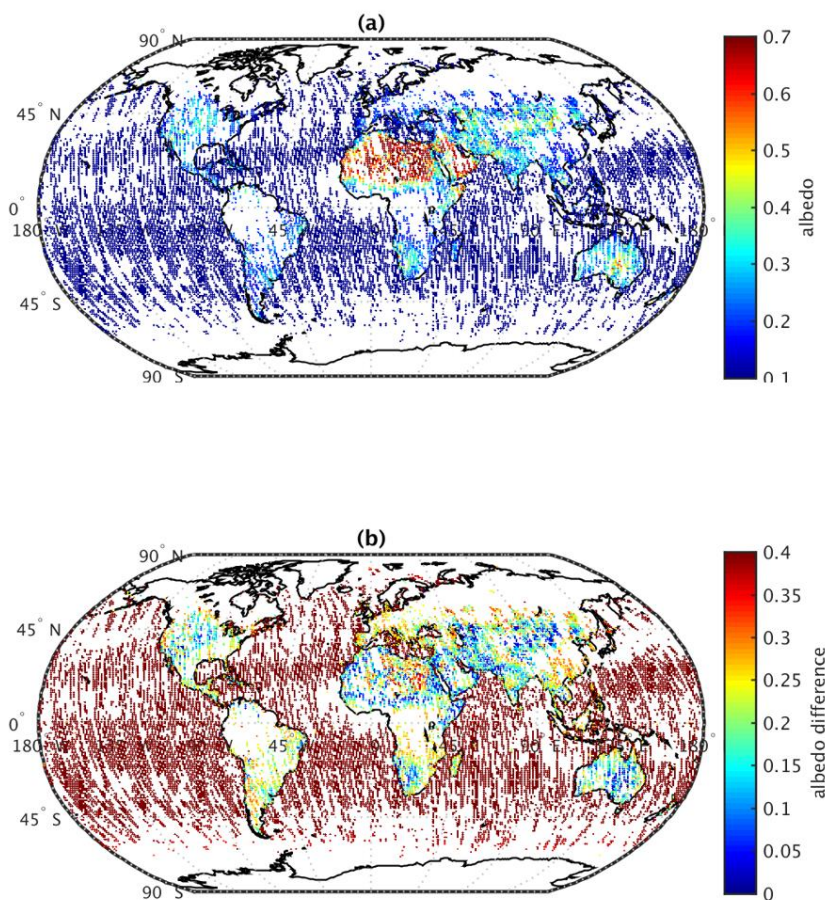


Figure 3.3 (a) Global map of the retrieved surface albedo in the 1.6 μm weak CO₂ band in April 2015. (b) Difference between the retrieved surface albedo and the critical surface albedo of 0.46. Differences are displayed in absolute values. We assume that the aerosol has mineral dust properties with SSA = 0.94. The aerosol SSA is defined as the ratio between the scattering optical depth and the total extinction optical depth. In Section 3.3, we use the same surface albedo for all the absorption bands in the simulations.

To confirm our hypothesis that the retrieval errors are caused by the surface albedo being close to the critical value, we examine the surface albedo in Figure 3.3. Figure 3.3a shows the retrieved surface albedo in the CO₂ 1.6 μm weak band and Figure 3.3b shows the difference between the retrieved surface albedo and the critical surface albedo of 0.46, a value that is estimated in the next section using the 2S-ESS model. In the calculation of the critical surface albedo, we assume that the aerosol has mineral dust properties over the desert with single scattering albedo (SSA) = 0.94 [Kahn *et al.*, 2005]. The critical surface albedo corresponding to mineral dust is much higher than the ocean albedo and is also higher than land albedos in most areas. Figure 3.3 shows that the only areas with such high albedos are deserts, where the X_{CO₂} retrieval errors are large.

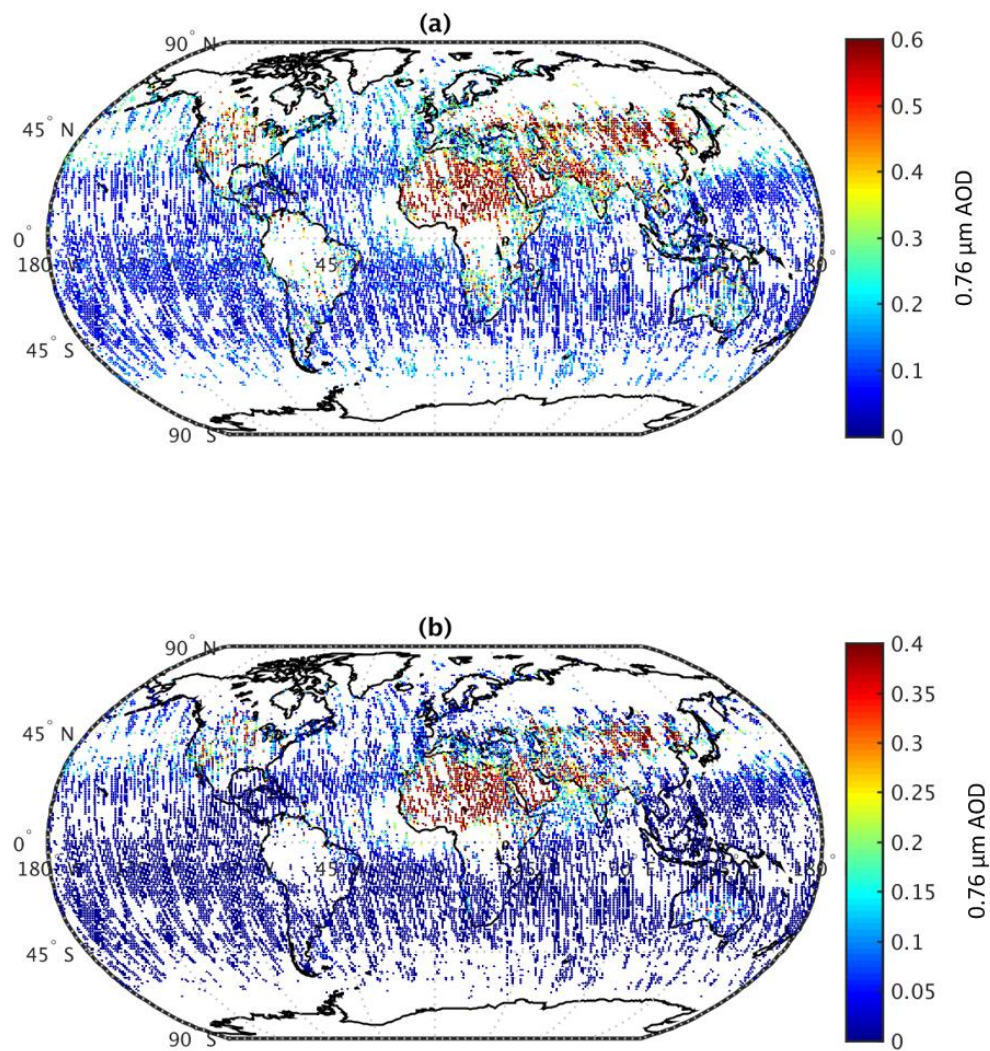


Figure 3.4 (a) Global map of the OCO-2 total AOD retrieval in April 2015. AOD values are shown in the O₂ 0.76 μm absorption band. (b) Same as a, but for ‘type 1’ aerosol in the OCO-2 retrieval [O’Dell *et al.*, 2012], i.e. mineral dust [Kahn *et al.*, 2005].

It is well known that AOD can be large over desert regions due to wind and dust [Houweling *et al.*, 2005]. We plot the total AOD and the retrieved mineral dust AOD from the OCO-2 product in Figure 3.4. AOD values are shown in the O₂ 0.76 μm absorption band. Over the deserts, we suspect that the AOD retrieval is biased. Since mineral dust aerosol acts to change the photon path length [Houweling *et al.*, 2005], the CO₂ column abundance retrieval would also be biased, as shown in Figure 3.1. There are several reasons that lead us to attribute the X_{CO₂} retrieval errors to the interaction between AOD and critical surface albedo, instead of the large AOD alone.

1. Desert is not the only region with high aerosol loadings. Over other regions with high pollution levels and large AOD, such as megacities in the eastern US and China, the X_{CO₂} retrievals have much lower biases than those over desert regions.
2. Due to atmospheric circulation, dust aerosol over the Sahara Desert extends far into the Atlantic Ocean, as seen in the MODIS product [See Figure 1b in Houweling *et al.*, 2005 and Figure 8 in Remer *et al.*, 2008]. However, in Figure 3.1 and Figure 3.4, we see a clear contrast in the X_{CO₂} and AOD retrievals between the ocean and the land on the boundary of the African continent. The X_{CO₂} retrieval differences between the land and the adjacent ocean are most evident near the Sahara Desert. We assume that such differences in the OCO-2 product are unrealistic, although ocean retrievals are done using glint mode and land retrievals using nadir mode. We don't observe such discontinuities in other regions.

3. We examine the regions in Figure 3.1b where the X_{CO_2} retrieval fails to pass the quality check or shows a low bias, and the regions in Figure 3.3b where the surface albedo is very close to the critical surface albedo relevant to mineral dust. The two regions coincide to a large extent.

3.3. Radiative transfer modeling

The concept of critical surface albedo can be explained by a numerically efficient 2S-ESS radiative transfer model [Spurr and Natraj, 2011]. This model is better than a traditional numerical two-stream model in that the singly scattered radiation is computed exactly, while the two-stream approximation is used only for the multiply scattered radiation. It has been used in several previous studies on the remote sensing of greenhouse gases [e.g. Xi *et al.*, 2015; Zhang *et al.*, 2015]. We use a typical model atmosphere derived from the NCEP-NCAR reanalysis data [Kalnay *et al.*, 1996]. The model atmosphere includes 70 layers from the surface to the top of atmosphere. Absorption coefficients for all absorbing gases are obtained from the HITRAN database [Rothman *et al.*, 2008]. Rayleigh scattering is included in the calculation. To simulate OCO-2 nadir observations in the mid-latitude, we assume that the viewing zenith angle is zero, while the solar zenith angle is set to 45° . The incoming solar flux is assumed to be unity for all wavelengths (we effectively calculate the dimensionless reflectance). Aerosol scattering in this model is isotropic. The AOD is distributed evenly within the boundary layer below 800 hPa. The isotropic scattering assumption is equivalent to the Delta-Eddington approximation of a more realistic forward-peaked dust aerosol phase function

[Wiscombe, 1976]. This assumption has minor impact on the accuracy of radiative transfer calculation, and does not influence the conclusions in this study with respect to surface albedo and SSA. Figure 3.5a-c shows the simulated spectra in the 2.0 μm strong CO_2 band, 1.6 μm weak CO_2 band, and 0.76 μm $\text{O}_2\text{-A}$ band. Water vapor absorption is not included in this model.

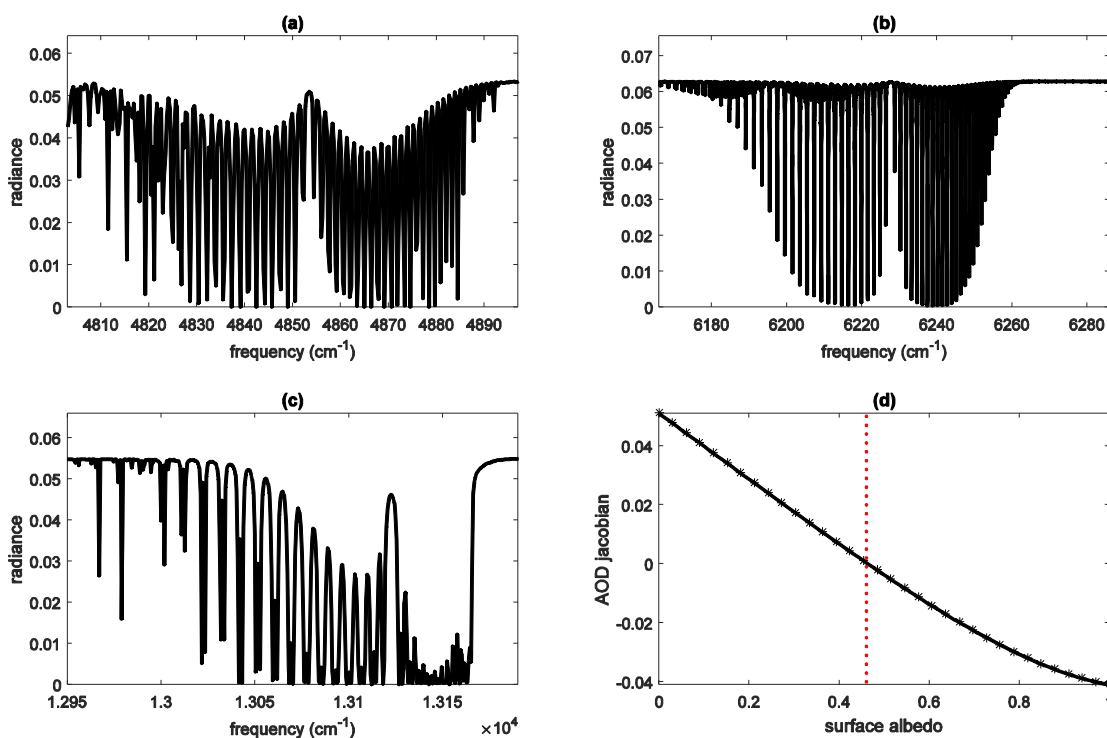


Figure 3.5 (a) Spectrum of 2.0 μm strong CO_2 band. (b) Spectrum of 1.6 μm weak CO_2 band. (c) Spectrum of 0.76 μm weak $\text{O}_2\text{-A}$ band. (d) AOD Jacobian in the continuum as a function of surface albedo. The critical surface albedo (0.46) is marked by the red dotted line.

Intuitively, increasing AOD in the atmosphere will change the continuum radiance since aerosol scattering changes the apparent albedo. We assume that the aerosol SSA is fixed for mineral dust; however, the surface albedo may vary widely

across different regions. Figure 3.5b shows the variation of the AOD Jacobian (derivative of radiance with respect to AOD) in the continuum of the 1.6 μm weak CO_2 band as a function of surface albedo. Mineral dust aerosol increases the apparent albedo over a dark surface and decreases the apparent albedo over a bright surface. Of interest, then, is the transition point at which the derivative of the radiance with respect to AOD changes sign (Equation 3.1). In Figure 3.5b, this point is marked by the dotted red line ($\alpha_c = 0.46$). Mathematically we can derive it as follows:

$$\frac{\partial R(\text{AOD}, \alpha_c)}{\partial \text{AOD}} = 0 \quad (3.1)$$

Equation 3.1 can be solved numerically using a radiative transfer model. As shown in *Seidel and Popp* [2012], α_c is primarily a function of aerosol SSA. Aerosols with larger SSA correspond to larger critical surface albedo values. In addition, the value of α_c is also associated with many other factors such as viewing geometry and aerosol height distribution.

In an optically thick atmosphere, the value of α_c can be roughly estimated as the reflectance of an infinitely thick atmosphere [*Goody and Yung*, 1989]:

$$\alpha_c = R_{\text{inf}}(\omega_0) = \frac{1 - \sqrt{1 - \omega_0}}{1 + \sqrt{1 - \omega_0}} \quad (3.2)$$

where ω_0 is the aerosol SSA. This is based on the assumption that the incoming solar flux is approximated by an isotropic diffusive flux in the atmosphere. Equation 3.2 gives a simple analytic relationship between α_c and ω_0 . The critical surface albedo is a monotonically increasing function of aerosol SSA, which is

consistent with the numerical results in *Seidel and Popp* [2012] and *Wells* [2012]. However, in an optically thin atmosphere, Equation 3.2 would overestimate the value of α_c . In this case, the critical surface albedo needs to be solved numerically using a realistic radiative transfer model.

The aerosol SSA is defined as the ratio between the scattering optical depth and the total extinction optical depth. Within the absorption line, gaseous absorption must be added on to the aerosol extinction optical depth; therefore, the relationship between SSA and critical surface albedo no longer holds. An important implication is that, if the surface albedo approaches the critical value, it is difficult to retrieve AOD. In this scenario, the sensitivity of the reflected radiance to AOD will decrease, and retrieval errors for both AOD and CO₂ will increase (Figure 3.2).

In an atmosphere with both aerosol scattering and gaseous absorption, this relationship for the critical surface albedo only holds in the continuum. Within the absorption line, the derivative of radiance with respect to AOD is not zero. In Figure 3.6, we zoom in on a single absorption line in the 1.6 μm weak CO₂ band and calculate the Jacobians with respect to AOD and CO₂ total column (scaling factor) over a low albedo surface and a surface with albedo close to α_c . Over a low albedo surface, increasing AOD has two effects: 1. increasing the radiance as the aerosol appears to be brighter than the surface; 2. changing the apparent absorption as the scattering modifies the photon path length. In Figures 3.6c and 3.6d, the AOD and CO₂ Jacobians are easy to distinguish. However, over a surface with albedo close to α_c , increasing AOD does not change the radiance in the continuum. In this scenario, the only effect of aerosol scattering is to change the apparent absorption.

Therefore, the AOD and CO₂ Jacobians, as shown in Figures 3.6a and 3.6b respectively, have almost the same shape. At low spectral resolution, the signals from AOD and CO₂ would not be distinguishable in the observations.

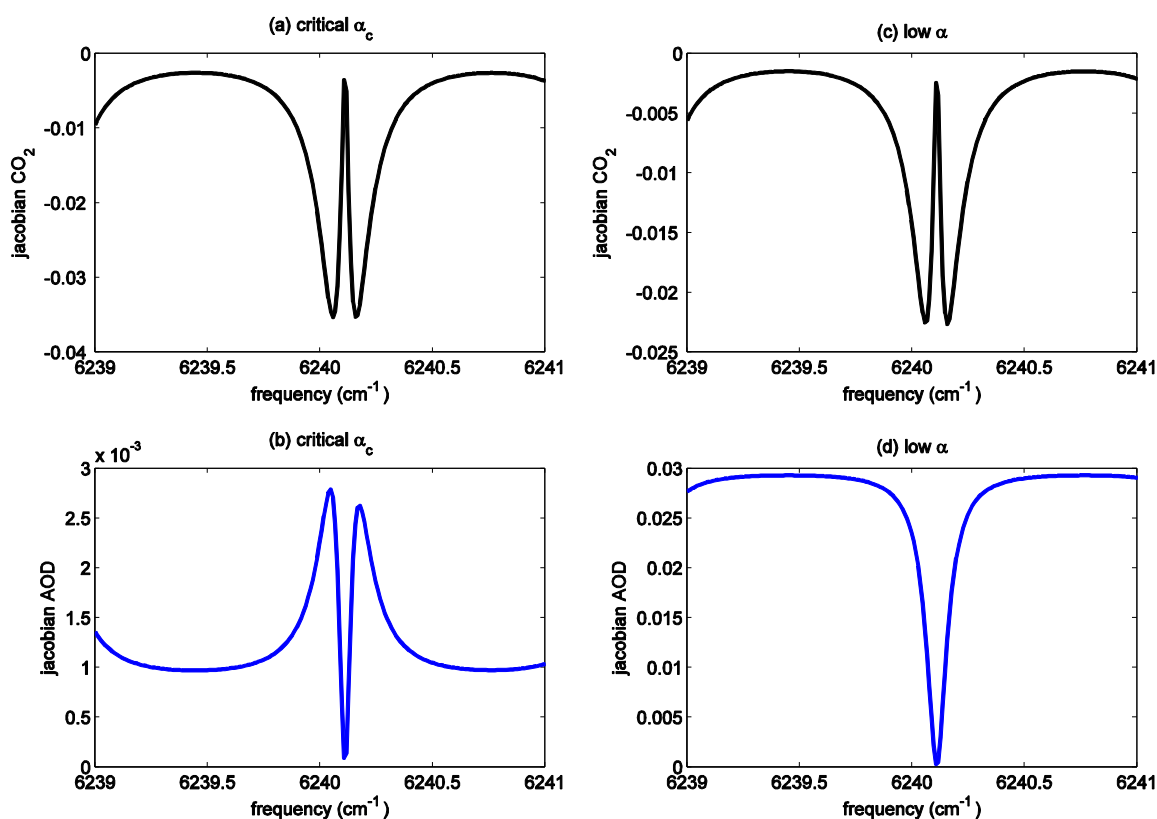


Figure 3.6 Jacobians of CO₂ and AOD in a single line, generated by the 2S-ESS model. (a) Jacobian of CO₂ total column over a surface with albedo close to α_c (0.46). (b) Jacobian of AOD over a surface with albedo close to α_c (0.46). (c) Same as (a), but over a low albedo (0.2) surface. (d) Same as (b), but over a low albedo (0.2) surface.

Using the 2S-ESS model, we can study the retrieval error caused by the surface albedo being close to the critical value. Here, retrieval error is defined as the difference between the retrieved state variables and the truth. It is different from

the posterior error, which is computed from the *a posteriori* covariance and depends only on the measurement noise. OCO-2 uses an optimal estimation approach to retrieve X_{CO_2} and other state vector variables [Rodgers, 2000] based on minimizing the following cost function:

$$\chi^2 = [\mathbf{x}_i - \mathbf{x}_a]^T \mathbf{S}_a^{-1} [\mathbf{x}_i - \mathbf{x}_a] + [\mathbf{y} - \mathbf{F}(\mathbf{x}_i)]^T \mathbf{S}_e^{-1} [\mathbf{y} - \mathbf{F}(\mathbf{x}_i)], \quad (3.3)$$

where \mathbf{x}_i is the state vector, \mathbf{x}_a is the *a priori* state vector, $\mathbf{F}(\mathbf{x})$ is the forward model, \mathbf{y} is the measurement, \mathbf{S}_a is the *a priori* covariance matrix, and \mathbf{S}_e is the measurement error covariance matrix.

We use two quantities to determine the retrieval quality and precision: degrees of freedom (d) and information content (H). They are calculated using Equations 3.4 – 3.5.

$$d = \sum_i \lambda_i^2 / (1 + \lambda_i^2), \quad (3.4)$$

$$H = \frac{1}{2} \ln(|(\mathbf{K}^T \mathbf{S}_e^{-1} \mathbf{K} + \mathbf{S}_a^{-1}) \mathbf{S}_a|), \quad (3.5)$$

where \mathbf{K} is the jacobian matrix with respect to CO_2 and AOD, and $\{\lambda_i\}$ are the singular values of the normalized jacobian $\mathbf{S}_e^{-\frac{1}{2}} \mathbf{K} \mathbf{S}_a^{\frac{1}{2}}$. Degree of freedom and information content measure, respectively, how many independent pieces of information we can obtain from the measurements, and how much the estimation of the state vector can be improved given the information from the measurement.

To simplify the problem, we set up a retrieval scheme assuming that only three state variables are included in the state vector, i.e. total column CO_2 (scaling factor), AOD, and surface pressure. In the calculation, their *a priori* uncertainties are

arbitrarily assumed to be 20%, 100%, and 0.4%, respectively. They are consistent with the retrieval algorithm shown in *O'Dell et al.* [2012]. We assume that the three state variables are not correlated. Therefore, the *a priori* covariance matrix \mathbf{S}_a is diagonal. The Jacobian matrix \mathbf{K} is calculated using finite differences, and the measurement error covariance matrix \mathbf{S}_e is defined according to the signal to noise ratio (SNR). We employ the Levenberg-Marquardt (LM) algorithm [*Rodgers, 2000*] to minimize the cost function. The iteration in this algorithm is:

$$\mathbf{x}_{i+1} = \mathbf{x}_i + [(1 + \gamma)\mathbf{S}_a^{-1} + \mathbf{K}_i^T \mathbf{S}_e^{-1} \mathbf{K}_i]^{-1} \{ \mathbf{K}_i^T \mathbf{S}_e^{-1} [\mathbf{y} - \mathbf{F}(\mathbf{x}_i)] - \mathbf{S}_a^{-1} [\mathbf{x}_i - \mathbf{x}_a] \} \quad (3.6)$$

where γ is the parameter determining the size of each iteration step. In the retrieval tests, we generate synthetic measurements using the 2S-ESS model within the three absorption bands, as shown in Figure 3.5a-c. For simplicity, surface albedo and AOD are the same for all the three bands. We employ a spectral resolution of 0.3 cm^{-1} in the weak and strong CO_2 absorption bands, and 0.6 cm^{-1} in the O_2 -A band. SNR is set to be 100. Gaussian white noise is added to the synthetic data. The SNR used in the retrieval tests is lower than the OCO-2 instrument SNR [*Frankenberg et al., 2015*]. In addition to the radiometric noise, it includes other sources of error such as uncertainties in the HITRAN spectroscopic parameters and unresolved solar lines. We assume that the *a priori* and first guess values of X_{CO_2} , AOD, and surface pressure are 380 ppm, 0.3, and 998 hPa, respectively. These values are different from the truth, which are 400 ppm for X_{CO_2} , 0.6 for AOD, and 1000 hPa for surface pressure.

Retrieval results for different values of surface albedo are listed in Table 1. We evaluate the error in the retrieved X_{CO_2} over three scenarios: a low albedo surface ($\alpha=0.2$), a surface with albedo close to α_c ($\alpha_c=0.46$), and a high albedo surface

($\alpha=0.9$). All parameters are the same for the three cases except for the surface albedo. Over a surface with albedo close to α_c , the retrieval of the three state variables suffers from degeneracy. Further, the errors in the retrieved X_{CO_2} can be as large as 3.2 ppm over a surface with albedo close to α_c , while retrieval errors over a high or low albedo surface are about 1 ppm. The large X_{CO_2} retrieval error over a surface with albedo close to α_c is related to the inaccurate AOD retrieval, which is mainly due to the loss of degrees of freedom and information content.

Table 3.1. Retrieval tests using the 2S-ESS model

	X_{CO_2} error	AOD error	Surface pressure error	d	H
low albedo (0.2)	0.97	0.0008	-0.41	2.843	11.82
critical albedo (0.46)	3.22	-0.1018	-6.22	2.565	8.09
high albedo (0.9)	1.09	0.0009	-1.89	2.850	11.12

X_{CO_2} errors are in ppm. Surface pressure errors are in hPa. Errors are defined as the difference between the retrieved state variables and the truth (retrieved - truth).

3.4. Discussions and conclusions

We have analyzed the X_{CO_2} retrieval errors over deserts, and attributed the errors to the surface albedo being close to the critical value, α_c . It is apparent that such errors,

if not taken into account, could cause large biases in the inversion of CO₂ sources and sinks. The 2S-ESS radiative transfer model provides clear insights into the physical mechanism of aerosol scattering over a surface with albedo close to α_c . In this study, the value of α_c is determined in the 1.6 μm weak CO₂ band. Surface albedos in the strong CO₂ band and O₂-A band do not necessarily satisfy the condition of critical surface albedo. Even by using all the three measured bands, we still see a significant increase in the X_{CO_2} retrieval error when the surface albedo in the weak CO₂ band is close to α_c . The transition of retrieval error from a low/high surface albedo to the critical surface albedo is a smooth function. There is a significant increase in the retrieval error, and a loss of degrees of freedom, if the surface albedo falls within $\alpha_c \pm 0.1$ (Figure 3.8). We use a 2S-ESS model in this study because it is simple and can reveal the basic physics of the impact of critical albedo on X_{CO_2} retrieval. We plan to explore a more realistic model in future collaborative work with the OCO-2 retrieval team.

In addition to the interaction between aerosol scattering and critical surface albedo, there are many other sources of error in the X_{CO_2} retrieval, such as cirrus clouds, uncertainties in the spectroscopic parameters, and large solar zenith angles. In Figure 3.1, we also identify large retrieval errors in high latitude regions and over South America. However, these errors are probably not related to surface albedo. Retrieval errors over these regions warrant further investigation.

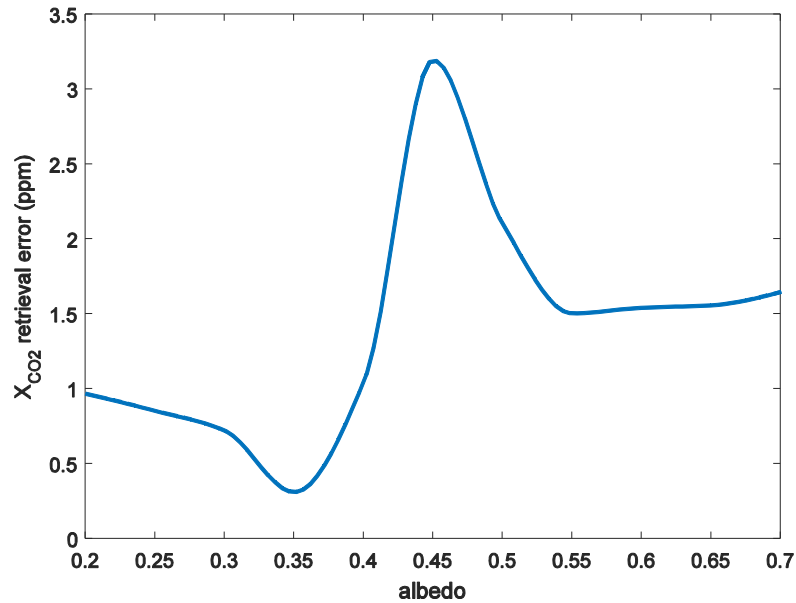


Figure 3.7 X_{CO_2} retrieval error as a function of surface albedo. The same retrieval test as shown in Table 3.1 has been done at various surface albedos.

The problem over a surface with albedo close to α_c is essentially a degeneracy in the retrieval. This idea is also tested using the analytic model we presented in Chapter 2. Although the magnitude of the AOD Jacobian is small over such a surface, its signal is almost identical to the CO_2 mixing ratio Jacobian, which leads to a loss of degrees of freedom and information content. In this scenario, the information on AOD mainly comes from the *a priori* and its retrieval has large smoothing errors. This error in the AOD retrieval will change the photon path length and influence the X_{CO_2} retrieval. We have tested synthetic data by retrieving them using the 2S-ESS model. We see a large X_{CO_2} error over a surface with albedo close to α_c , when the AOD *a priori* deviates away from the true value.

To reduce the error, we need to bring in additional information to constrain aerosol properties. If we use more accurate AOD *a priori* information and apply a stronger *a priori* constraint, X_{CO_2} retrievals over surfaces with albedo close to α_c could be improved. Given the same error in AOD estimation, the X_{CO_2} retrieval error over a surface with albedo close to α_c could be even smaller than that over a high or low albedo surface, since the jacobian of AOD over a surface with albedo close to α_c is smaller. One possible solution is to fix the surface pressure at the ECMWF [Uppala *et al.*, 2005] reanalysis value and retrieve AOD using the O_2 absorption band [Sanghavi *et al.*, 2012]. When the O_2 column abundance is known, aerosol information can be obtained from the O_2 absorption lines. Zhang *et al.* [2015] has proposed a similar solution for the retrieval of X_{CO_2} from the California Laboratory for Atmospheric Remote Sensing (CLARS) measurements. Since the ECMWF surface pressure reanalysis data is very accurate [Ponte and Dorandeu, 2003], it should be acceptable to fix the surface pressure. Retrieval tests similar to those shown in Table 1 have been done to confirm that aerosol information from the O_2 -A band could significantly reduce the X_{CO_2} retrieval error over a surface with albedo close to α_c . For OCO-2, we still need an accurate estimate of the Ångström coefficient to translate the AOD in the O_2 -A band to a value that is relevant to the weak CO_2 band. Alternatively, information on aerosols and surface albedo from other satellites, such as MISR and MODIS [Kahn *et al.*, 2005; Liang *et al.*, 2002], could also be employed to improve OCO-2 retrievals.

Bibliography:

- Aben, I., Hasekamp, O., Hartmann, W., 2007. Uncertainties in the space-based measurements Of CO₂ columns due to scattering in the Earth's atmosphere. *Journal of Quantitative Spectroscopy & Radiative Transfer* 104, 450-459.
- Banks, J.R., Brindley, H.E., Flamant, C., Garay, M.J., Hsu, N.C., Kalashnikov, O.V., Kluser, L., Sayer, A.M., 2013. Intercomparison of satellite dust retrieval products over the west African Sahara during the Fennec campaign in June 2011. *Remote Sensing of Environment* 136, 99-116.
- Crisp, D., Atlas, R.M., Breon, F.M., Brown, L.R., Burrows, J.P., Ciais, P., Connor, B.J., Doney, S.C., Fung, I.Y., Jacob, D.J., Miller, C.E., O'Brien, D., Pawson, S., Randerson, J.T., Rayner, P., Salawitch, R.J., Sander, S.P., Sen, B., Stephens, G.L., Tans, P.P., Toon, G.C., Wennberg, P.O., Wofsy, S.C., Yung, Y.L., Kuang, Z.M., Chudasama, B., Sprague, G., Weiss, B., Pollock, R., Kenyon, D., Schroll, S., 2004. The orbiting carbon observatory (OCO) mission. *Trace Constituents in the Troposphere and Lower Stratosphere* 34, 700-709.
- Frankenberg, C., Pollock, R., Lee, R.A.M., Rosenberg, R., Blavier, J.F., Crisp, D., O'Dell, C.W., Osterman, G.B., Roehl, C., Wennberg, P.O., Wunch, D., 2015. The Orbiting Carbon Observatory (OCO-2): spectrometer performance evaluation using pre-launch direct sun measurements. *Atmos Meas Tech* 8, 301-313.
- Fraser, R. S., and Y. J. Kaufman, 1985. The Relative Importance of Aerosol Scattering and Absorption in Remote-Sensing, *Ieee T Geosci Remote*, 23(5), 625-633.

- Goody, R.M., Yung, Y.L., 1989. Atmospheric Radiation: Theoretical Basis, Second Edition. Oxford University Press.
- Houweling, S., Hartmann, W., Aben, I., Schrijver, H., Skidmore, J., Roelofs, G.J., Breon, F.M., 2005. Evidence of systematic errors in SCIAMACHY-observed CO₂ due to aerosols. *Atmospheric Chemistry and Physics* 5, 3003-3013.
- Kahn, R.A., Gaitley, B.J., Martonchik, J.V., Diner, D.J., Crean, K.A., Holben, B., 2005. Multiangle Imaging Spectroradiometer (MISR) global aerosol optical depth validation based on 2 years of coincident Aerosol Robotic Network (AERONET) observations. *Journal of Geophysical Research-Atmospheres* 110.
- Kalnay, E., Kanamitsu, M., Kistler, R., Collins, W., Deaven, D., Gandin, L., Iredell, M., Saha, S., White, G., Woollen, J., Zhu, Y., Chelliah, M., Ebisuzaki, W., Higgins, W., Janowiak, J., Mo, K.C., Ropelewski, C., Wang, J., Leetmaa, A., Reynolds, R., Jenne, R., Joseph, D., 1996. The NCEP/NCAR 40-year reanalysis project. *B Am Meteorol Soc* 77, 437-471
- Kuang, Z.M., Margolis, J., Toon, G., Crisp, D., Yung, Y., 2002. Spaceborne measurements of atmospheric CO₂ by high-resolution NIR spectrometry of reflected sunlight: An introductory study. *Geophysical Research Letters* 29.
- Liang, S.L., Fang, H.L., Chen, M.Z., Shuey, C.J., Walthall, C., Daughtry, C., Morisette, J., Schaaf, C., Strahler, A., 2002. Validating MODIS land surface reflectance and albedo products: methods and preliminary results. *Remote Sensing of Environment* 83, 149-162.
- Mandrake, L., Frankenberg, C., O'Dell, C.W., Osterman, G., Wennberg, P., Wunch,

- D., 2013. Semi-autonomous sounding selection for OCO-2. *Atmos Meas Tech* 6, 2851-2864.
- Miller, C.E., Crisp, D., DeCola, P.L., Olsen, S.C., Randerson, J.T., Michalak, A.M., Alkhaled, A., Rayner, P., Jacob, D.J., Suntharalingam, P., Jones, D.B.A., Denning, A.S., Nicholls, M.E., Doney, S.C., Pawson, S., Boesch, H., Connor, B.J., Fung, I.Y., O'Brien, D., Salawitch, R.J., Sander, S.P., Sen, B., Tans, P., Toon, G.C., Wennberg, P.O., Wofsy, S.C., Yung, Y.L., Law, R.M., 2007. Precision requirements for space-based X-CO₂ data. *Journal of Geophysical Research-Atmospheres* 112.
- O'Dell, C.W., Connor, B., Bosch, H., O'Brien, D., Frankenberg, C., Castano, R., Christi, M., Crisp, D., Eldering, A., Fisher, B., Gunson, M., McDuffie, J., Miller, C.E., Natraj, V., Oyafuso, F., Polonsky, I., Smyth, M., Taylor, T., Toon, G.C., Wennberg, P.O., Wunch, D., 2012. The ACOS CO₂ retrieval algorithm - Part 1: Description and validation against synthetic observations. *Atmos Meas Tech* 5, 99-121.
- Oshchepkov, S., Bril, A., Yokota, T., 2008. PPDF-based method to account for atmospheric light scattering in observations of carbon dioxide from space. *Journal of Geophysical Research-Atmospheres* 113.
- Ponte, R.M., Dorandeu, J., 2003. Uncertainties in ECMWF surface pressure fields over the ocean in relation to sea level analysis and Modeling. *Journal of Atmospheric and Oceanic Technology* 20, 301-307.
- Rayner, P.J., O'Brien, D.M., 2001. The utility of remotely sensed CO₂ concentration data in surface source inversions. *Geophysical Research Letters*

28, 175-178.

Remer, L.A., Kleidman, R.G., Levy, R.C., Kaufman, Y.J., Tanre, D., Mattoo, S., Martins, J.V., Ichoku, C., Koren, I., Yu, H.B., Holben, B.N., 2008. Global aerosol climatology from the MODIS satellite sensors. *Journal of Geophysical Research-Atmospheres* 113.

Rodgers, C.D., 2000. *Inverse Methods for Atmospheric Sounding: Theory and Practice*. World Scientific Publishing Co. Pte. Ltd.

Rothman, L.S., Gordon, I.E., Barbe, A., Benner, D.C., Bernath, P.E., Birk, M., Boudon, V., Brown, L.R., Campargue, A., Champion, J.P., Chance, K., Coudert, L.H., Dana, V., Devi, V.M., Fally, S., Flaud, J.M., Gamache, R.R., Goldman, A., Jacquemart, D., Kleiner, I., Lacome, N., Lafferty, W.J., Mandin, J.Y., Massie, S.T., Mikhailenko, S.N., Miller, C.E., Moazzen-Ahmadi, N., Naumenko, O.V., Nikitin, A.V., Orphal, J., Perevalov, V.I., Perrin, A., Predoi-Cross, A., Rinsland, C.P., Rotger, M., Simeckova, M., Smith, M.A.H., Sung, K., Tashkun, S.A., Tennyson, J., Toth, R.A., Vandaele, A.C., Vander Auwera, J., 2009. The HITRAN 2008 molecular spectroscopic database. *Journal of Quantitative Spectroscopy & Radiative Transfer* 110, 533-572.

Sanghavi, S., J. V. Martonchik, J. Landgraf, and U. Platt (2012), Retrieval of the optical depth and vertical distribution of particulate scatterers in the atmosphere using O-2 A- and B-band SCIAMACHY observations over Kanpur: a case study, *Atmos Meas Tech*, 5(5), 1099-1119.

Sayer, A.M., Hsu, N.C., Bettenhausen, C., Jeong, M.J., 2013. Validation and uncertainty estimates for MODIS Collection 6 "Deep Blue" aerosol data.

- Journal of Geophysical Research-Atmospheres 118, 7864-7872.
- Seidel, F.C., Popp, C., 2012. Critical surface albedo and its implications to aerosol remote sensing. *Atmos Meas Tech* 5, 1653-1665.
- Spurr, R., Natraj, V., 2011. A linearized two-stream radiative transfer code for fast approximation of multiple-scatter fields. *J Quant Spectrosc Ra* 112, 2630-2637.
- Uchino, O., Kikuchi, N., Sakai, T., Morino, I., Yoshida, Y., Nagai, T., Shimizu, A., Shibata, T., Yamazaki, A., Uchiyama, A., Kikuchi, N., Oshchepkov, S., Bril, A., Yokota, T., 2012. Influence of aerosols and thin cirrus clouds on the GOSAT-observed CO₂: a case study over Tsukuba. *Atmospheric Chemistry and Physics* 12, 3393-3404.
- Uppala, S.M., Kallberg, P.W., Simmons, A.J., Andrae, U., Bechtold, V.D., Fiorino, M., Gibson, J.K., Haseler, J., Hernandez, A., Kelly, G.A., Li, X., Onogi, K., Saarinen, S., Sokka, N., Allan, R.P., Andersson, E., Arpe, K., Balmaseda, M.A., Beljaars, A.C.M., Van De Berg, L., Bidlot, J., Bormann, N., Caires, S., Chevallier, F., Dethof, A., Dragosavac, M., Fisher, M., Fuentes, M., Hagemann, S., Holm, E., Hoskins, B.J., Isaksen, L., Janssen, P.A.E.M., Jenne, R., McNally, A.P., Mahfouf, J.F., Morcrette, J.J., Rayner, N.A., Saunders, R.W., Simon, P., Sterl, A., Trenberth, K.E., Untch, A., Vasiljevic, D., Viterbo, P., Woollen, J., 2005. The ERA-40 re-analysis. *Q J Roy Meteor Soc* 131, 2961-3012.
- Wells, K.C., Martins, J.V., Remer, L.A., Kreidenweis, S.M., Stephens, G.L., 2012. Critical reflectance derived from MODIS: Application for the retrieval of

aerosol absorption over desert regions. *Journal of Geophysical Research-Atmospheres* 117.

Wiscombe, W.J., 1977. Delta-M Method - Rapid yet Accurate Radiative Flux Calculations for Strongly Asymmetric Phase Functions. *Journal of the Atmospheric Sciences* 34, 1408-1422.

Xi, X., Natraj, V., Shia, R.L., Luo, M., Zhang, Q., Newman, S., Sander, S.P., Yung, Y.L., 2015. Simulated retrievals for the remote sensing of CO₂, CH₄, CO, and H₂O from geostationary orbit. *Atmos. Meas. Tech.* 8, 4817-4830.

Zhang, Q., Natraj, V., Li, K.F., Shia, R.L., Fu, D.J., Pongetti, T.J., Sander, S.P., Roehl, C.M., Yung, Y.L., 2015. Accounting for aerosol scattering in the CLARS retrieval of column averaged CO₂ mixing ratios. *J Geophys Res-Atmos* 120, 7205-7218.

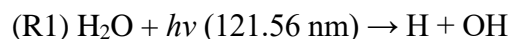
Chapter 4

RESOLVING MODEL-OBSERVATION DISCREPANCY IN THE MESOSPHERIC AND STRATOSPHERIC HO_x CHEMISTRY

4.1. Introduction

Odd hydrogen (HO_x) species, including hydroxyl radical (OH) and hydroperoxyl (HO₂), are important catalysts of odd oxygen in the middle atmosphere [Brasseur and Solomon, 2005]. Their profiles have been observed using balloon-based measurements [Jucks *et al.*, 1998], ground-based measurements [Cageao *et al.*, 2001; Li *et al.*, 2005], and space-borne measurements [Pickett, 2006]. Other measurement techniques include ground based microwave measurements; satellite or rocket-borne absorption spectroscopy etc. Since 2004, Aura Microwave Limb Sounder (MLS) has been providing high-quality OH and HO₂ measurements in the mesosphere and stratosphere [Livesey *et al.*, 2015; Pickett *et al.*, 2008].

The main source of middle atmospheric HO_x is direct photolysis of H₂O by the solar Lyman- α line in the mesospheric region (>60 km):



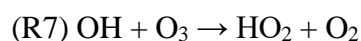
or the photolysis of O₃ and N₂O by solar UV below 200 nm and 330 nm, respectively, in the stratospheric region (<60 km) that produces O(¹D):



followed by:



OH is then converted to HO₂, and vice versa, via reactions with O, O₃ and NO:



Throughout the whole middle atmosphere, the ultimate sink of HO_x is by



[*Brasseur and Solomon, 2005; Canty and Minschwaner, 2002; Wang et al., 2015*]. It is clear from Reactions (1 – 3) that the net source of HO_x depends sensitively to the variations of incoming solar UV solar spectral irradiance (SSI) over the rotational (~27 days) and decadal (~11 years) time scales. From satellite observations, the HO_x species have been shown to better correlate with SSI than O₃ or temperature [*Rozanov et al., 2006*] and be good indicators of solar cycle with almost zero time lag [*Shapiro et al., 2012; Wang et al., 2015*].

Despite the simple HO_x photochemistry, a number of studies reveal discrepancies between observed and modeled HO_x concentrations. *Conway et al.* [2000] first claimed that the modeled stratospheric OH is lower than that observed by the Middle Atmosphere High Resolution Spectrograph Investigation (MAHRSI) [*Summers et al., 1997*] while the modelled mesospheric OH is higher. They thus coined the term “HO_x dilemma” to describe this discrepancy having opposite signs in the stratosphere

and mesosphere. However, this apparent dilemma has been attributed to large uncertainties of MAHRSI data at low altitudes [Englert *et al.*, 2008]. Using standard chemistry, Canty *et al.* [2006] found that a photochemical model overestimates the HO_x concentrations in the stratosphere; while Millan *et al.* [2015] concluded that the model shows a deficit in the mesospheric HO₂. By adjusting the kinetic rates of some important photochemical reactions, Canty *et al.* [2006], Pickett *et al.* [2008] and Siskind *et al.* [2013] show that the OH concentrations observed by MLS [Pickett *et al.*, 2006] and Spatial Heterodyne Imager for Mesospheric Radicals (SHIMMER) [Englert *et al.*, 2008] are consistent with the modelled concentration.

However, since there are tens, or sometimes hundreds, of important photochemical reactions in the middle atmosphere, the choice of which kinetic rates to be adjusted to fit the observation may not be unique and subjectively dependent on our prior knowledge. For example, Canty *et al.* [2006] adjusted the reaction rates for $\text{HO}_2 + \text{OH} \rightarrow \text{H}_2\text{O} + \text{O}_2$ and $\text{O} + \text{OH} \rightarrow \text{O}_2 + \text{H}$, while Siskind *et al.* [2013] adjusted the reaction rate for $\text{H} + \text{O}_2 + \text{M} \rightarrow \text{HO}_2 + \text{M}$. To overcome the degeneracy of possible choices, here we propose an objective Bayesian optimal estimation approach that accounts for both observational and model uncertainties when selecting and adjusting model parameters. The assumptions made in this approach is that both the state variable *a priori* and the measurements follow Gaussian distribution. This approach enables us to quantify degrees of freedom (DOF) of adjusting based on the sensitivity of middle atmospheric HO_x concentrations with respect to photochemical reactions [Rodgers, 2000].

In this paper, we perform a systematic sensitivity study of mesospheric and stratospheric HO_x chemistry with respect to chemical kinetic rates and O₂ molecular cross sections. In Section 4.2, we present the Caltech-JPL photochemical model and the optimal estimation method used to adjust several model parameters. In Section 4.3, results of the optimal estimation are shown. We identify the need for reconsideration of the laboratory data and recommended rate coefficients for the H + O₂ + M → HO₂ + M reaction. Discussions and conclusions follow in Section 4.4.

4.2. Model and method

MLS is an instrument on board the Aura spacecraft, which was launched in 2004 [*Waters et al.*, 2006]. Version 3.3 MLS data are used in this study. We choose a moderately strong solar activity period in June 2005 and only use the daytime data. The lifetime of HO_x in the mesosphere depends on the concentration of several key species, such as O, O₂, and O₃; but is generally much shorter than the time scale of vertical and horizontal transport. A period at the peak of solar activity would be desirable due to the correlation between OH concentration and solar UV flux, however, it is limited by the launched date of the Aura mission. The year of 2005 is right after the maximum solar activity year. Monthly mean tropical data averaged from 25°S to 25°N are used to calculate the mean OH and HO₂ profiles (Figure 4.1). Mean solar flux data are from the Naval Research Laboratory (NRL) model [*Lean*, 2000]. We focus on monthly mean profiles so the results are not affected by the 27-day solar cycle variabilities.

We employ the Caltech-JPL 1-D photochemical model KINETICS to simulate OH and HO₂ profiles in the stratosphere and mesosphere [Allen and Yung, 1981]. This model contains 66 levels from the surface to 130 km altitude. Vertical transports are parameterized using eddy diffusion. Model outputs are interpolated to 1:30 pm local time in order to be compared with the MLS daytime measurements. The model has been widely used for studying photochemistry on earth and other planets [e.g. Li *et al.*, 2014; Wang *et al.*, 2013]. All the reactions in this model are listed in the supplementary material.

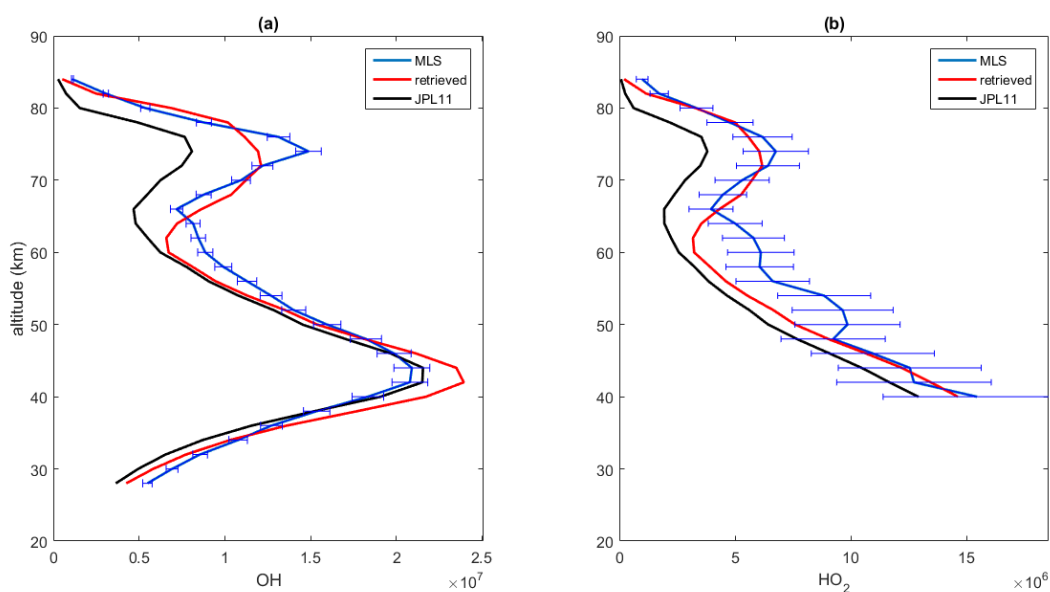


Figure 4.1. Comparison between MLS measurements (blue) and Caltech-JPL KINETICS model simulations (black and red). (a) OH concentration (cm⁻³). (b) HO₂ concentration (cm⁻³). MLS measurements are interpolated to the same pressure levels as KINETICS output and plotted as a function of altitude. Blue error bars indicate the MLS measurement uncertainties. In the comparison with the KINETICS model, MLS daytime measurements are averaged between 25°S to 25°N in latitude, and 06/01/2005 to 07/01/2005 in time. The black curve shows the model result using the

standard JPL 2011 chemistry. The red curve shows the model result using the adjusted reaction rates as shown in Table 4.1.

The goal of this study is to match the model simulation and MLS observations by adjusting a few important model parameters. Due to the simplicity of HO_x chemistry, we limit our parametric study to chemical reaction rate constants and absorption cross sections. Temperature-dependent bimolecular rate coefficients are given by:

$$k = A \exp\left(-\frac{E_a}{RT}\right) \quad (4.1)$$

where A is the collision frequency factor, hereafter referred to as reaction rate coefficient, E is the energy barrier for the reaction, T is temperature, and R = 8.31 J K⁻¹ mol⁻¹ is the gas constant. For each reaction, initial values of A and E_a/R are taken from the JPL 2011 data evaluation [Sander *et al.*, 2011], but only the A-factors are allowed to vary. For a termolecular reaction, k is expressed in terms of high- and low-pressure limiting values and their temperature dependences. We also only consider the reaction rate constant and scale the reaction rate at all pressure levels using the same factor.

In the Bayesian optimal estimation, we minimize the cost function, as shown in Equation 2, using Levenberg-Marquardt (LM) algorithm [Rodgers, 2000]. The method has been widely used for retrieving Level 2 data from the satellite-observed radiance. It is based on Bayesian approach assuming that both the measurements and the model parameters follow Gaussian distributions.

$$\chi^2 = [\mathbf{x}_i - \mathbf{x}_a]^T \mathbf{S}_a^{-1} [\mathbf{x}_i - \mathbf{x}_a] + [\mathbf{y} - \mathbf{F}(\mathbf{x}_i)]^T \mathbf{S}_e^{-1} [\mathbf{y} - \mathbf{F}(\mathbf{x}_i)] \quad (4.2)$$

In Equation 2, \mathbf{x}_i is the statevector, \mathbf{x}_a is the *a priori* statevector, $\mathbf{F}(\mathbf{x})$ is the forward model, \mathbf{y} is the measurement of OH and HO₂ concentrations as shown by the blue lines in Figure 4.1, \mathbf{S}_a is the *a priori* covariance matrix, and \mathbf{S}_e is the measurement error covariance matrix. In this study, \mathbf{x}_a is defined as the recommended values in the JPL 2011 evaluation. We assume the measurement error to be the sum of the systematic error σ_{sys} and random error σ_{rand} as $\sqrt{\sigma_{\text{sys}}^2 + \sigma_{\text{rand}}^2}$. Random errors are calculated from the monthly OH and HO₂ data retrieval error. We set the systematic error of OH to be 5% and HO₂ to be 20%, according to the MLS product description [Livesey *et al.*, 2015]. OH and HO₂ profiles and their assumed uncertainties are shown in Figure 4.1. The cost function is evaluated in the altitude range where we have OH or HO₂ observations, i.e., 28 – 84 km for OH and 40 – 84 km for HO₂.

The cost function is expressed as the sum of two terms. The first one represents the contribution from the adjustments we made to the model parameters $\mathbf{x}_i - \mathbf{x}_a$, such as chemical kinetic rate coefficients. The second one, $\mathbf{y} - \mathbf{F}(\mathbf{x}_i)$, represents the difference in OH and HO₂ profiles between our model simulation and MLS measurements. The iteration process in this algorithm is:

$$\mathbf{x}_{i+1} = \mathbf{x}_i + [(1 + \gamma)\mathbf{S}_a^{-1} + \mathbf{K}_i^T \mathbf{S}_e^{-1} \mathbf{K}_i]^{-1} \{ \mathbf{K}_i^T \mathbf{S}_e^{-1} [\mathbf{y} - \mathbf{F}(\mathbf{x}_i)] - \mathbf{S}_a^{-1} [\mathbf{x}_i - \mathbf{x}_a] \} \quad (4.3)$$

where \mathbf{K} is the jacobian which measures the sensitivity of model output with respect to the perturbation in each parameter, and γ is a parameter determining the size of each iteration step. Jacobians of OH and HO₂ with respect to each reaction rate

constant are plotted in Figure 4.2 and Figure 4.3, respectively. There are many factors that control the sign and magnitude of the jacobians, such as the abundances of the reactants, the temperature dependence of the reaction rates, and the intensity of solar flux (for photochemical reactions). We select important reactions based on the values of their jacobians. There are two criteria here. 1. We require that the selected reactions have high sensitivities to the concentrations of OH and HO₂, therefore, their jacobians should be large in magnitude. 2. We require that the selected reactions do not suffer from the problem of degeneracy, i.e., we have enough DOF to constrain all of them.

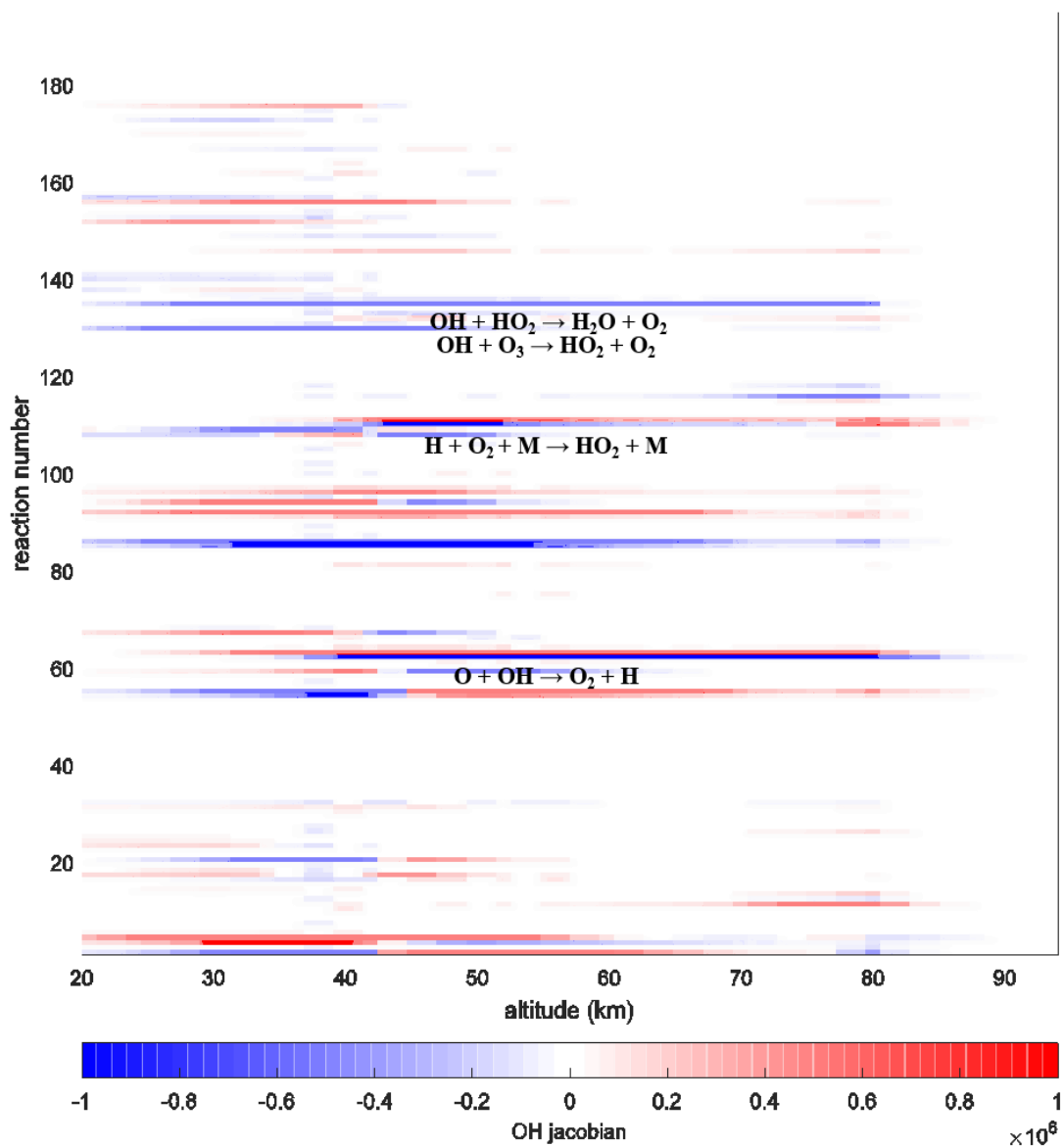


Figure 4.2. Jacobians of OH with respect to all the reaction rate constants listed in the supplementary material. Jacobian at a particular altitude is defined as the change of OH concentration (cm^{-3}) per 100% change of reaction rate constant. Important reactions are labeled in the figure. Reactions corresponding to reaction numbers are listed in the supplementary material.

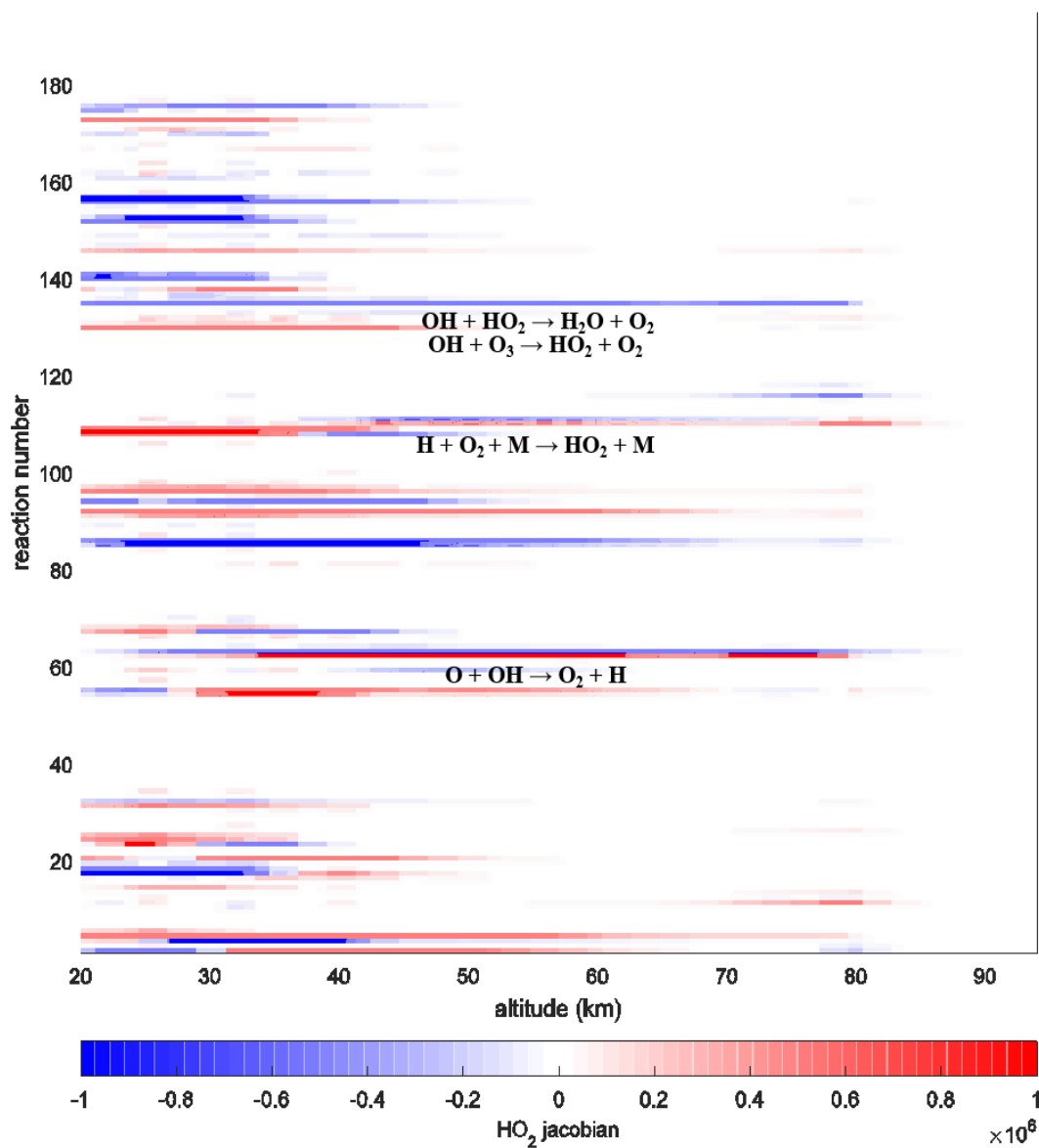
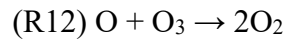
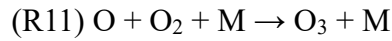


Figure 4.3. Same as Figure 4.2, jacobians of HO_2 with respect to all the reaction rate constants listed in the supplementary material. Important reactions are labeled in the figure.

A key question in the optimal estimation approach is to avoid multiple solutions. The information from the MLS measurements is not enough to constrain all the 195 reactions in this model. If too many reaction rates are adjusted, some of them may

cause degeneracy, i.e. they have very similar jacobians and therefore cannot be distinguished by the information from OH and HO₂ profiles. In this situation, we can still get a mathematically good fit of the OH and HO₂ profiles between MLS measurements and the KINETICS model simulation. However, the adjustments made to the kinetic rate coefficients are not unique, and do not have any physical meanings. For example, the following two reactions have almost symmetrically opposite effects on both OH and HO₂.

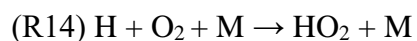


Our purpose is to exclude such similar or symmetrically opposite reactions into the optimal estimation algorithm. Otherwise they would be confounding and cause multiple solution problems. To select a list of reactions for the optimal estimation, we can calculate the DOF using 2005 June monthly mean MLS measurements (Figure 4.1), as shown in Equation 4 [Rodgers, 2000].

$$DOF = \sum_i \lambda_i^2 / (1 + \lambda_i^2) \quad (4.4)$$

where $\{\lambda_i\}$ are the singular values of the normalized Jacobian $\mathbf{S}_e^{-\frac{1}{2}} \mathbf{K} \mathbf{S}_a^{-\frac{1}{2}}$. This quantity measures how many independent pieces of information we can obtain from the measurements, i.e. how many model parameters can we estimate independently from the MLS OH and HO₂ profiles. To constrain n parameters, we require a DOF larger than $n-1$. Mathematically, the DOF depends on the uncertainties of measurements and the correlations of state variable jacobians. Using all the 195 reactions, we get a DOF equal to 6.84. Apparently, it means we do not have enough information to

constrain all them. Based on the DOF analysis, we selected 4 key reactions: (R7), (R10), and the following two reactions:



These reactions are consistent with the ones suggested by *Canty et al.* [2006] and *Siskind et al.* [2013]. OH and HO₂ jacobians with respect to these reactions are plotted as a function of altitude in Figure 4.4. These 4 reactions are independent and determine the OH and HO₂ abundances at different altitudes. Their reaction rate constant uncertainties are 20%, 30%, 15%, and 15%, respectively, according to the JPL 2011 evaluations. The uncertainty values are used as diagonal components in \mathbf{S}_a

Another important model parameter that has not been considered in previous works is the O₂ absorption cross section at Lyman- α wavelength. Figure 4.5a shows the O₂ absorption cross section as a function of wavelength. An obvious feature is the particularly small value at Lyman- α [*Liang et al.*, 2007], which is very difficult to be measured accurately in the laboratory and may thus be subject to large uncertainty.

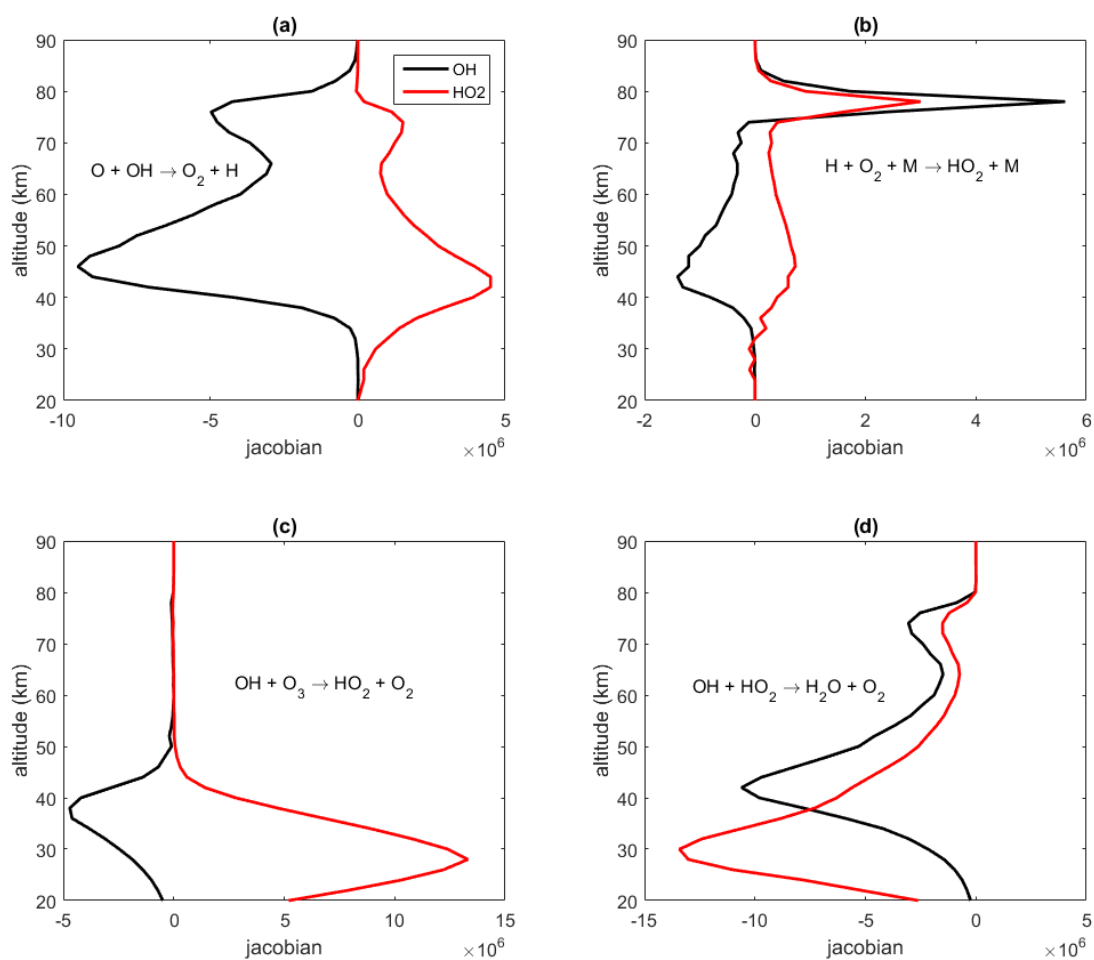


Figure 4.4. Jacobians of OH (black) and HO₂ (red) with respect to all the reaction rate constants in the optimal estimation.

The overhead sum atmospheric optical depth at Lyman- α reaches unit above 80 km due to O₂ absorption. The weaker the O₂ absorption at Lyman- α , the deeper the solar Lyman- α can penetrate into the mesosphere, and the stronger response of the H₂O photodissociation (R1) to the 11-year solar variability. Hence, the jacobians shown in Figure 4.5b reveal that adjusting the O₂ absorption cross section at Lyman-

α has a large impact on OH and HO₂ profiles. We include the O₂ cross section at Lyman- α as another state variable in our optimal estimation and give it an uncertainty of 30%. This uncertainty includes the effect of coarse spectral resolution used in the KINETKICS photochemical model. The effective cross section also decreases as atmospheric optical depth increases, since the highest absorption cross section is stronger absorbed.

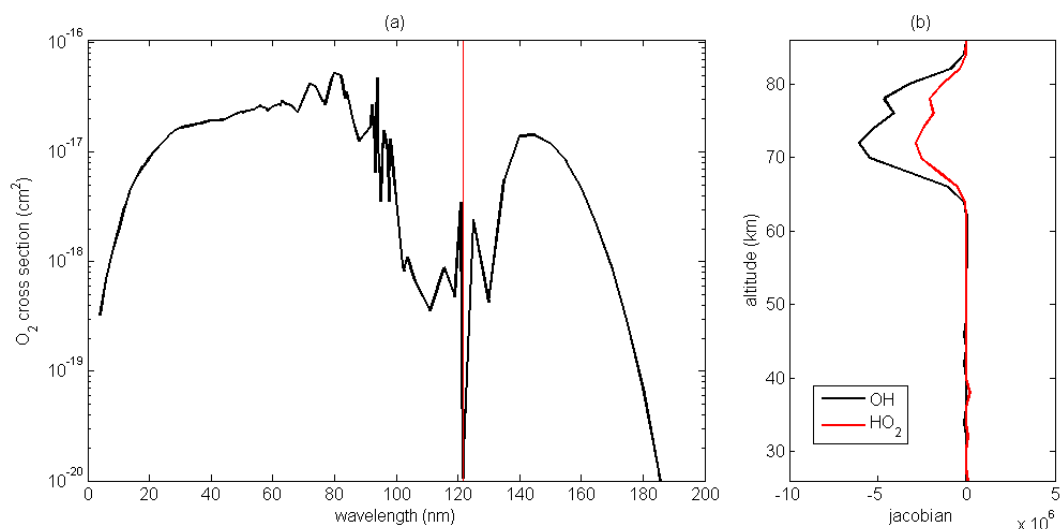


Figure 4.5. (a) O₂ cross section as a function of wavelength, Lyman- α (121.6 nm) wavelength is marked with a vertical red line. (b) Jacobian of OH (black) and HO₂ (red) with respect to the O₂ cross section at Lyman- α .

These 5 parameters have a DOF equal to 4.38. We find that including any other single reaction into the optimal estimation cannot increase the DOF by 1.0.

Table 4.1. Model parameter adjustments

reaction	uncertainty	perturbation
$\text{O} + \text{OH} \rightarrow \text{O}_2 + \text{H}$	15%	-0.3%
$\text{H} + \text{O}_2 + \text{M} \rightarrow \text{HO}_2 + \text{M}$	30%	+137.6%
$\text{OH} + \text{O}_3 \rightarrow \text{HO}_2 + \text{O}_2$	15%	-9.9%
$\text{OH} + \text{HO}_2 \rightarrow \text{H}_2\text{O} + \text{O}_2$	15%	-22.0%
O ₂ cross section	30%	-60.5%

The chemical reaction rate uncertainties are the same for the total column. The same perturbations are made at each level. [*Sander et al.*, 2011]

4.3 Results

As shown in Figure 4.1, OH and HO₂ profiles generated using standard JPL 2011 chemical kinetics show a large deficit in the mesosphere. This is consistent with *Millan et al.* [2015]. We run the optimal estimation algorithm until convergence. The *posteriori* state variables listed in Table 4.1 are the adjusted model parameters which can improve the fit between model and observation. OH and HO₂ profiles generated using our adjusted model parameters are shown as the red curves in Figure 4.1. The model results after the optimal estimation exhibit much better fit to the observation. The goodness of fit is quantified by the reduced chi-square (χ_r^2):

$$\chi_r^2 = \frac{1}{N - k - 1} \sum_i \frac{(M_i - O_i)^2}{\sigma_i^2} \quad (4.5)$$

where N is the number of data points in the observation, i.e. the sum of OH profile level and HO₂ profile level, k = 5 is the number of parameters in the optimal

estimation (equal to zero for standard chemistry before we perform the optimal estimation), $M_i - O_i$ is the difference between each observation and model-simulated data point, and σ_i is the measurement uncertainty. After the optimal estimation, the value of χ_r^2 decreases from 10.01 to 2.92, showing a significant improvement in the goodness of fit. Our model is able to simulate the overall shapes of OH and HO₂ profiles. However, χ_r^2 is still larger than 1.0 in this study, probably due to the oscillatory behavior of the OH and HO₂ profiles which is a retrieval artifact [Canty *et al.*, 2006; Pickett, 2006]

In Table 4.1, the reaction $\text{H} + \text{O}_2 + \text{M} \rightarrow \text{HO}_2 + \text{M}$ requires a 137.6% increase in its reaction rate, while the measurement uncertainty recommended by JPL 2011 evaluation is only 30%. This is much larger than the perturbations made to other model parameters. There are two possible explanations. The first one is that this reaction is primarily contributing to the production of OH and HO₂ in the mesosphere (Figure 4.4b). At this altitude, pressure and temperature are extremely low. At 78 km where the jacobian of this reaction peaks, atmospheric pressure is only 0.022 hPa. Most of the measurements of this reaction are done at much higher pressure and temperature [Sander *et al.*, 2011; and references therein] and may not be accurate at such low pressure level. The characteristic times of odd hydrogen and odd oxygen increase with altitude. Reactions at high altitude may not reach steady state, but instead be in a flowing equilibrium.

Another possible explanation is the role of radiative association reaction [Vuitton *et al.*, 2012]. In the mesosphere, the pressure is low, therefore the limiting factor of

the three body reaction is the total concentration of M. At this level, the radiative association reaction ($A + B \rightarrow AB + h\nu$) may have a similar or even higher order of magnitude reaction rate than the three-body reaction ($A + B + M \rightarrow AB + M$). As a estimation, we can calculate the reaction rate of $H + O_2 + M \rightarrow HO_2 + M$ at 78 km altitude using the low pressure limit:

$$k = k_0^{300} \left(\frac{T}{300} \right)^{-n} [M] \quad (4.6)$$

In the JPL 2011 evaluation, $k_0^{300} = 4.4 \times 10^{-32} \text{ s}^{-1} \text{ cm}^6$, $n = 1.3$. T and [M] can be read from the model output as $T = 191.6\text{K}$, $[M] = 6.32 \times 10^{14} \text{ cm}^{-3}$. To compensate for the 137.6% increase in the three body reaction rate for $H + O_2 + M \rightarrow HO_2 + M$, a radiative association reaction rate for $H + O_2 \rightarrow HO_2 + h\nu$ is needed as $6.82 \times 10^{-17} \text{ s}^{-1} \text{ cm}^3$. While the radiative association reaction rates have never been measured, *Vuitton et al.* [2012] calculated several radical-molecule reaction rates theoretically using transition state theory. Our estimated reaction rate for $H + O_2 \rightarrow HO_2 + h\nu$ is consistent with their results. According to *Vuitton et al.* [2012], the contribution of the photo association reaction in a two-heavy-atom radical-radical reaction rate coefficient is in the order of $1.0 \times 10^{-17} \text{ s}^{-1} \text{ cm}^3$. As a test, this reaction is added to our 1-D KINETIC model with a nominal reaction rate of $1.0 \times 10^{-17} \text{ s}^{-1} \text{ cm}^3$. The jacobians of OH and HO₂ with respect to this new reaction exhibit the same sharp peaks in the mesosphere, as the jacobians with respect to the three body reaction $H + O_2 + M \rightarrow HO_2 + M$ (Figure 4.6). The values of its jacobians also confirm our estimation of the required radiative association reaction rate.

We have used the 2011 JPL reaction rate coefficient estimations and take into account both the stratospheric and mesospheric peaks in the OH and HO₂ profiles. Therefore, our results are slightly different from previous studies [e.g. *Canty et al*, 2006]. For example, the JPL 2011 evaluation for the reaction rate of $O + OH \rightarrow O_2 + H$ is 16% higher than that in the 2006 or 2002 version, which results in a better match between the model and observation in the stratospheric HO_x profiles. In addition to the reactions listed in Table 4.1, we also tried other combinations of reactions, including some NO_x reactions. Their fittings are all worse than the result we have shown above.

4. 4 Discussion and Conclusion

In this study, we have proposed a systematic approach to estimate model parameters, including chemical reaction rate coefficients and molecular cross sections from high-quality MLS satellite observations. The optimal estimation output can be used to quantify model parameter uncertainties and provide guidance to laboratory measurements for some key reactions. Such sensitivity studies require multiple runs to estimate the sensitivity of model output with respect to each parameter. Therefore, we employed a fast 1-D photochemical model with enough computation speed (~ one hour for forward model run). Since HO_x chemistry in the mesosphere and stratosphere is simple and mainly controlled by several key reactions, the simplification in the transport in our model should not affect the results. In this model, all transports including vertical winds and gravity wave mixing [*Grygalashvyly et al.*, 2011] are parameterized using eddy diffusion. The most significant impact on the concentrations of HO_x species from this simplified

scheme is the transport of H₂O. As a test, we tried to perturb the eddy diffusivities at all altitudes to see their effects on OH and HO₂. The largest effect happens at the tropopause around 12 km, where H₂O is transported into the stratosphere and mesosphere. However, the jacobian of eddy diffusivity is in the order of 10⁵, much smaller than the jacobians of important reaction rate coefficients.

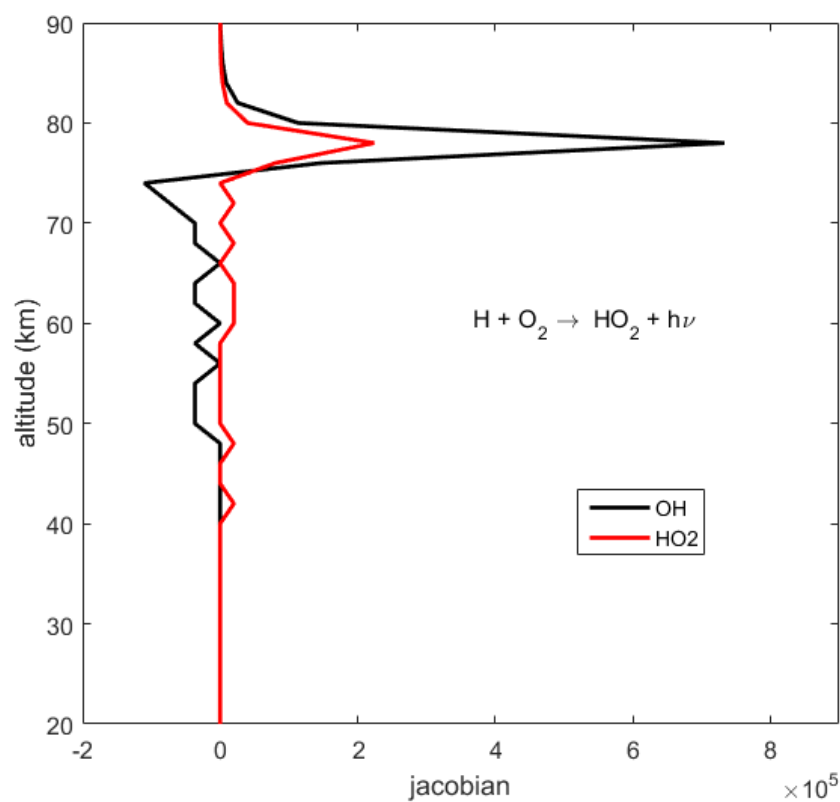


Figure 4.6. Jacobians of OH (black) and HO₂ (red) with respect to the radiative association reaction $\text{H} + \text{O}_2 \rightarrow \text{HO}_2 + h\nu$. We put this new reaction into KINETICS with a nominal reaction rate of $1.0 \times 10^{-17} \text{ s}^{-1} \text{ cm}^3$.

In previous model studies of OH, various observational constraints have been applied to reservoir species H₂O and O₃, as well as minor species such as N₂O, NO_y,

CH₄, and Cl_y [Conway *et al.*, 2000; Canty *et al.*, 2006; Pickett *et al.*, 2008]. In our work, the model is time dependent, therefore we do not apply any constraints to those species. Instead, we question whether the observed OH can be simulated by an unconstrained photochemical model. As a test of our model results, we compare the model output of H₂O and O₃ profiles with MLS measurements in Figure 4.7. Our model generally agrees with observation. The impact of HO_x species on O₃ and H₂O are relatively small, since they have much larger abundances. In the mesosphere, by using the adjusted parameters in the model, higher OH and HO₂ concentrations give rise to the O₃ loss rate. Therefore, the O₃ concentration is lower than that using standard chemistry. The results are consistent with Allen *et al.* [1981] and Canty *et al.* [2006].

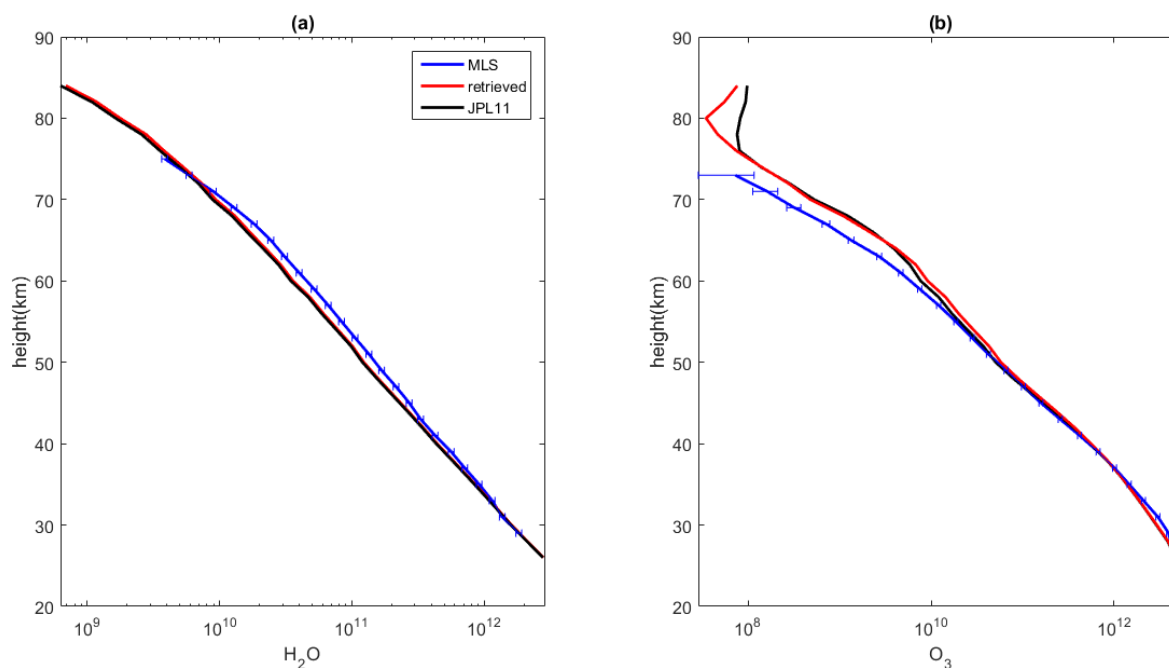


Figure 4.7. Same as Figure 4.1. Comparison between MLS measurements (blue) and Caltech-JPL KINETICS model simulations (black and red). (a) H₂O concentration (cm⁻³). (b) O₃ concentration (cm⁻³).

³). We assume the systematic error to be 5%. Concentrations are displayed in *logarithm* scale to show the differences more clearly. In a linear scale figure, the difference between model and observation is almost negligible.

Among all the state variables listed in Table 4.1, the reaction rate of $\text{H} + \text{O}_2 + \text{M} \rightarrow \text{HO}_2 + \text{M}$ and O_2 cross section require the largest adjustments. In the JPL 2011 evaluation, this reaction has the largest measurement uncertainty up to 30%, while most of the uncertainties for other reaction rates are 5% or 15%. *Siskind et al.* [2013] also shows the same result. For the O_2 cross section, in addition to the measurement error, molecular cross sections in the model could be misrepresented due to the low spectral resolution. The spectral resolution in our photochemical model varies between 20 ~ 50 Å. Cross section around Lyman- α wavelength is better resolved, but still not enough to accurately represent the dramatic change up to several orders of magnitude (Figure 4.5a). To fully resolve its shape, a typical spectral resolution of less than 1 Å is required [Ogawa, 1968]. However, this would be too expensive in terms of computational cost. The same problem also exists in a more advanced 3-D model [eg. *Garcia et al.*, 2014].

In view of the large increase in rate constant for the $\text{H} + \text{O}_2 + \text{M}$ implied by the model retrieval simulations, we have reexamined the kinetics data base for this reaction. The conclusion here is similar to that presented in *Siskind et al.* [2013]. The NASA Panel considered 11 laboratory studies of this reaction which used several different techniques over a wide range of pressures and temperatures. A large majority of these studies focused on the temperature range relevant to

combustion conditions, $298 < T < 1500$ K. Only two studies presented data relevant to the middle atmosphere. Both *Kurylo* [1972] and *Wong and Davis* [1974] used the flash photolysis-atomic resonance fluorescence technique to measure termolecular rate coefficients below room temperature using several different bath gases. For $M = N_2$ at 220 K, *Kurylo* [1972] obtained $8.35 \times 10^{-32} \text{ cm}^6 \text{ molecule}^{-2} \text{ s}^{-1}$ while *Wong and Davis* [1974] obtained $(8.6 \pm 1.6) \times 10^{-32} \text{ cm}^6 \text{ molecule}^{-2} \text{ s}^{-1}$. The rate coefficient recommended by the NASA Panel for $M = N_2$ at 220 K is considerably smaller: $6.6 \times 10^{-32} \text{ cm}^6 \text{ molecule}^{-2} \text{ s}^{-1}$. At 298 K, where there are several additional studies, the average of the k_{298} rate coefficients is also about 25-30% larger than the NASA recommendation. It should be noted that the NASA Panel accepted the recommendation contained in a theoretical paper by *Sellevåg et al.* [2008] which was aimed at obtaining a suitable fit between two-dimensional master equation calculations and the high-temperature kinetics data base for the purposes of combustion studies. Inspection of Figure 4(b) in *Sellevåg et al.* [2008] which compares their master equation results with the lab data near room temperature for $M = N_2$ clearly shows that the theoretical results fall below all the experimental data in the termolecular pressure regime. It is clear, therefore, that the *Sellevåg et al.* [2008], and implicitly the NASA recommendation, is unsuitable for the pressure and temperature range of interest for the altitude regime considered in the present study. Although the laboratory data are very sparse in this regime, a value for the $H + O_2 + N_2$ termolecular rate coefficient that is 25 ~ 30% larger than the NASA recommendation is the best choice.

Another mechanism that might enhance the effective rate of $\text{H} + \text{O}_2 \rightarrow \text{HO}_2$ under upper stratospheric conditions is radiative association. The reaction enthalpy, ΔH (298 K), is $-49.2 \text{ kcal mole}^{-1}$, which is much larger than the energy required to populate the low-lying \tilde{A} electronic state of HO_2 at about $17,200 \text{ cm}^{-1}$ provided that the required electronic curve-crossing is sufficiently rapid. This would also require a favorable fluorescence lifetime for the $\tilde{A} \ ^2A' \rightarrow \tilde{X} \ ^2A''$ transition, which is reasonably strong in absorption.

The method proposed in this study is not limited to studying HO_x chemistry. We choose to use the stratospheric and mesospheric HO_x mean profiles because they are very well measured by MLS and are mainly controlled by simple chemistry. The same method could be applied to solve other model-observation discrepancy problems. OH and HO_2 are important catalytic species for O_3 chemistry. The updated model parameters in this study can also potentially be used to model the O_3 mean profile and its responses to short- and long-term solar variabilities.

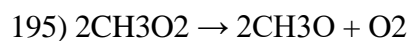
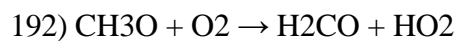
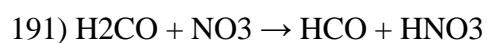
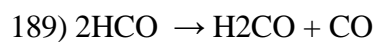
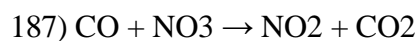
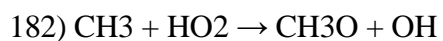
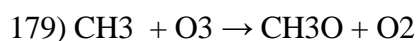
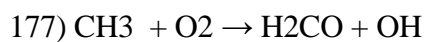
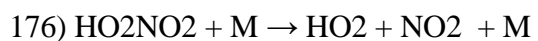
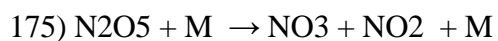
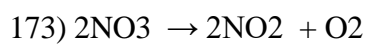
Supplementary material

- 1) $O_2 \rightarrow 2O$
- 2) $O_2 \rightarrow O + O(1D)$
- 3) $O_3 \rightarrow O_2 + O$
- 4) $O_3 \rightarrow O_2(1D) + O(1D)$
- 5) $O_3 \rightarrow O_2 + O(1D)$
- 6) $O_3 \rightarrow O_2(1D) + O$
- 7) $O_3 \rightarrow 3O$
- 8) $H_2 \rightarrow 2H$
- 9) $OH \rightarrow O + H$
- 10) $HO_2 \rightarrow OH + O$
- 11) $H_2O \rightarrow H + OH$
- 12) $H_2O \rightarrow H_2 + O(1D)$
- 13) $H_2O \rightarrow 2H + O$
- 14) $H_2O_2 \rightarrow 2OH$
- 15) $N_2 \rightarrow 2N$
- 16) $NO \rightarrow N + O$
- 17) $NO_2 \rightarrow NO + O$
- 18) $NO_3 \rightarrow NO_2 + O$
- 19) $NO_3 \rightarrow NO + O_2$
- 20) $N_2O \rightarrow N_2 + O(1D)$
- 21) $N_2O_5 \rightarrow NO_2 + NO_3$
- 22) $N_2O_5 \rightarrow NO + NO_3 + O$
- 23) $HNO_3 \rightarrow NO_2 + OH$
- 24) $HO_2NO_2 \rightarrow HO_2 + NO_2$
- 25) $HO_2NO_2 \rightarrow OH + NO_3$
- 26) $CH_4 \rightarrow CH_3 + H$
- 27) $CO_2 \rightarrow CO + O$
- 28) $CO_2 \rightarrow CO + O(1D)$
- 29) $HCO \rightarrow H + CO$
- 30) $H_2CO \rightarrow 2H + CO$
- 31) $H_2CO \rightarrow HCO + H$
- 32) $H_2CO \rightarrow H_2 + CO$
- 33) $CH_3O_2 \rightarrow CH_3 + O_2$
- 34) $CH_3OOH \rightarrow CH_3O + OH$
- 35) $H_2O \rightarrow M$
- 36) $CH_4 \rightarrow M$
- 37) $CO \rightarrow M$
- 38) $CO_2 \rightarrow M$
- 39) $H_2CO \rightarrow M$
- 40) $O_2 \rightarrow O_2$

- 41) $O_3 \rightarrow O_3$
- 42) $H_2O \rightarrow H_2O$
- 43) $N_2 \rightarrow N_2$
- 44) $NO_2 \rightarrow NO_2$
- 45) $NO_3 \rightarrow NO_3$
- 46) $N_2O_5 \rightarrow N_2O_5$
- 47) $CH_4 \rightarrow CH_4$
- 48) $CO_2 \rightarrow CO_2$
- 49) $H_2CO \rightarrow H_2CO$
- 50) $M \rightarrow RAYEARTH$
- 51) $M \rightarrow RAYCO_2$
- 52) $2O + M \rightarrow O_2 + M$
- 53) $2O + O_2 \rightarrow O_3 + O$
- 54) $O + 2O_2 \rightarrow O_3 + O_2$
- 55) $O + O_2 + N_2 \rightarrow O_3 + N_2$
- 56) $O + O_2 + CO \rightarrow O_3 + CO$
- 57) $O + O_2 + CO_2 \rightarrow O_3 + CO_2$
- 58) $O + O_2 + M \rightarrow O_3 + M$
- 59) $O + O_3 \rightarrow 2O_2$
- 60) $O + H + M \rightarrow OH + M$
- 61) $O + H_2 \rightarrow OH + H$
- 62) $O + OH \rightarrow O_2 + H$
- 63) $O + HO_2 \rightarrow OH + O_2$
- 64) $O + HO_2 \rightarrow OH + O_2(1D)$
- 65) $O + H_2O_2 \rightarrow OH + HO_2$
- 66) $O + NO + M \rightarrow NO_2 + M$
- 67) $O + NO_2 \rightarrow NO + O_2$
- 68) $O + NO_2 + M \rightarrow NO_3 + M$
- 69) $O + NO_3 \rightarrow O_2 + NO_2$
- 70) $O + N_2O_5 \rightarrow 2NO_2 + O_2$
- 71) $O + HNO_3 \rightarrow OH + NO_3$
- 72) $O + HO_2NO_2 \rightarrow OH + NO_2 + O_2$
- 73) $O + CH_3 \rightarrow H_2CO + H$
- 74) $O + CH_3 \rightarrow CO + H_2 + H$
- 75) $O + CH_4 \rightarrow CH_3 + OH$
- 76) $O + CO + M \rightarrow CO_2 + M$
- 77) $O + 2CO \rightarrow CO_2 + CO$
- 78) $2O + CO \rightarrow CO_2 + O$
- 79) $O + HCO \rightarrow H + CO_2$
- 80) $O + HCO \rightarrow OH + CO$
- 81) $O + H_2CO \rightarrow OH + HCO$
- 82) $O + CH_3O \rightarrow H_2CO + OH$
- 83) $O + CH_3O \rightarrow CH_3 + O_2$
- 84) $O + CH_3O_2 \rightarrow H_2CO + HO_2$

- 85) $O(1D) + O_2 \rightarrow O + O_2$
- 86) $O(1D) + N_2 \rightarrow O + N_2$
- 87) $O(1D) + CO_2 \rightarrow O + CO_2$
- 88) $O(1D) + U \rightarrow O$
- 89) $O(1D) + O_3 \rightarrow 2O_2$
- 90) $O(1D) + O_3 \rightarrow 2O + O_2$
- 91) $O(1D) + H_2 \rightarrow H + OH$
- 92) $O(1D) + H_2O \rightarrow 2OH$
- 93) $O(1D) + N_2 + M \rightarrow N_2O + M$
- 94) $O(1D) + N_2O \rightarrow 2NO$
- 95) $O(1D) + N_2O \rightarrow N_2 + O_2$
- 96) $O(1D) + CH_4 \rightarrow CH_3 + OH$
- 97) $O(1D) + CH_4 \rightarrow CH_3O + H$
- 98) $O(1D) + CH_4 \rightarrow H_2CO + H_2$
- 99) $O_2(1D) + O \rightarrow O_2 + O$
- 100) $O_2(1D) + O_2 \rightarrow 2O_2$
- 101) $O_2(1D) + H_2O \rightarrow O_2 + H_2O$
- 102) $O_2(1D) + N_2 \rightarrow O_2 + N_2$
- 103) $O_2(1D) + CO \rightarrow O_2 + CO$
- 104) $O_2(1D) + CO_2 \rightarrow O_2 + CO_2$
- 105) $O_2(1D) + U \rightarrow O_2$
- 106) $O_2(1D) + O_3 \rightarrow 2O_2 + O$
- 107) $O_2(1D) + N \rightarrow NO + O$
- 108) $O_3 + NO \rightarrow NO_2 + O_2$
- 109) $O_3 + NO_2 \rightarrow NO_3 + O_2$
- 110) $H + O_2 + M \rightarrow HO_2 + M$
- 111) $H + O_3 \rightarrow OH + O_2$
- 112) $2H + M \rightarrow H_2 + M$
- 113) $H + OH + N_2 \rightarrow H_2O + N_2$
- 114) $H + OH + CO_2 \rightarrow H_2O + CO_2$
- 115) $H + HO_2 \rightarrow 2OH$
- 116) $H + HO_2 \rightarrow H_2 + O_2$
- 117) $H + HO_2 \rightarrow H_2 + O_2(1D)$
- 118) $H + HO_2 \rightarrow H_2O + O$
- 119) $H + NO_2 \rightarrow OH + NO$
- 120) $H + NO_3 \rightarrow OH + NO_2$
- 121) $H + CH_3 + M \rightarrow CH_4 + M$
- 122) $H + CH_4 \rightarrow CH_3 + H_2$
- 123) $H + CO + M \rightarrow HCO + M$
- 124) $H + HCO \rightarrow H_2 + CO$
- 125) $H + H_2CO \rightarrow H_2 + HCO$
- 126) $H + CH_3O \rightarrow H_2CO + H_2$
- 127) $H + CH_3O \rightarrow OH + CH_3$
- 128) $H + CH_3O_2 \rightarrow CH_4 + O_2$

- 129) $\text{H} + \text{CH}_3\text{O}_2 \rightarrow \text{H}_2\text{O} + \text{H}_2\text{CO}$
- 130) $\text{OH} + \text{O}_3 \rightarrow \text{HO}_2 + \text{O}_2$
- 131) $\text{OH} + \text{O}_3 \rightarrow \text{HO}_2 + \text{O}_2(1\text{D})$
- 132) $\text{OH} + \text{H}_2 \rightarrow \text{H}_2\text{O} + \text{H}$
- 133) $2\text{OH} \rightarrow \text{H}_2\text{O} + \text{O}$
- 134) $2\text{OH} + \text{M} \rightarrow \text{H}_2\text{O}_2 + \text{M}$
- 135) $\text{OH} + \text{HO}_2 \rightarrow \text{H}_2\text{O} + \text{O}_2$
- 136) $\text{OH} + \text{HO}_2 \rightarrow \text{H}_2\text{O} + \text{O}_2(1\text{D})$
- 137) $\text{OH} + \text{H}_2\text{O}_2 \rightarrow \text{H}_2\text{O} + \text{HO}_2$
- 138) $\text{OH} + \text{NO}_2 + \text{M} \rightarrow \text{HNO}_3 + \text{M}$
- 139) $\text{OH} + \text{NO}_3 \rightarrow \text{HO}_2 + \text{NO}_2$
- 140) $\text{OH} + \text{HNO}_3 \rightarrow \text{NO}_3 + \text{H}_2\text{O}$
- 141) $\text{OH} + \text{HO}_2\text{NO}_2 \rightarrow \text{H}_2\text{O} + \text{NO}_2 + \text{O}_2$
- 142) $\text{OH} + \text{CH}_3 \rightarrow \text{H}_2\text{CO} + \text{H}_2$
- 143) $\text{OH} + \text{CH}_3 \rightarrow \text{CH}_3\text{O} + \text{H}$
- 144) $\text{OH} + \text{CH}_3 \rightarrow \text{CO} + 2\text{H}_2$
- 145) $\text{OH} + \text{CH}_4 \rightarrow \text{CH}_3 + \text{H}_2\text{O}$
- 146) $\text{OH} + \text{CO} \rightarrow \text{CO}_2 + \text{H}$
- 147) $\text{OH} + \text{HCO} \rightarrow \text{H}_2\text{O} + \text{CO}$
- 148) $\text{OH} + \text{H}_2\text{CO} \rightarrow \text{HCO} + \text{H}_2\text{O}$
- 149) $\text{OH} + \text{CH}_3\text{O} \rightarrow \text{H}_2\text{O} + \text{H}_2\text{CO}$
- 150) $\text{OH} + \text{CH}_3\text{OOH} \rightarrow \text{CH}_3\text{O}_2 + \text{H}_2\text{O}$
- 151) $\text{HO}_2 + \text{O}_3 \rightarrow \text{OH} + 2\text{O}_2$
- 152) $2\text{HO}_2 \rightarrow \text{H}_2\text{O}_2 + \text{O}_2$
- 153) $2\text{HO}_2 \rightarrow \text{H}_2\text{O}_2 + \text{O}_2(1\text{D})$
- 154) $2\text{HO}_2 + \text{M} \rightarrow \text{H}_2\text{O}_2 + \text{O}_2 + \text{M}$
- 155) $\text{HO}_2 + \text{NO} \rightarrow \text{NO}_2 + \text{OH}$
- 156) $\text{HO}_2 + \text{NO}_2 + \text{M} \rightarrow \text{HO}_2\text{NO}_2 + \text{M}$
- 157) $\text{HO}_2 + \text{NO}_3 \rightarrow \text{HNO}_3 + \text{O}_2$
- 158) $\text{HO}_2 + \text{HCO} \rightarrow \text{H}_2\text{CO} + \text{O}_2$
- 159) $\text{HO}_2 + \text{CH}_3\text{O} \rightarrow \text{H}_2\text{CO} + \text{H}_2\text{O}_2$
- 160) $\text{HO}_2 + \text{CH}_3\text{O}_2 \rightarrow \text{CH}_3\text{OOH} + \text{O}_2$
- 161) $\text{N} + \text{O}_2 \rightarrow \text{NO} + \text{O}$
- 162) $\text{N} + \text{O}_3 \rightarrow \text{NO} + \text{O}_2$
- 163) $\text{N} + \text{OH} \rightarrow \text{NO} + \text{H}$
- 164) $\text{N} + \text{HO}_2 \rightarrow \text{NO} + \text{OH}$
- 165) $2\text{N} + \text{M} \rightarrow \text{N}_2 + \text{M}$
- 166) $\text{N} + \text{NO} \rightarrow \text{N}_2 + \text{O}$
- 167) $\text{N} + \text{NO}_2 \rightarrow \text{N}_2\text{O} + \text{O}$
- 168) $\text{N}_2 + \text{U} \rightarrow 2\text{N}$
- 169) $\text{NO} + \text{NO}_3 \rightarrow 2\text{NO}_2$
- 170) $\text{NO} + \text{CH}_3\text{O}_2 \rightarrow \text{CH}_3\text{O} + \text{NO}_2$
- 171) $\text{NO}_3 + \text{NO}_2 \rightarrow \text{NO} + \text{NO}_2 + \text{O}_2$
- 172) $\text{NO}_3 + \text{NO}_2 + \text{M} \rightarrow \text{N}_2\text{O}_5 + \text{M}$



Bibliography:

Allen, M., Y. L. Yung, and J. W. Waters (1981), Vertical Transport and Photochemistry in the Terrestrial Mesosphere and Lower Thermosphere (50-120 Km), *J Geophys Res-Space*, 86(Na5), 3617-3627, doi:Doi 10.1029/Ja086ia05p03617.

Brasseur, G. P. and S. Solomon. 2005. *Aeronomy of the Middle Atmosphere*. Springer.

Cageao, R. P., J. F. Blavier, J. P. McGuire, Y. B. Jiang, V. Nemtchinov, F. P. Mills, and S. P. Sander (2001), High-resolution Fourier-transform ultraviolet-visible spectrometer for the measurement of atmospheric trace species: application to OH, *Appl Optics*, 40(12), 2024-2030, doi:Doi 10.1364/Ao.40.002024.

Canty, T., and K. Minschwaner (2002), Seasonal and solar cycle variability of OH in the middle atmosphere, *J Geophys Res-Atmos*, 107(D24), doi:Artn 473710.1029/2002jd002278.

Canty, T., H. M. Pickett, R. J. Salawitch, K. W. Jucks, W. A. Traub, and J. W. Waters (2006), Stratospheric and mesospheric HOx: results from aura MLS and FIRS-2, *Geophys Res Lett*, 33(12), doi:Artn L1280210.1029/2006gl025964.

Conway, R. R., M. E. Summers, M. H. Stevens, J. G. Cardon, P. Preusse, and D. Offermann (2000), Satellite observations of upper stratospheric and mesospheric OH: The HOx dilemma, *Geophys Res Lett*, 27(17), 2613-2616,

doi:Doi 10.1029/2000gl011698.

- Englert, C. R., M. H. Stevens, D. E. Siskind, J. M. Harlander, F. L. Roesler, H. M. Pickett, C. von Savigny, and A. J. Kochenash (2008), First results from the Spatial Heterodyne Imager for Mesospheric Radicals (SHIMMER): Diurnal variation of mesospheric hydroxyl, *Geophys Res Lett*, 35(19), doi:Artn L1981310.1029/2008gl03542
- Garcia, R. R., M. Lopez-Puertas, B. Funke, D. R. Marsh, D. E. Kinnison, A. K. Smith & F. Gonzalez-Galindo (2014) On the distribution of CO₂ and CO in the mesosphere and lower thermosphere. *Journal of Geophysical Research-Atmospheres*, 119, 5700-5718.
- Grygalashvily, M., E. Becker & G. R. Sonnemann (2011) Wave mixing effects on minor chemical constituents in the MLT region: Results from a global CTM driven by high-resolution dynamics. *Journal of Geophysical Research-Atmospheres*, 116. D18302.
- Jucks, K. W., D. G. Johnson, K. V. Chance, W. A. Traub, J. J. Margitan, G. B. Osterman, R. J. Salawitch, and Y. Sasano (1998), Observations of OH, HO₂, H₂O, and O-3 in the upper stratosphere: implications for HOx photochemistry, *Geophys Res Lett*, 25(21), 3935-3938, doi:Doi 10.1029/1998gl900009.
- Kurylo, M. J. (1972). Absolute rate constants for the reaction H⁺ O₂⁺ M. far. HO₂⁺

M over the temperature range 203-404. deg. K. *The Journal of Physical Chemistry*, 76(24), 3518-3526.

Lean, J. (2000), Evolution of the sun's spectral irradiance since the Maunder Minimum, *Geophys Res Lett*, 27(16), 2425-2428, doi:Doi 10.1029/2000gl000043.

Lean, J., G. Rottman, J. Harder, and G. Kopp (2005), SORCE contributions to new understanding of global change and solar variability, *Sol Phys*, 230(1-2), 27-53, doi:DOI 10.1007/s11207-005-1527-2.

Lean, J. L., and M. T. Deland (2012), How Does the Sun's Spectrum Vary?, *J Climate*, 25(7), 2555-2560, doi:Doi 10.1175/Jcli-D-11-00571.1.

Li, C., X. Zhang, J. A. Kammer, M. C. Liang, R. L. Shia, and Y. L. Yung (2014), A non-monotonic eddy diffusivity profile of Titan's atmosphere revealed by Cassini observations, *Planet Space Sci*, 104, 48-58, doi:10.1016/j.pss.2013.10.009.

Li, K. F., R. P. Cageao, E. M. Karpilovsky, F. P. Mills, Y. L. Yung, J. S. Margolis, and S. P. Sander (2005), OH column abundance over Table Mountain Facility, California: AM-PM diurnal asymmetry, *Geophys Res Lett*, 32(13), doi:Artn L1381310.1029/2005gl022521.

Liang, M. C., G. A. Blake, B. R. Lewis, and Y. L. Yung (2007), Oxygen isotopic composition of carbon dioxide in the middle atmosphere, *P Natl Acad Sci*

USA, 104(1), 21-25, doi:10.1073/pnas.0610009104.

Livesey, N. J., W. G. R., Paul A. Wagner, Lucien Froidevaux, Alyn Lambert, Gloria L. Manney, Luis F. Mill'an Valle, Hugh C. Pumphrey, Michelle L. Santee, Michael J. Schwartz, Shuhui Wang, Ryan A. Fuller, Robert F. Jarnot, Brian W. Knosp, Elmain Martinez (2015), *Version 4.2x Level 2 data quality and description document*, JPL, Jet Propulsion Laboratory, Pasadena.

Millan, L., S. Wang, N. Livesey, D. Kinnison, H. Sagawa, and Y. Kasai (2015), Stratospheric and mesospheric HO₂ observations from the Aura Microwave Limb Sounder, *Atmos Chem Phys*, 15(5), 2889-2902, doi:10.5194/acp-15-2889-2015.

Nicolet, M. & W. Peetermans (1980) Atmospheric Absorption in the O₂ Schumann-Runge Band Spectral Range and Photo-Dissociation Rates in the Stratosphere and Mesosphere. *Planetary and Space Science*, 28, 85-103.

Ogawa, M. (1968) Absorption Coefficients of O₂ at Lyman-Alpha Line and Its Vicinity. *Journal of Geophysical Research*, 73,6759.

Pickett, H. M. (2006), Microwave Limb Sounder THz module on Aura, *Ieee T Geosci Remote*, 44(5), 1122-1130, doi:10.1109/Tgrs.2005.862667.

Pickett, H. M., B. J. Drouin, T. Canty, L. J. Kovalenko, R. J. Salawitch, N. J. Livesey, W. G. Read, J. W. Waters, K. W. Jucks, and W. A. Traub (2006), Validation of Aura MLS HO_x measurements with remote-sensing balloon instruments,

Geophys Res Lett, 33(1), doi:Artn L0180810.1029/2005gl024048.

Pickett, H. M., et al. (2008), Validation of Aura Microwave Limb Sounder OH and HO₂ measurements, *J Geophys Res-Atmos*, 113(D16), doi:Artn D16s3010.1029/2007jd008775.

Rodgers, C. D. (2000), *Inverse Methods for Atmospheric Sounding: Theory and Practice*, World Scientific Publishing Co. Pte. Ltd. Singapore

Rozanov, E., T. Egorova, W. Schmutz, and T. Peter (2006), Simulation of the stratospheric ozone and temperature response to the solar irradiance variability during sun rotation cycle, *J Atmos Sol-Terr Phy*, 68(18), 2203-2213, doi:DOI 10.1016/j.jastp.2006.09.004.

Sander, S. P., J. Abbatt, J. R. Barker, J. B. Burkholder, R. R. Friedl, D. M. Golden, R. E. Huie, C. E. Kolb, M. J. Kurylo, G. K. Moortgat, V. L. Orkin and P. H. Wine (2011), *Chemical Kinetics and Photochemical Data for Use in Atmospheric Studies, Evaluation No. 17*, JPL, Jet Propulsion Laboratory, Pasadena.

Sellevåg, S. R., Y. Georgievskii, and J. A. Miller (2008), The temperature and pressure dependence of the reactions $\text{H}+\text{O}_2(+\text{M})\rightarrow\text{HO}_2(+\text{M})$ and $\text{H}+\text{OH}(+\text{M})\rightarrow\text{H}_2\text{O}(+\text{M})$, *J Phys Chem A*, 112(23), 5085-5095, doi:10.1021/jp711800z.

Shapiro, A. V., E. Rozanov, A. I. Shapiro, S. Wang, T. Egorova, W. Schmutz, and T.

- Peter (2012), Signature of the 27-day solar rotation cycle in mesospheric OH and H₂O observed by the Aura Microwave Limb Sounder, *Atmos Chem Phys*, *12*(7), 3181-3188, doi:10.5194/acp-12-3181-2012.
- Siskind, D. E., M. H. Stevens, C. R. Englert, and M. G. Mlynczak (2013), Comparison of a photochemical model with observations of mesospheric hydroxyl and ozone, *J Geophys Res-Atmos*, *118*(1), 195-207, doi:10.1029/2012JD017971.
- Summers, M. E., R. R. Conway, D. E. Siskind, M. H. Stevens, D. Offermann, M. Riese, P. Preusse, D. F. Strobel, and J. M. Russell (1997), Implications of satellite OH observations for middle atmospheric H₂O and ozone, *Science*, *277*(5334), 1967-1970, doi:DOI 10.1126/science.277.5334.1967.
- Vuitton, V., R. V. Yelle, P. Lavvas, and S. J. Klippenstein (2012), Rapid Association Reactions at Low Pressure: Impact on the Formation of Hydrocarbons on Titan, *Astrophys J*, *744*(1), doi:Artn 1110.1088/0004-637x/744/1/11.
- Wang, S., Q. Zhang, L. Millán, K. F. Li, Y. L. Yung, S. P. Sander, N. J. Livesey, and M. L. Santee (2015), First evidence of middle atmospheric HO₂ response to 27 day solar cycles from satellite observations, *Geophys Res Lett*, *42*(22).
- Wang, S. H., K-F Li, T. J. Pongetti, et al. (2013), Midlatitude atmospheric OH response to the most recent 11-year solar cycle, *P Natl Acad Sci USA*, *110*(6), 2023-2028, doi:10.1073/pnas.1117790110.

Waters, J. W., et al. (2006), The Earth Observing System Microwave Limb Sounder (EOS MLS) on the Aura satellite, *Ieee T Geosci Remote*, 44(5), 1075-1092, doi:Doi 10.1109/Tgrs.2006.873771.

Wong, W., and D. D. Davis (1974), Flash Photolysis-Resonance Fluorescence Study of Reaction of Atomic-Hydrogen with Molecular-Oxygen $H + O_2 + M \rightarrow HO_2 + M$, *Int J Chem Kinet*, 6(3), 401-416, doi:DOI 10.1002/kin.55006031

A p p e n d i x

SUBMESOSCALE TURBULENCE OVER A TOPOGRAPHIC SLOPE

#Manuscript submitted to Ocean Modelling

Submesoscale Turbulence over a Topographic Slope

Qiong Zhang¹, Andrew F. Thompson¹, Ayah Lazar¹

*California Institute of Technology, 1200E California Blvd,
Pasadena, CA, 91125*

Abstract

Oceanic motions at submesoscales are characterized by enhanced vertical velocities, as compared to mesoscale motions, due to greater contributions from ageostrophic flows. These enhanced vertical velocities can make an important contribution to turbulent fluxes near ocean boundaries. Regions of the ocean near continental slopes are also linked to significant vertical velocities caused by advection over a sloping bottom, frictional processes and diffusion. Sloping topography may also induce large-scale potential vorticity gradients by modifying the slope of interior isopycnal surfaces. Potential vorticity gradients, in turn, may feed back on mesoscale stirring and the generation of submesoscale features.

In this study, we explore the impact of sloping topography on the characteristics of submesoscale motions. We use the MITgcm to conduct high-resolution ($1 \text{ km} \times 1 \text{ km}$) simulations of a wind-driven frontal current over an idealized continental shelf and slope. We explore changes in the magnitude, skewness and spectra of surface vorticity and vertical velocity across different configurations of the topographic slope and wind-forcing orientations. These properties are strongly modulated by the topographic slope. Additionally, submesoscale motions exhibit spatial variability across the continental shelf and slope. We find that changes in submesoscale characteristics are linked to mesoscale stirring responding to differences in the interior potential vorticity distributions, which

*Qiong Zhang
Email address: qzh@caltech.edu (Qiong Zhang)

are set by frictional processes at the ocean surface and over the sloping bottom. Improved parameterizations of submesoscale motions over topography may be needed to simulate the spatial variability of these features in coarser resolution models and accurately represent vertical nutrient fluxes in coastal waters.

Keywords: submesoscale, turbulence, topography, potential vorticity

1 **1. Introduction**

2 Dynamically, the transition between mesoscale and submesoscale motions
3 is often marked by the loss of geostrophic balance. This is also accompanied
4 by the generation of larger vertical velocities through ageostrophic circulations,
5 which occurs for $Ro \sim O(1)$ (Thomas et al., 2008). Here, the Rossby number
6 Ro is the ratio of the vertical component of relative vorticity ζ to the Coriolis
7 frequency f . Previous studies have shown that submesoscale flows can influ-
8 ence vertical mixing (Klein and Lapeyre, 2009), energy transport (Klein et al.,
9 2008), biological productivity (Mahadevan and Archer, 2000; Levy et al., 2012)
10 and carbon export (Omand et al., 2015). However, parameterizations of subme-
11 soscale dynamics are only now being implemented in global general circulation
12 models (GCMs) (Fox-Kemper et al., 2008), largely based on process studies in
13 more idealized model configurations. Meanwhile, regional GCMs that directly
14 resolve submesoscale motions show a potential increase in total eddy kinetic
15 energy (EKE) by a factor of two (Siegel et al., 2001; Klein and Lapeyre, 2009)
16 as compared to simulations where these motions are not resolved. The contribu-
17 tion of submesoscales to regional EKE may also exhibit seasonal cycles (Mensa
18 et al., 2013; Sasaki et al., 2014).

19 Motions at meso- and submesoscales are intricately linked as stirring by
20 coherent mesoscale eddies are typically responsible either for frontogenesis or
21 filamentation that produce lateral gradients that become susceptible to subme-
22 soscale instabilities (Boccaletti et al., 2007; Capet et al., 2008). Thus variations
23 in the spatial and temporal scales of mesoscale motions may be reflected in the
24 intensity of submesoscale flows. Variations in the depth of the mixed layer and

25 the vertical stratification may also modulate the submesoscale characteristics.

26 Large-scale topographic slopes focus frontal currents or jets, influence the
27 extraction of potential energy via baroclinic instability and modulate the result-
28 ing equilibrated eddy kinetic energy (EKE) of ocean flows (Hart, 1975; Poulin
29 and Flierl, 2005; Thompson, 2010; Isachsen, 2011; Stewart and Thompson, 2015;
30 Stern et al., 2015). Topographic constraints on ocean variability are particularly
31 strong at the continental margins with previous studies emphasizing the impact
32 of topographic slopes on frontogenesis and jet stability (Poulin and Flierl, 2005;
33 Wang and Jordi, 2011; Spall, 2013). Figure 1 shows an estimate of Ro along
34 a transect spanning the continental shelf and slope in the western Weddell Sea
35 (Thompson and Heywood, 2008). The relative vorticity here is approximated
36 by $\zeta = v_x$, where v and x are the cross-transect velocity and along-track dis-
37 tance respectively. The cross-transect velocity is calculated using the thermal
38 wind relationship, referenced to the depth-averaged current from the glider, as
39 documented in Thompson et al. (2014). This is a good approximation because
40 $v_x \gg u_y$ in this region. The figure shows that Ro often exceeds values of 0.5 and
41 frequently reaches a magnitude of $O(1)$, suggesting that balanced geostrophic
42 motion may be insufficient to describe dynamics here and in other parts of the
43 ocean’s continental margins.

44 This observational data is also consistent with recent high-resolution numer-
45 ical studies with a similar shelf-slope configuration. Stewart and Thompson
46 (2013, 2015) find that submesoscale eddies are generated over the continental
47 shelf and shelf break, but are suppressed over the continental slope due to the
48 strong potential vorticity gradient (Isachsen, 2011). To date, much of the work
49 on submesoscale dynamics have been limited to idealized processes models or
50 observational studies in strong western boundary currents (DAsaro et al., 2011;
51 Shcherbina et al., 2013; Thomas et al., 2013) and the open ocean (Thompson
52 et al., 2016), thus the understanding of how topographic slopes influence sub-
53 mesoscale dynamics is limited. An exception is a pair of studies that used a high
54 resolution ($1/20^\circ$) numerical model to examine the generation of submesoscale
55 dynamics in the lee of the Kerguelen Plateau in the Antarctic Circumpolar

56 Current (ACC) (Rosso et al., 2014, 2015). These simulations suggested that
57 the ACC's interaction with the bathymetry enhanced the generation of subme-
58 soscale eddies, which subsequently played a key role in the vertical advection of
59 tracers. However, this regime is somewhat unique, since the topographic inter-
60 actions are transient as the flow moves past the plateau and the flow transitions
61 between different states, e.g. topographically-steered and open ocean. We focus
62 on a simpler configuration in this study.

63 One common characteristic of submesoscale turbulence is the generation of
64 ageostrophic motions that produce a significant asymmetry between cyclonic
65 and anticyclonic coherent vortices. Both theoretical predictions (Kloosterziel
66 et al., 2007; Lazar et al., 2013b) and laboratory experiments (Afanasyev and
67 Peltier, 1998; Lazar et al., 2013a) have shown that anticyclonic vortices are more
68 susceptible to inertial instability. This has been used to explain the preponder-
69 ance of cyclonic submesoscale eddies observed at the ocean surface (Munk et al.,
70 2000). Furthermore, Eldevik and Dysthe (2002) showed that ageostrophic baro-
71 clinic instability produces narrow frontal zones of strong cyclonic shear which
72 roll up into submesoscale cyclonic eddies. Both of these mechanisms could ex-
73 plain the results of Capet et al. (2008) and Klein et al. (2008) who demonstrated,
74 in numerical simulations of the California Current system and a baroclinically-
75 unstable zonal flow respectively, that submesoscale processes favor the gener-
76 ation of cyclonic vortices with Ro larger than one. These results also hold in
77 observations for open ocean regimes in which the fluid motion does not feel
78 any additional constraints due to changes in the water column depth (Buck-
79 ingham et al., 2016). Here we explore the robustness of these asymmetries in
80 topographically-controlled flows.

81 While this study largely focuses on the pattern of surface turbulence, it is
82 known (and shown below) that surface characteristics are linked to potential
83 vorticity (PV) distributions in the fluid interior. Modifications to PV are con-
84 centrated at the surface and sea floor due to surface wind forcing and bottom
85 friction respectively. Thomas (2005) showed that down-front wind forcing can
86 extract PV from the fluid at the surface. The low PV is then transmitted

87 through the boundary layer by the secondary circulation induced by the front
88 (Hoskins, 1982). Benthuisen and Thomas (2012) proposed that bottom friction,
89 responding to flow over a sloping bottom, could also inject or extract PV from
90 the fluid depending on the direction of the mean flow. Bottom Ekman trans-
91 port may induce changes in the isopycnal layer thickness and modulate PV in
92 the fluid interior (Thompson et al., 2014). Finally, on larger scales, we also
93 address the role of topography modifying the background PV, which changes
94 the turbulence patterns.

95 In this manuscript, we explore the hypothesis that a sloping bottom topog-
96 raphy has the potential to significantly modulate submesoscale characteristics
97 of a turbulent ocean flow. We simulate an idealized wind-forced channel, which
98 allows us to examine a range of surface wind-topography configurations. In §2
99 we present the model configuration and introduce five different experiments. In
100 §3, we present results from the numerical simulations, focusing on vorticity dis-
101 tributions, vertical velocity and energy spectra, which are common methods of
102 identifying submesoscale characteristics. We also discuss the relationship with
103 larger-scale PV distributions. Discussions of these results and our conclusions
104 follow in §4 and §5.

105 **2. Model description**

106 The MITgcm is employed to simulate a zonally-periodic channel on an f -
107 plane, forced by a zonally-symmetric wind stress. A schematic figure, depicting
108 the various model configurations, is shown in Figure 2. Since this study is partly
109 motivated by data collected around the continental margins of Antarctica, the
110 Coriolis parameter in the model is defined as $f = -1 \times 10^{-4} \text{ s}^{-1}$. Typically,
111 resolving submesoscale eddies requires the horizontal resolution on the order
112 of one tenth of the Rossby deformation radius (Levy et al., 2012). The model
113 domain used in this study is 640 km in the meridional direction and 320 km
114 in the zonal direction with a horizontal resolution of 1 km \times 1 km. This scale
115 is much smaller than the Rossby deformation radius, $\lambda = NH/f$, where N is

116 the buoyancy frequency ($\sim 4 \times 10^{-3} \text{ s}^{-1}$). These values produce a λ that varies
 117 between 10 km and 30 km, depending on the depth. In the vertical direction we
 118 have 60 layers evenly spaced from the surface to a maximum depth of $H = 600\text{m}$,
 119 giving a vertical resolution of 10 m. Density is a linear function of the potential
 120 temperature (θ) with a constant thermal expansion coefficient $\alpha = 1 \times 10^{-4}$
 121 ($^{\circ}\text{C}$) $^{-1}$. The initial θ ($^{\circ}\text{C}$) profile is a function of latitude and depth,

$$\theta(y, z) = T_0 \left(1 + \frac{y}{\ell_\theta} \right) \exp\left(\frac{z}{H}\right), \quad (1)$$

122 where $T_0 = 19^{\circ}\text{C}$ and $\ell_\theta = 80 \text{ km}$. We define $y = 0$ to be the meridional mid-
 123 point of the channel. The surface temperature at the southern and northern
 124 boundaries of the domain are 15°C and 23°C , respectively. We provide a small
 125 perturbation to the initial temperature profile to induce baroclinic instability.
 126 At the northern and southern boundaries, θ relaxes to the initial stratification
 127 within a sponge layer of 20 km width. The relaxation decays linearly to zero
 128 across the sponge layer with a maximum time scale of 3 days at the northern
 129 and southern boundaries.

130 At the surface, we apply a meridionally-varying Gaussian wind stress

$$\tau = \tau_0 \exp\left(-\frac{y^2}{\sigma^2}\right) \quad (2)$$

131 with the peak value $\tau_0 = 0.05 \text{ N m}^{-2}$ and a standard deviation of $\sigma = 40 \text{ km}$.
 132 The momentum input by the wind stress is balanced by a linear bottom friction
 133 with a constant bottom drag coefficient, $r = 1.1 \times 10^{-3} \text{ m s}^{-1}$. In this model,
 134 horizontal and vertical viscosities are set to be 1 and $10^{-5} \text{ m}^2 \text{ s}^{-1}$ respectively.
 135 Horizontal and vertical temperature diffusion coefficients are 10 and $10^{-5} \text{ m}^2 \text{ s}^{-1}$,
 136 respectively. To simulate vertical mixing in the ocean surface boundary layer,
 137 the K-profile parametrization (KPP) method (Large et al., 1997) is employed.

138 To study the influence of bathymetry, the simulations include a zonally-
 139 uniform topographic slope described by:

$$h(y, z) = -H \pm d \tanh\left(\frac{y}{\ell_h}\right), \quad (3)$$

140 where $H = 400 \text{ m}$, $d = 200 \text{ m}$ is the height of the slope relative to the maximum
 141 depth and $\ell_h = 40 \text{ km}$ is the meridional scale of the slope. The \pm sign indicates

142 that the continental shelf, the shallowest part of which is 200 m, may be either
143 in the north (−) or the south (+). Following Poulin and Flierl (2005), we label
144 the topographic slope as *prograde* when the shallow water is located to the
145 left of the jet direction (recall that $f < 0$); we label the topographic slope as
146 *retrograde* when the shallow water is to the right of the jet direction. Unlike
147 Poulin and Flierl (2005) the jet direction is strongly forced by the surface wind
148 stress, as opposed to responding to the propagation direction of topographic
149 Rossby waves. The wind orientation is referenced to the initial temperature
150 distribution. Down-front (DF) winds have the warmer water to the left of the
151 wind stress maximum, while up-front (UF) winds have warmer water to the
152 right of the wind stress maximum.

153 The parameter space we explore in this study is solely based on the relative
154 orientation of the surface winds and the bathymetry. Experiments completed
155 with different amplitudes of these properties showed qualitatively similar results.
156 Based on alternating these two values, and including a “control” simulation with
157 a flat bottom (DF-F1), there are five different model configurations that are pre-
158 sented in Table 1 and Figure 2. In each Experiment, the surface wind generates
159 an along-slope current that is in the same direction as the wind stress. Thus
160 while configurations DF-S and DF-N both have a westerly wind stress and east-
161 ward jet, they produce retrograde and prograde jets respectively because in the
162 former, the shallow shelf region is to the south (S experiments) while in the lat-
163 ter the shelf is located to the north (N experiments). Similarly, configurations
164 UF-S and UF-N produce prograde and retrograde jets respectively. Since the
165 model simulates f -plane dynamics, the terms north and south have no dynam-
166 ical meaning, however, the relaxation towards a colder boundary condition to
167 the south sets the orientation of the large-scale background shear. In all of the
168 simulations this shear is positive $\partial u/\partial z > 0$.

169 For each Experiment described in Table 1, the simulation is integrated for
170 a period of 1000 days. The initial velocity is zero everywhere in the domain.
171 The time required to reach a statistically-equilibrated state depends on the
172 model configurations, however all model runs are equilibrated after 500 days.

173 Equilibration is determined from considering the time series of total kinetic
 174 energy (TKE) (Figure 3). Due to the suppression of linear instability growth
 175 rates over sloping topography (Isachsen, 2011), the experiments including a
 176 topographic slope take longer to reach equilibrium than the control experiment,
 177 DF-Fl. All calculations shown below represent averages over the last 200 days.

178 3. Results

179 Figure 3 provides an overview of Experiment DF-S. Available potential en-
 180 ergy is present in all simulations due to the imposed initial temperature distribu-
 181 tion. In experiments with down-front winds, Ekman pumping also contributes
 182 additional tilting of isopycnal surfaces. Baroclinic instability acts to relax this
 183 isopycnal tilt and generates mesoscale turbulence. Figure 3b shows a snapshot
 184 of surface θ at day 900; the sharp θ gradient just north of $y = 0$ is indicative of
 185 frontogenesis with both mesoscale and submesoscale structures apparent. While
 186 mesoscale structure is largely associated with balanced, horizontal flow, Figure
 187 3c provides strong evidence for an active and energetic submesoscale flow by
 188 showing a snapshot of the vertical velocity w at a depth of 30 m. Near-surface
 189 w has a large magnitude (up to 10 *m/day*) and displays fine filaments associ-
 190 ated with ageostrophic fronts. A spatial pattern in the strength of w occurs
 191 (Figure 3c) with large absolute values of w over the deeper (northern) flank of
 192 the domain, while turbulence is suppressed over the shallow (southern) flank of
 193 the domain.

194 The enhancement of vertical velocities is consistent with a transition towards
 195 flow with $O(1)$ Rossby number. Figure 4 shows both time-averaged and snap-
 196 shots of the surface (10 m) Ro for each of the five experiments in Table 1. As
 197 in previous studies, we define local Ro as the ratio of absolute vertical vorticity
 198 and planetary vorticity:

$$Ro = \frac{\mathbf{k} \cdot \nabla \times \mathbf{u}}{f}, \quad (4)$$

199 where \mathbf{u} is the velocity and \mathbf{k} is the vertical unit vector. In the snapshots
 200 the surface Ro is frequently of $O(1)$. Comparing the different experiments,

201 we find the following features: (1) In all experiments, the domain is domi-
 202 nated by regions where Ro is positive. (2) Simulations that have a topographic
 203 slope tend to exhibit structure on smaller scales compared to the DF-FI Ex-
 204 periment (panel a). (3) Furthermore, in all experiments with topography, the
 205 meso/submesoscale turbulence acquires an asymmetric meridional (warm-to-
 206 cold or deep-to-shallow) spatial pattern. For example, in Figure 4(b,c), the
 207 down-front wind experiments, the warmer, “northern” flank is more energetic
 208 and exhibits larger values of Ro . This is true even though the topographic
 209 orientation is reversed between these two experiments. In contrast, in Figure
 210 4(d,e), for the up-front wind experiments, the colder, “southern” flank of the
 211 jet is more energetic and exhibits larger values of Ro . However, the meridional
 212 asymmetry is less dramatic in these up-front wind experiments. Since all other
 213 parameters are the same for these five experiments, Figure 4 indicates that the
 214 orientations of the surface wind stress and the bathymetric slope not only influ-
 215 ence the amplitude of the submesoscale turbulence, but also its spatial patterns.
 216 (4) Finally, the time-averaged Ro peaks in the core of the slope front current in
 217 both of the down-front wind experiments (panels b,c), while it is suppressed in
 218 the core of the jet in the up-front wind experiments (panels d,e). In contrast,
 219 Ro is uniform with latitude, outside of the sponge layers, in the flat bottom
 220 Experiment (panel a).

221 The meridional distribution of the turbulence can be further explored by
 222 considering the energy content at different spatial scales as shown by the power
 223 spectra of surface kinetic energy (KE) and vertical velocity (Figure 5). In each
 224 panel, the domain is partitioned into regions on the northern (black, $100 <$
 225 $y < 300$) and southern (blue, $-300 < y < -100$) flanks of the jet as well as
 226 the jet cores (red, $-100 < y < 100$). Overall, the surface KE spectra have
 227 slopes close to k^{-2} , while the vertical velocity spectra have slopes close to k^{-1} .
 228 The spectral slope is steeper in the interior deeper ocean (not shown, see Klein
 229 et al. (2008)). For Experiment DF-S, the northern (warm) flank has a larger
 230 KE spectral amplitude. The northern flank also exhibits larger amplitude in
 231 the vertical velocity spectral curve, consistent with the asymmetry in Figure

232 4b. In addition to having a larger amplitude, Figure 5d also shows that the
233 northern flank surface vertical velocity spectra has a slope of $k^{-0.57}$, which is
234 significantly shallower than in all other simulations. A shallow slope implies a
235 greater proportion of energy is found at higher wavenumbers or smaller scales.
236 In the control Experiment, DF-FI, surface KE and vertical velocity spectra do
237 not show significant north to south differences in either amplitude or spectral
238 slopes. The north-to-south asymmetry near the surface is largest in Experiment
239 DF-S. The spectral slope in Experiment DF-N is similar to Experiment DF-S,
240 although the amplitude is larger in DF-S. In the UF experiments, where the
241 wind forcing is to the opposite direction of the thermal-wind balanced flow
242 (Experiments UF-S, UF-N), the surface turbulence spectra is not modified as
243 strongly by the bathymetry. Kinetic energy and vertical velocity spectra in
244 Experiments UF-S and UF-N are similar to the control Experiment DF-FI (not
245 shown).

246 In all experiments, cyclonic vortices are more prevalent near the surface than
247 anticyclonic vortices, resulting in a preference for positive Ro . As mentioned in
248 the introduction, this is consistent with many previous studies (Munk et al.
249 (2000), Lazar et al. (2013b), Buckingham et al. (2016) to name a few), and is
250 a possible signature of the flow's geostrophic imbalance. In each of our simula-
251 tions, we choose a shallow layer at 10 m depth and calculate the Ro probability
252 density functions (PDF) as shown in Figure 6a. The mean PDFs for all exper-
253 iments show an asymmetric distribution between positive and negative values
254 with larger tails on the positive side. The skewness, as measured by the third
255 moment of Ro , is positive in all experiments.

256 Away from the surface, Ro decays to smaller values, roughly by a factor
257 of 3 at 180 m depth (Figure 6b, also shown in Klein et al. (2008)). PDF
258 skewness of Ro in the interior also decreases to smaller values compared to
259 that close to the surface, and in DF-N, the skewness of Ro decays altogether.
260 The relative strength of the skewness across the different experiments remains
261 unchanged away from the surface. The down-front wind experiments, DF-N and
262 DF-S exhibit the minimum and maximum values of the skewness parameter,

263 respectively, both at the surface and in the interior. The mean of these values is
 264 approximately equal to the skewness that occurs in the flat bottom experiment.
 265 This is partially a feature of the influence of the topography on the skewness
 266 giving rise to regions within a single experiment where skewness is stronger or
 267 weaker.

268 The spatially-asymmetric pattern of the flow’s turbulent characteristics across
 269 the northern and southern flanks of the jet can be linked to the potential vor-
 270 ticity (PV) gradients in the fluid interior. The Ertel PV is defined as:

$$PV = \left(f\hat{\mathbf{k}} + \nabla \times \mathbf{u} \right) \cdot \nabla b, \quad (5)$$

271 where the buoyancy b , is a linear function of θ in our model. The interior
 272 of the model domain is largely adiabatic, therefore we expect PV anomalies
 273 to be generated primarily at interfaces, for example due to the surface wind
 274 stress or bottom friction. Figure 7 shows vertical cross sections of PV with
 275 potential temperature contours for each Experiment. Due to its large variations
 276 with depth, PV is shown in a logarithmic scale. Low PV is generated near the
 277 surface frontal regions due to wind stress, inducing lateral Ekman transport as
 278 well as strong vertical mixing. At the bottom, momentum input by the wind
 279 forcing is balanced by friction. At the same time, bottom friction drives Ekman
 280 transport to the right hand side of the zonal flow. Therefore in Experiments
 281 DF-S and UF-N, bottom Ekman transport moves dense water below light water,
 282 acting as a PV source (measured by the absolute value); while in Experiments
 283 DF-N and UF-S, bottom Ekman transport extracts PV from the fluid, acting
 284 as a PV sink. These anomalies only occur on the isopycnal layers that directly
 285 intersect with the topography. With westerly wind in Experiments DF-S and
 286 DF-N, bottom Ekman transport tilts the isopycnal layers upslope in DF-S and
 287 downslope in DF-N. As a consequence, in the shallower fluid interior (around
 288 100 m depth), interior PV gradients are generated due to the change of isopycnal
 289 layer thickness. These modifications to the background stratification lead to
 290 the preferential formation of submesoscale eddies on the flank of the jet where
 291 stratification is weak. Conversely, submesoscale eddies are suppressed over the

292 flank of the jet where the stratification is intensified. For the experiments where
 293 the winds are easterly (UF-S and UF-N), the interior PV tends to be larger
 294 (Figure 7), and therefore the distribution of Ro is different (Figure 4). For
 295 the UF cases, the outcropping isopycnals are advected southward, which both
 296 flattens the isopycnals generates a stronger vertical stratification on the northern
 297 flank of the jet.

298 In the flat bottom Experiment DF-F1, the PV structure is more uniform
 299 in the vertical direction. Critically, only a small temperature or density range
 300 outcrops on the bottom. The isopycnals that outcrop vary over relatively large
 301 scales (approximately the domain size). Thus Ekman transport is unable to
 302 generate large PV anomalies near the bottom in this experiment. By comparing
 303 Experiment DF-F1 with other experiments, we also confirm that PV changes
 304 are mainly attributed to the modulation of bottom topographic slope, and not
 305 to the surface wind forcing alone.

306 To show the coherent PV patterns from the bottom to the surface, in Ex-
 307 periment DF-S for example, we project PV onto different isopycnal layers in
 308 Figure 8. The PV on the three layers shows similar patterns, related to the
 309 anomalies either due to the wind forcing at the surface or the bottom friction.
 310 Even on the $14^{\circ}C$ isopycnal layer which neither intersects with the surface nor
 311 the bottom, we still see PV patterns affected by the layer thickness modulations
 312 from above and below. This shows that PV sources/sinks at the bottom due
 313 to Ekman transport can affect the stratification in the isopycnal layers above.
 314 Corresponding time and zonal mean PV fluxes are also calculated in each isopy-
 315 cnal layer as $\overline{\langle PV \cdot \mathbf{v} \rangle}^{x,t}$, where \mathbf{v} is the interpolated meridional velocity in
 316 each snapshot. Mean PV flux has opposite sign to the PV gradient. In the layer
 317 that intersects with the slope, negative PV flux is generated near the slope and
 318 results in a low PV region.

319 4. Discussion

320 4.1. Spectral slope

321 The spectral representation of the velocity field has been a powerful tool
322 for distinguishing flows in mesoscale and submesoscale regimes. At the outset
323 of the study, we described the submesoscale range as those scales at which
324 Ro becomes $O(1)$ and therefore, ageostrophic motions, by definition, become
325 relevant. Callies and Ferrari (2013), using an objective rather than a dynamic
326 definition, identified submesoscales using a wavelength range from 1 to 200 km,
327 and used observation-based spectra of eddy kinetic energy to determine the
328 contribution from balanced and unbalanced motions at these scales. In the Gulf
329 Stream region, within the mixed layer, a transition between balanced, interior
330 quasi-geostrophic motion and unbalanced, predominantly internal wave motion,
331 occurs at roughly 20 km. At scales smaller than 20 km, unbalanced motion was
332 found to dominate the energy spectrum, and spectral slopes consistent with
333 surface quasi-geostrophic (SQG) predictions (Klein et al., 2008) were not found.
334 Additionally, in a more quiescent region in the eastern Pacific, kinetic energy
335 distributions were not consistent with SQG, nor did they reveal a geostrophic
336 turbulence regime (spectral slope of k^{-3}).

337 Klein et al. (2008) concluded that near surface kinetic energy spectra show a
338 k^{-2} slope, which is significantly shallower than that in the deeper ocean (k^{-4}).
339 Mixed layer baroclinic and symmetric instabilities may enhance submesoscale
340 turbulence and flatten the spectra (Capet et al., 2008). In our simulations, sur-
341 face kinetic energy spectra show a similar slope of k^{-2} despite the introduction
342 of a continental slope. Callies and Ferrari (2013) argued that the disagreement
343 with SQG theory arose from the injection of energy in the submesoscale range
344 by small-scale baroclinic instabilities or from a coupling between surface and
345 interior dynamics. While we do not resolve internal waves in these experiments,
346 we speculate that the introduction of a topographic slope may impact the wave-
347 length at which the transition between balanced and unbalanced motions occur.
348 Both of these processes are likely to be active in producing the spectra diagnosed

349 from our simulations.

350 Callies and Ferrari (2013) found a similar near-surface k^{-2} slope when an-
351 alyzing observations from the subtropic North Pacific gyre, however they dis-
352 carded the link of this slope to SQG dynamics due to the fact that this region
353 has non-uniform stratification, from which the k^{-2} scaling arises in Klein et al.
354 (2008). For our simulations, we introduce a stratification with a vertical tem-
355 perature decay, which should result in a kinetic energy slope that is flatter than
356 k^{-2} . Finally, the spectra show a weak dependence with depth, which also con-
357 tradicts SQG theory. Thus we conclude that our shallow spectra are not results
358 of near-surface SQG dynamics, but rather with the generation of unbalanced,
359 ageostrophic motions.

360 Typical explanations for the failure of geostrophic balanced motion include
361 frontal circulations, Ekman flows, mixed layer turbulence, near-inertial oscil-
362 lations, and internal tides. We can eliminate internal tides because they are
363 not included in our simulations. However, both frontal circulations and Ekman
364 flows are likely to play a critical part in generating the flatter spectra and also
365 in explaining the diversity of spectral slopes seen across the different simula-
366 tions. To assess the importance of Ekman flows and mixed layer turbulence,
367 we have analyzed the vertical structure of the EKE in our various simulations
368 (Figure 9). Experiment DF-N shows the largest degree of vertical decay of the
369 EKE amplitude, where all the other experiments show similar levels of EKE
370 throughout the upper 200 m of the domain. The DF-N experiment also shows
371 the smallest vorticity skewness (Figure 6), which decays completely in only 180
372 m depth. This is also consistent with the fact that in Experiment DF-N the PV
373 is approximately constant throughout the water column (Figure 7).

374 Rosso et al. (2015) studied the spatial inhomogeneity in submesoscale tur-
375 bulence and proposed that topography influences submesoscale dynamics indi-
376 rectly through the interaction with the large scale flow. Here we showed that
377 kinetic energy spectra display a north to south asymmetry over the topographic
378 slope. Next we will demonstrate that this is due to the topographic modifica-
379 tion of background PV, which suppresses turbulence over one side of the domain

380 (section 4.2).

381 Compared to kinetic energy, vertical velocity is of greater biogeochemical
382 interest as it influences the transport of nutrients from greater depths to the
383 surface. In this study, we also calculate the spectra of surface vertical velocity.
384 It has a spectral slope of k^{-1} , consistent with Levy et al. (2012), in which the
385 co-spectra of $w \cdot NO_3$ are studied. Vertical velocity spectra are also strongly
386 modified by the bathymetry in both absolute value and power spectrum slope.
387 Regions with larger EKE are associated with larger vertical velocities.

388 *4.2. Interior PV gradients*

389 In this section, we link changes in submesoscale characteristics to the dis-
390 tribution of PV in each of the simulations. These distributions have a strong
391 impact on the characteristics and amplitude of the mesoscale vorticity field,
392 which is responsible for generating horizontal buoyancy gradients that catalyze
393 submesoscale instabilities. This relationship emphasizes the strong connection
394 between the surface submesoscale field and the interior dynamics.

395 There are three physical processes that are responsible for setting the inte-
396 rior stratification: (a) thermal forcing from the lateral boundaries; (b) modifi-
397 cation of the isopycnals over the continental slope related to PV conservation
398 (this tends to generate isopycnals that slope in a similar sense to the bottom
399 topography) (Isachsen, 2011; Stewart and Thompson, 2013) and (c) Ekman con-
400 vergence and divergence caused by frictional processes at both top and bottom
401 boundaries (Thomas, 2005). Figure 7 shows that in all simulations, a broad
402 region at the surface, which spans the latitudes that feel a surface wind forcing
403 exhibits low PV reflecting a weak surface stratification. The generation of this
404 low PV layer is due to the inclusion of the KPP parameterization scheme in the
405 numerical model, which keeps the mixed layer approximately constant at 40 m.
406 The presence of this relatively well-mixed surface layer preconditions the verti-
407 cal stratification to be weak and that can potentially generate low Richardson
408 number flows. We note that low or even positive PV values may be generated
409 in these simulations when lateral buoyancy gradients exceed the size of vertical

410 buoyancy gradients. These conditions may be suitable to mixed layer instabil-
411 ity (Boccaletti et al., 2007; Mahadevan et al., 2010) or symmetric instability
412 (Hoskins, 1974), which would work to restratify the mixed layer. However, for
413 symmetric instability, our simulations do not have sufficient resolution to cap-
414 ture the evolution of secondary instabilities that would lead to diabatic mixing
415 (Taylor and Ferrari, 2009; Bachman and Taylor, 2014).

416 In each simulation, the wind stress generates a mean flow that is in the same
417 direction as the surface wind stress (see contours in Figure 9). In experiments
418 where the wind stress is *down-front*, in the sense of the thermal forcing from the
419 boundaries, the mean wind-driven overturning increases the isopycnal tilt (Fig-
420 ure 7). The generation of mesoscale eddies via baroclinic instability saturates
421 this process. In the experiments where the wind forcing is *up-front*, the (Exper-
422 iment UF-S and UF-N) the surface wind forcing is sufficiently large to generate
423 a V-shaped pattern in the isopycnals, which will act to localize the instabil-
424 ity processes. These surface forcings have a significant impact on the interior
425 PV distributions. In regions where the Ekman flow is predominantly divergent,
426 isopycnal surfaces are pushed up towards the surface, which enhances the verti-
427 cal stratification and the background PV. This is apparent on the jet’s southern
428 flank in Experiments DF-S and DF-N and on the northern flank in Experiments
429 UF-S and UF-N. Conversely, the stratification and the PV is suppressed on the
430 opposite flank. In these low PV regions, the potential for generation of sub-
431 mesoscale processes is enhanced. This explains why in both Experiments DF-S
432 and DF-N, turbulence is more energetic at smaller scales on the northern flank
433 of the jet. Here the amplitude of PV is reduced as a result of convergent Ekman
434 transport.

435 This localization of regions that are preferentially susceptible to subme-
436 soscale motions is also apparent when comparing Experiments DF-S and UF-S.
437 In the former, PV is minimized at the core of the jet, whereas in the latter
438 PV is maximized at the core of the jet. Again, the Ekman transport cause the
439 outcropping isopycnals to be advected southward, increasing the near-surface
440 vertical stratification across the core of the jet. As a result, in Experiment DF-

441 S, the Rossby number is elevated in the jet core, while in Experiment UF-S, the
442 Rossby number is suppressed at the jet core.

443 Fine spatial variability in the PV distributions also occurs near the bottom
444 boundary. Figure 10 compares vertical kinetic energy as $\rho w^2/2$ in all the simu-
445 lations, where w is vertical velocity and ρ is density. Here, frictional processes in
446 the bottom boundary layer can, with a laterally-sheared mean flow, give rise to
447 significant vertical velocities that influence the near-bottom stratification (Ben-
448 thuyssen and Thomas, 2013; Ruan and Thompson, 2016).

449 Over the continental slope, Ekman overturning acts as a PV sink in Exper-
450 iment DF-N and UF-S, resulting in a low PV region. This region is associated
451 with large vertical velocity and Ro . We compare the vertical structures of Ro
452 for Experiment DF-S and UF-S in Figure 11. It is evident that in Experiment
453 UF-S, Ekman overturning due to friction produces large Ro at 300 m depth. Ro
454 close to the bathymetry is even larger than that at 150 m depth. In contrast,
455 for Experiment DF-S, bottom friction is a source of PV, which inhibits the gen-
456 eration of large w or Ro . In Figure 11 a-c, Ro decays in magnitude through the
457 water column; there is no near-bottom enhancement.

458 In summary, the interaction of surface wind forcing, a strong mean flow
459 and a topographic slope can lead to substantial changes in the interior PV
460 over relatively short distances. These are reflected in the characteristics of the
461 submesoscale motions, which are more active in low PV regions.

462 *4.3. Interaction between mesoscale and submesoscale*

463 Topography influences submesoscale motions primarily through mesoscale
464 eddies. The interaction between the mesoscale and submesoscale motions can
465 be studied through the correlation between submesoscale vertical velocities and
466 mesoscale EKE (Rosso et al., 2015). Isachsen (2011) has shown that eddy diffu-
467 sivities in the ocean is sensitive to the ratio of topographic slope and isopycnal
468 slope. In this study, all simulations with a topographic slope exhibit stronger
469 isopycnal tilt than the flat-bottom control experiment, DF-F1. However, the
470 equilibrated EKE levels are spatially more complex, which is due to a tendency

471 for a continental slope to dampen EKE levels. Over a steep continental slope,
472 baroclinic instability is inhibited and EKE becomes smaller compared with a
473 flat bottom experiment (Figure 9).

474 Comparing Figure 10 with Figure 9, we find that regions with enhanced
475 submesoscale vertical velocities are also associated with larger mesoscale eddy
476 kinetic energies. Similar to Ro and the vertical velocities, EKE also shows
477 an asymmetric distribution between the northern and southern flanks of the
478 front, with larger values associated with weaker stratification. The only counter-
479 intuitive case is Experiment DF-N, in which submesoscale motions are enhanced
480 in the northern flank of the front but EKE is suppressed in the same region. The
481 low EKE in the northern flank is mainly due to the isopycnal layers that interact
482 with both the surface and the bathymetry (Figure 6). The transport of EKE
483 from the frontal region to the northern flank is constrained by the isopycnal
484 layers that outcrop on the continental slope and do not extend to the northern
485 boundary. This results in a low EKE region coupled with a weak background
486 PV and vertical stratification that still supports a shallow submesoscale field.

487 5. Conclusion

488 In this study, we examine the modulation of surface turbulence characteris-
489 tics related to wind-induced frontal currents formed over a topographic slope.
490 We link the surface properties to changes in interior PV distributions related
491 to the orientation of the surface wind stress and the continental slope. Ekman
492 transport over a topographic slope can generate low or high PV regions in the
493 ocean interior, associated with weak or strong stratification near the surface,
494 respectively. We find that this variability in the surface stratification generates
495 meridional asymmetry in the kinetic energy spectra as well as the amplitude
496 and skewness of the Rossby number. Variations in surface submesoscale turbu-
497 lence by the topography is mainly through the modulation of mesoscale stirring,
498 which is evident from the correlation between near-surface EKE and the ampli-
499 tude of turbulent vertical velocities. In addition to the modulation of surface

500 turbulence, down-slope Ekman transport also generates a low PV region near
501 the ocean floor and give rises to large vertical velocities near the ocean bottom.

502 The main conclusions of the study are summarized as follows:

- 503 1. Surface vorticity characteristics are modified by the presence of a sloping
504 bottom. Most of the persistent eddies near the surface are cyclonic.
- 505 2. The sloping bottom modifies the spectra of near-surface vertical velocities
506 and kinetic energies. Velocity spectra exhibit spatial asymmetries between
507 the northern and southern flanks of the domain.
- 508 3. Surface turbulence characteristics are linked to modifications of the inte-
509 rior PV gradients, which are generated by the Ekman transport along the
510 sea surface and along the bottom.
- 511 4. These results are not consistent with SQG theory and suggest the criti-
512 cal role of ageostrophic velocities generated both at surface and bottom
513 boundaries.

514 These results suggest that along-slope wind stress and slope orientation exert
515 substantial influence over the transport and mixing across the continental shelf,
516 with implications for the exchanges of mass, heat, salt, and biogeochemical
517 tracers in coastal waters.

518 **Acknowledgment**

519 We acknowledge assistance from Andrew Stewart in configuring the numer-
520 ical simulations as well as helpful conversations from Xiaozhou Ruan and Mar
521 Flexas. AFT was supported by NSF grant OPP-1246460; AL was supported by
522 NSF grant OCE-1235488.

523 **Reference**

- 524 Afanasyev, Y. D. and W. R. Peltier, 1998: Three-dimensional instability of an-
525 ticyclonic swirling flow in rotating fluid: Laboratory experiments and related
526 theoretical predictions. *Phys. Fluids*, **10** (12), 3194–3202.
- 527 Bachman, S. and J. Taylor, 2014: Modelling of partially-resolved oceanic sym-
528 metric instability. *Oc. Modell.*, **82**, 15–27.
- 529 Benthuisen, J. and L. N. Thomas, 2012: Friction and diapycnal mixing at a
530 slope: Boundary control of potential vorticity. *J. Phys. Oceanogr.*, **42** (9),
531 1509–1523.
- 532 Benthuisen, J. A. and L. N. Thomas, 2013: Nonlinear stratified spindown over
533 a slope. *J. Fluid Mech.*, **726**, 371–403.
- 534 Boccaletti, G., R. Ferrari, and B. Fox-Kemper, 2007: Mixed layer instabilities
535 and restratification. *J. Phys. Oceanogr.*, **37** (9), 2228–2250.
- 536 Buckingham, C., et al., 2016: Seasonality of submesoscale flows in the ocean
537 surface boundary layer. *Geophys. Res. Lett.*, **43**, 2118–2126.
- 538 Callies, J. and R. Ferrari, 2013: Interpreting energy and tracer spectra of upper-
539 ocean turbulence in the submesoscale range (1-200 km). *J. Phys. Oceanogr.*,
540 **43** (11), 2456–2474.
- 541 Capet, X., J. C. McWilliams, M. J. Mokemaker, and A. F. Shchepetkin, 2008:
542 Mesoscale to submesoscale transition in the california current system. part i:
543 Flow structure, eddy flux, and observational tests. *J. Phys. Oceanogr.*, **38** (1),
544 29–43.
- 545 DAsaro, E., C. Lee, L. Rainville, R. Harcourt, and L. Thomas, 2011: Enhanced
546 turbulence and energy dissipation at ocean fronts. *Science*, **332** (6027), 318–
547 322.
- 548 Eldevik, T. and K. B. Dysthe, 2002: Spiral eddies. *J. Phys. Oceanogr.*, **32** (3),
549 851–869.

- 550 Fox-Kemper, B., R. Ferrari, and R. Hallberg, 2008: Parameterization of mixed
551 layer eddies. part i: Theory and diagnosis. *J. Phys. Oceanogr.*, **38** (6), 1145–
552 1165.
- 553 Hart, J. E., 1975: Baroclinic instability over a slope .1. linear theory. *J. Phys.*
554 *Oceanogr.*, **5** (4), 625–633.
- 555 Hoskins, B. J., 1974: The role of potential vorticity in symmetric stability and
556 instability. *Quart. J. R. Meteorol. Soc.*, **100**, 480–482.
- 557 Hoskins, B. J., 1982: The mathematical-theory of frontogenesis. *Ann. Rev. Fluid*
558 *Mech.*, **14**, 131–151.
- 559 Isachsen, P. E., 2011: Baroclinic instability and eddy tracer transport across
560 sloping bottom topography: How well does a modified eady model do in
561 primitive equation simulations? *Oc. Modell.*, **39** (1-2), 183–199.
- 562 Klein, P., B. L. Hua, G. Lapeyre, X. Capet, S. Le Gentil, and H. Sasaki,
563 2008: Upper ocean turbulence from high-resolution 3d simulations. *J. Phys.*
564 *Oceanogr.*, **38** (8), 1748–1763.
- 565 Klein, P. and G. Lapeyre, 2009: The oceanic vertical pump induced by mesoscale
566 and submesoscale turbulence. *Ann. Rev. Mar. Sci.*, **1**, 351–375.
- 567 Kloosterziel, R. C., G. F. Carnevale, and P. Orlandi, 2007: Inertial instability
568 in rotating and stratified fluids: barotropic vortices. *J. Fluid Mech.*, **583**,
569 379–412.
- 570 Large, W. G., G. Danabasoglu, S. C. Doney, and J. C. McWilliams, 1997:
571 Sensitivity to surface forcing and boundary layer mixing in a global ocean
572 model: Annual-mean climatology. *J. Phys. Oceanogr.*, **27** (11), 2418–2447.
- 573 Lazar, A., A. Stegner, R. Caldeira, C. Dong, H. Didelle, and S. Viboud, 2013a:
574 Inertial instability of intense stratified anticyclones. part 2. laboratory exper-
575 iments. *J. Fluid Mech.*, **732**, 485–509.

- 576 Lazar, A., A. Stegner, and E. Heifetz, 2013b: Inertial instability of intense
577 stratified anticyclones. part 1. generalized stability criterion. *J. Fluid Mech.*,
578 **732**, 457–484.
- 579 Levy, M., R. Ferrari, P. J. S. Franks, A. P. Martin, and P. Riviere, 2012: Bring-
580 ing physics to life at the submesoscale. *Geophys. Res. Lett.*, **39**.
- 581 Mahadevan, A. and D. Archer, 2000: Modeling the impact of fronts and
582 mesoscale circulation on the nutrient supply and biogeochemistry of the upper
583 ocean. *J. Geophys. Res.*, **105 (C1)**, 1209–1225.
- 584 Mahadevan, A., A. Tandon, and R. Ferrari, 2010: Rapid changes in mixed layer
585 stratification driven by submesoscale instabilities and winds. *J. Geophys. Res.*,
586 **115**.
- 587 Mensa, J. A., Z. Garraffo, A. Griffa, T. M. Ozgokmen, A. Haza, and
588 M. Veneziani, 2013: Seasonality of the submesoscale dynamics in the gulf
589 stream region. *Ocean Dynamics*, **63 (8)**, 923–941.
- 590 Munk, W., L. Armi, K. Fischer, and F. Zachariasen, 2000: Spirals on the sea.
591 *Proc. R. Soc. Lond. A*, **456 (1997)**, 1217–1280.
- 592 Omand, M. M., E. A. D’Asaro, C. M. Lee, M. J. Perry, N. Briggs, I. Cetinic,
593 and A. Mahadevan, 2015: Eddy-driven subduction exports particulate organic
594 carbon from the spring bloom. *Science*, **348 (6231)**, 222–225.
- 595 Poulin, F. J. and G. R. Flierl, 2005: The influence of topography on the stability
596 of jets. *J. Phys. Oceanogr.*, **35 (5)**, 811–825.
- 597 Rosso, I., A. M. Hogg, A. E. Kiss, and B. Gayen, 2015: Topographic influence
598 on submesoscale dynamics in the southern ocean. *Geophys. Res. Lett.*, **42 (4)**,
599 1139–1147.
- 600 Rosso, I., A. M. Hogg, P. G. Strutton, A. E. Kiss, R. Matear, A. Klocker, and
601 E. van Sebille, 2014: Vertical transport in the ocean due to sub-mesoscale
602 structures: Impacts in the kerguelen region. *Oc. Modell.*, **80**, 10–23.

- 603 Ruan, X. and A. Thompson, 2016: Bottom boundary potential vorticity injection
604 from an oscillating flow: a pv pump. *in review, J. Phys. Oceanogr.*
- 605 Sasaki, H., P. Klein, B. Qiu, and Y. Sasai, 2014: Impact of oceanic-scale interactions
606 on the seasonal modulation of ocean dynamics by the atmosphere. *Nat. Comm.*, **5**.
- 608 Shcherbina, A. Y., E. A. D’Asaro, C. M. Lee, J. M. Klymak, M. J. Mole-
609 maker, and J. C. McWilliams, 2013: Statistics of vertical vorticity, divergence,
610 and strain in a developed submesoscale turbulence field. *Geophys. Res. Lett.*,
611 **40 (17)**, 4706–4711.
- 612 Siegel, A., J. B. Weiss, J. Toomre, J. C. McWilliams, P. S. Berloff, and I. Yavneh,
613 2001: Eddies and vortices in ocean basin dynamics. *Geophys. Res. Lett.*,
614 **28 (16)**, 3183–3186.
- 615 Spall, M. A., 2013: Dense water formation around islands. *J. Geophys. Res.*,
616 **118 (5)**, 2507–2519.
- 617 Stern, A., L.-P. Nadeau, and D. Holland, 2015: Instability and mixing of zonal
618 jets along an idealized continental shelf break. *J. Phys. Oceanogr.*, **45 (9)**,
619 2315–2338.
- 620 Stewart, A. and A. Thompson, 2015: The temporal residual mean overturning
621 circulation in neutral density coordinates. *Oc. Modell.*, **in press**.
- 622 Stewart, A. L. and A. F. Thompson, 2013: Connecting antarctic cross-slope
623 exchange with southern ocean overturning. *J. Phys. Oceanogr.*, **43 (7)**, 1453–
624 1471.
- 625 Taylor, J. and R. Ferrari, 2009: On the equilibration of a symmetrically unstable
626 front via a secondary shear instability. *J. Fluid Mech.*, **622**, 103–113.
- 627 Thomas, L. N., 2005: Destruction of potential vorticity by winds. *J. Phys.*
628 *Oceanogr.*, **35 (12)**, 2457–2466.

- 629 Thomas, L. N., A. Tandon, and A. Mahadevan, 2008: Submesoscale processes
630 and dynamics. *Ocean Modeling in an Eddying Regime, Geophys. Monogr. Ser.*,
631 **177**, 17–38.
- 632 Thomas, L. N., J. R. Taylor, R. Ferrari, and T. M. Joyce, 2013: Symmetric
633 instability in the gulf stream. *Deep Sea Res. II*, **91**, 96–110.
- 634 Thompson, A., A. Lazar, C. Buckingham, A. N. Garabato, G. Damerell, and
635 K. Heywood, 2016: Open-ocean submesoscale motions: A full seasonal cycle
636 of mixed layer instabilities from gliders. *J. Phys. Oceanogr.*, **46**, 1285–1307.
- 637 Thompson, A. F., 2010: Jet formation and evolution in baroclinic turbulence
638 with simple topography. *J. Phys. Oceanogr.*, **40 (2)**, 257–278.
- 639 Thompson, A. F. and K. J. Heywood, 2008: Frontal structure and transport in
640 the northwestern Weddell Sea. *Deep Sea Res. I*, **55**, 1229–1251.
- 641 Thompson, A. F., K. J. Heywood, S. Schmidtke, and A. L. Stewart, 2014: Eddy
642 transport as a key component of the antarctic overturning circulation. *Nat.*
643 *Geosci.*, **7 (12)**, 879–884.
- 644 Wang, D. P. and A. Jordi, 2011: Surface frontogenesis and thermohaline intru-
645 sion in a shelfbreak front. *Oc. Modell.*, **38 (1-2)**, 161–170.

Table 1: Simulation configurations. The five experiments correspond to the schematics in Figure 2. The identifying characteristics include the wind and topography orientation. The front velocity is determined from the location where $|\bar{u}(y)|$ is greatest.

Experiment Number	Experiment ID	surface wind orientation	shelf location	front zonal velocity (m s ⁻¹)
1	DF-F1	down-front	flat bottom	0.1895
2	DF-S	down-front	south	0.4047
3	DF-N	down-front	north	0.4086
4	UF-S	up-front	south	-0.2589
5	UF-N	up-front	north	-0.3694

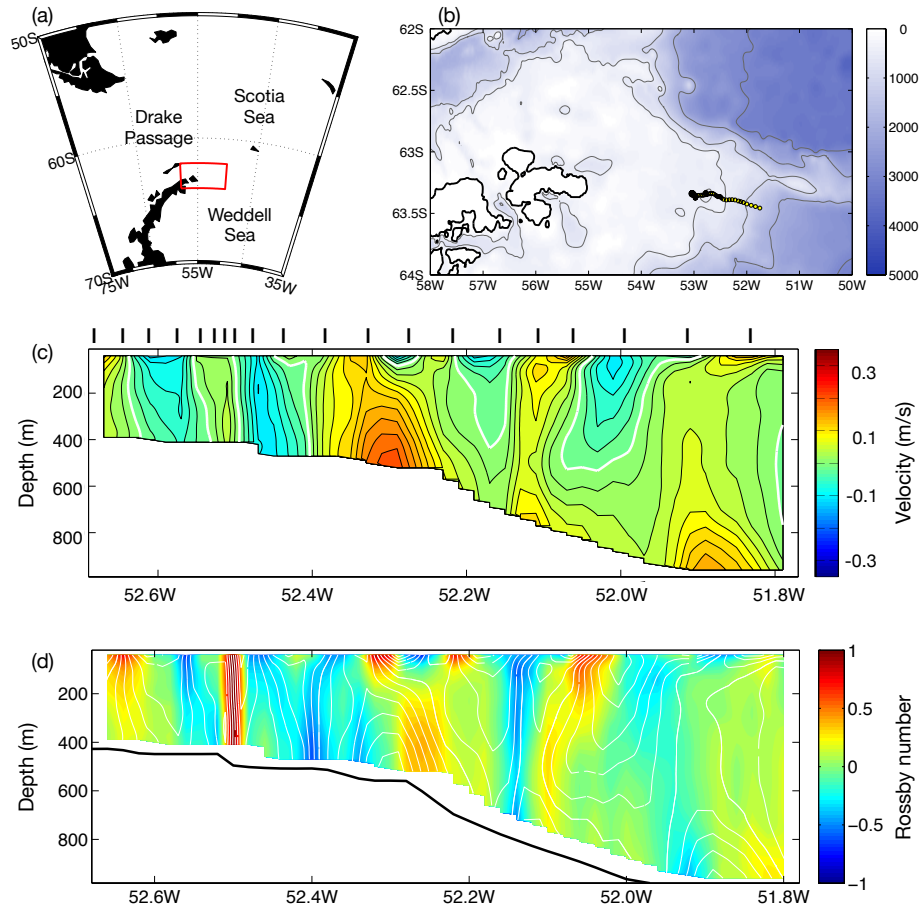


Figure 1: (a) Overview map of the Weddell Sea sector of the Southern Ocean. An enhanced view of the red box is shown in panel (b) where the bathymetry is given in color. The yellow dots in panel (b) correspond to a single hydrographic transect collected by an ocean glider in January 2012. Vertical, cross-slope section of (c) cross-track v (along-slope) velocity and (d) Rossby number approximated by v_x/f , where x is the off-shore direction. Tick marks at the top of panel (c) indicate the surfacing positions of each glider dive. See Thompson et al. (2014) for further details.

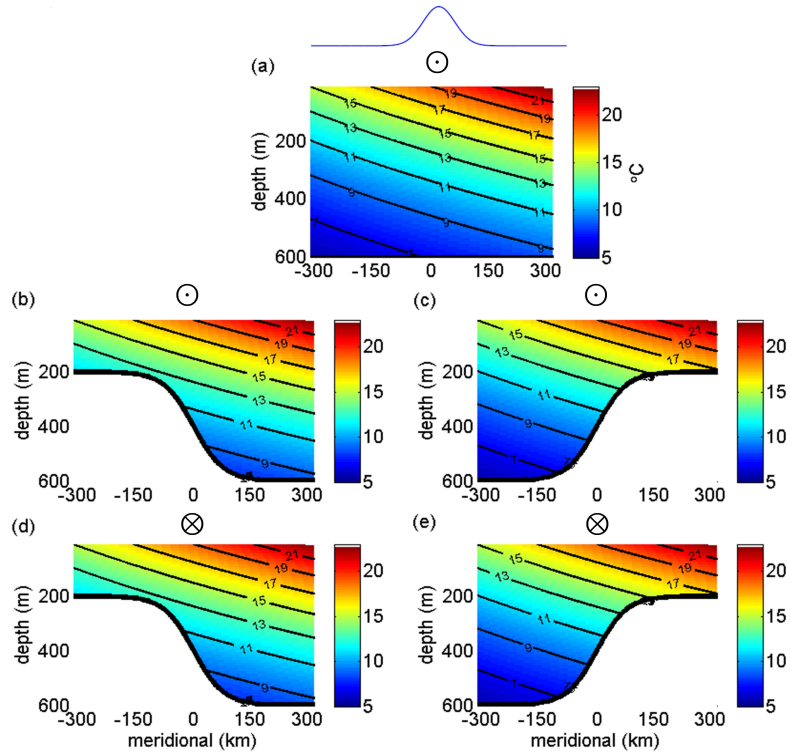


Figure 2: Schematic overview of the model configuration for the five simulations described in Table 1. Panels (a)-(e) correspond to experiments (1)-(5). Colors and contours show the zonally-uniform initial temperature profile. The temperature is relaxed to these initial values at the northern and southern boundaries. The thick black curve marks the bathymetry, while the circle over each panel marks the wind orientation: down-front (dots) or up-front (crosses). Blue curve on the top of panel (a) shows the surface wind stress profile, with a peak value $\tau_0 = 0.05 \text{ N m}^{-2}$.

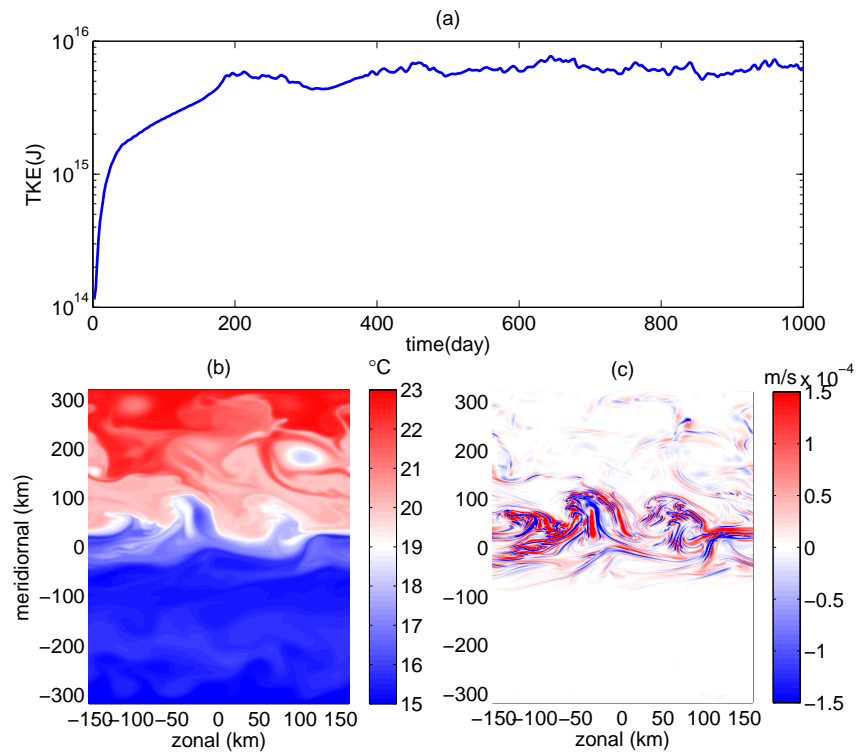


Figure 3: (a) Growth of total kinetic energy in Experiment DF-S. (b) Snapshots at day 900 for Experiment DF-S (Table 1) surface potential temperature ($^{\circ}\text{C}$) at 10 m depth. (c) Same as b, for vertical velocity w (10^{-4} m s $^{-1}$) at 30 m depth.

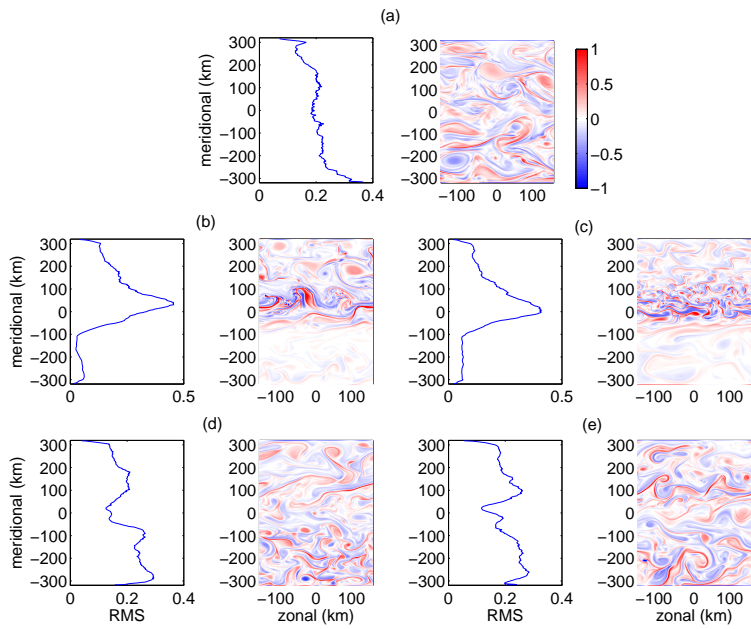


Figure 4: Near-surface Rossby number, $Ro = \zeta/f$, at 10m depth for the five experiments described in Table 1: (a) DF-F1, (b) DF-S, (c) DF-N, (d) UF-S, (e) UF-N. The left-hand plot in each plan shows the zonally-averaged root mean square (RMS) Ro averaged over a period of 200 days. The right-hand plot is a snapshot of surface Ro at day 900.

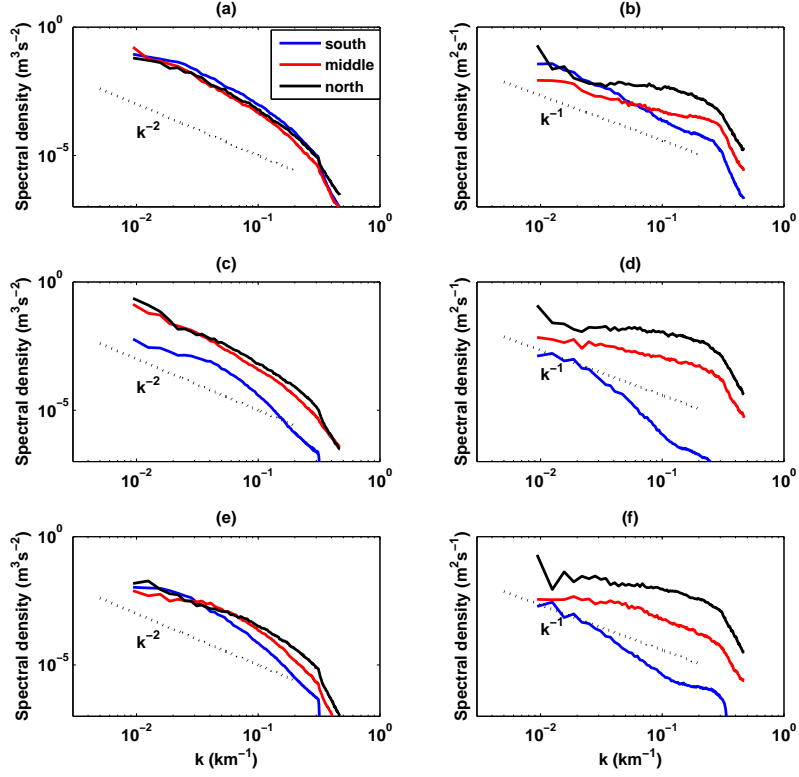


Figure 5: Spectra of surface horizontal kinetic energy (10 m depth, left panels) and vertical velocity (30 m depth, right panels) averaged from day 800 to 1000. (a) Kinetic energy spectra and (b) vertical velocity spectra in Experiment DF-FI. (c) Kinetic energy spectra and (d) vertical velocity spectra in Experiment DF-S. (e) Kinetic energy spectra and (f) vertical velocity spectra in Experiment DF-N. Dotted lines represent k^{-1} and k^{-2} spectral slope, provided for reference. Blue lines represent the southern flank of the domain from $-300 \text{ km} < y < -100 \text{ km}$. Red lines represent the middle of the domain (frontal region) from $-100 \text{ km} < y < 100 \text{ km}$. Black lines represent the northern flank of the domain from $100 \text{ km} < y < 300 \text{ km}$. Spectra in Experiments UF-S and UF-N are similar to those in the control Experiment DF-FI, and are not shown in this figure.

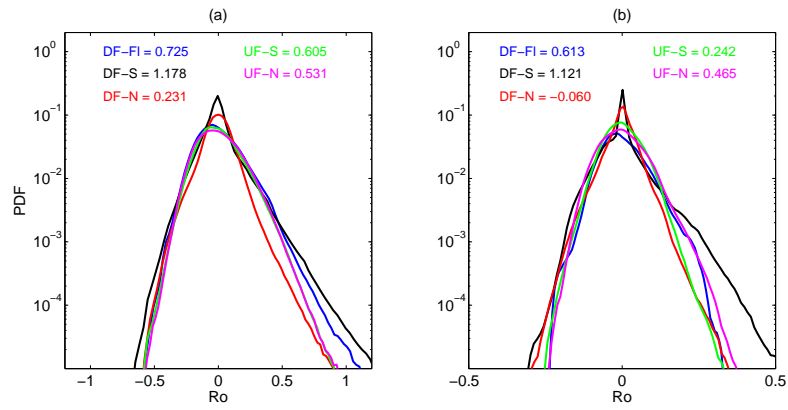


Figure 6: Probability density function (PDF) for (a) surface Rossby number, and (b) Rossby number at 180m depth averaged from day 800 to 1000 for Experiment (1) - (5). Values of PDF skewness are labeled using the same color for each Experiment.

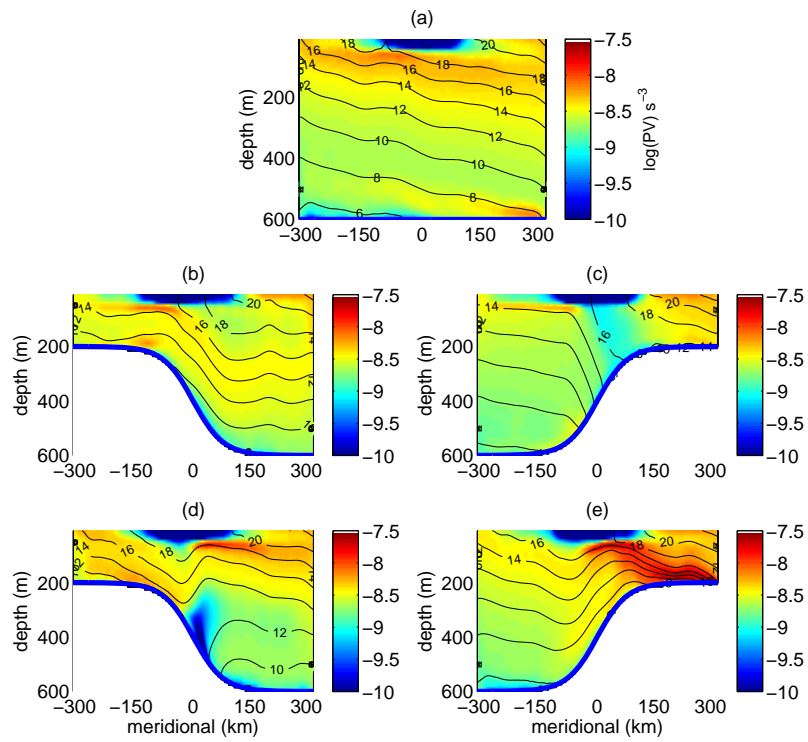


Figure 7: PV cross section in the middle of the domain ($x = 0$) averaged from day 800 to 1000 for five experiments. Values are displayed in \log_{10} scale. Black contours show the mean potential temperature, also indicate isopycnal surfaces.

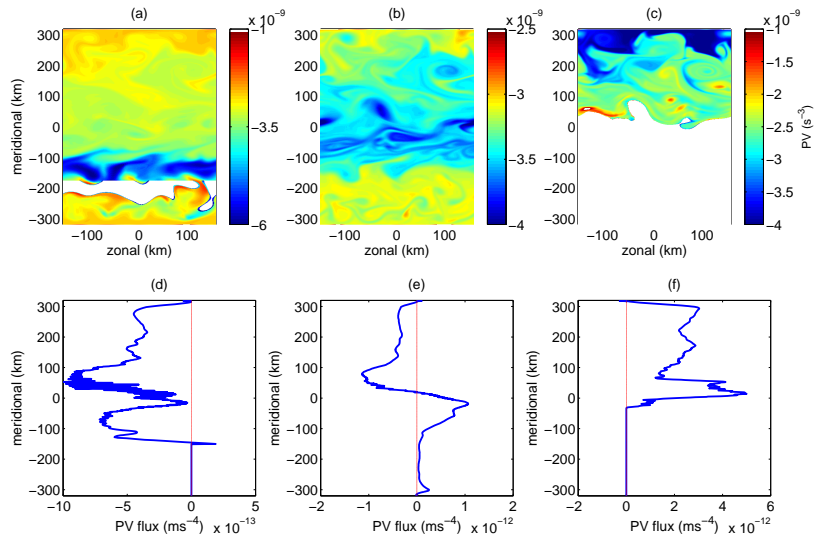


Figure 8: Upper panels are PV snapshots on the 12°C (a), 14°C (b), and 18°C (c) isopycnal surfaces at day 900 for Experiment DF-S. White areas indicate the isopycnal surface intersecting with the topographic slope or the surface. Lower panels are the corresponding time and zonal averaged PV fluxes. PV fluxes are calculated using snapshots between day 800 and 1000.

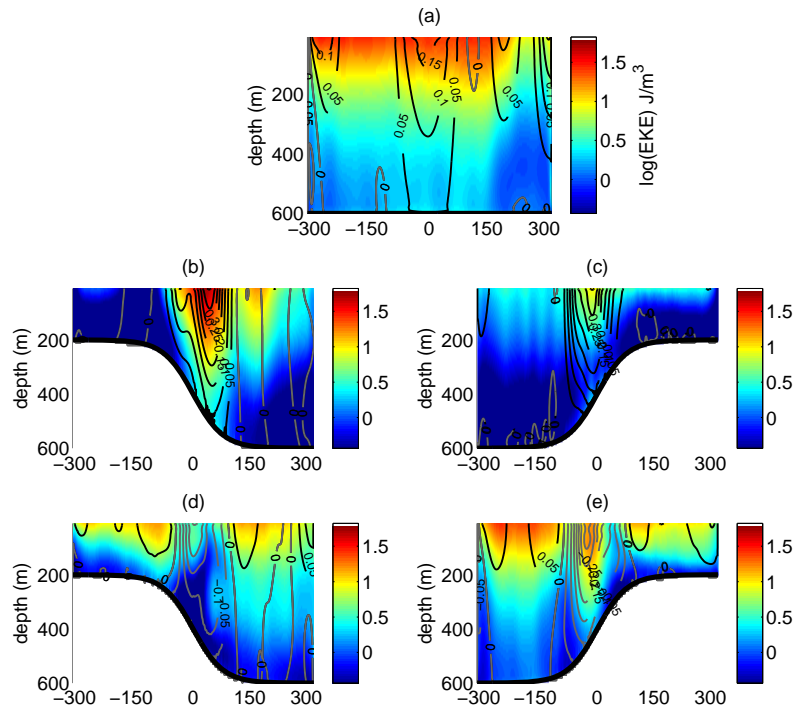


Figure 9: Zonal and time averaged EKE ($\rho(\mathbf{u}^2 + \mathbf{v}^2)/2$) from day 800 to 1000 for for five experiments. Values are displayed in \log_{10} scale. Contour lines show zonal and time averaged zonal velocity (\mathbf{u}). Black line represents positive values. Gray line represents negative values.

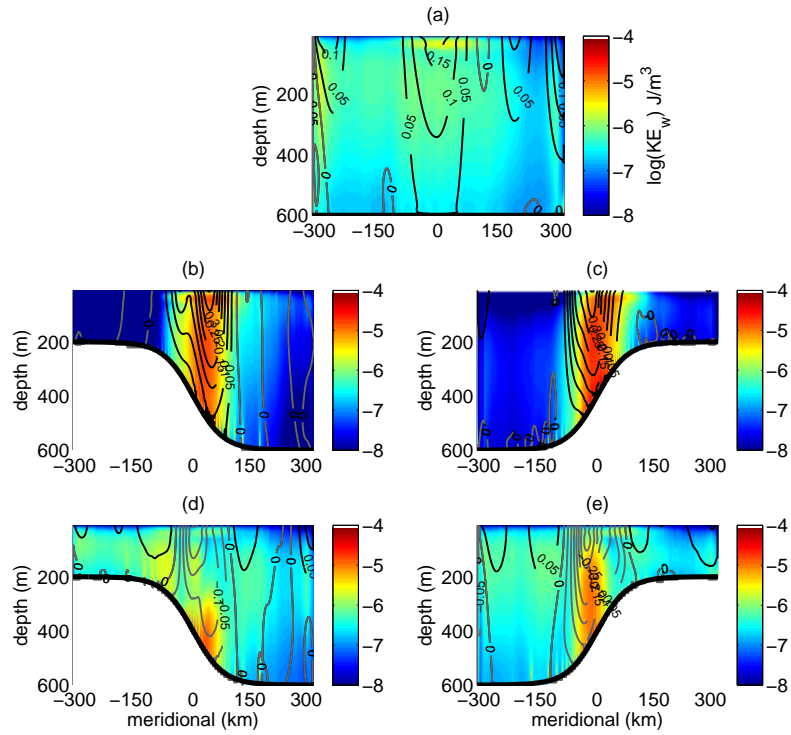


Figure 10: Zonal and time averaged vertical kinetic energy ($\rho \mathbf{w}^2/2$) from day 800 to 1000 for five experiments. Values are displayed in \log_{10} scale. Contour lines show zonal and time averaged zonal velocity (\mathbf{u}). Black line represents positive values. Gray line represents negative values.

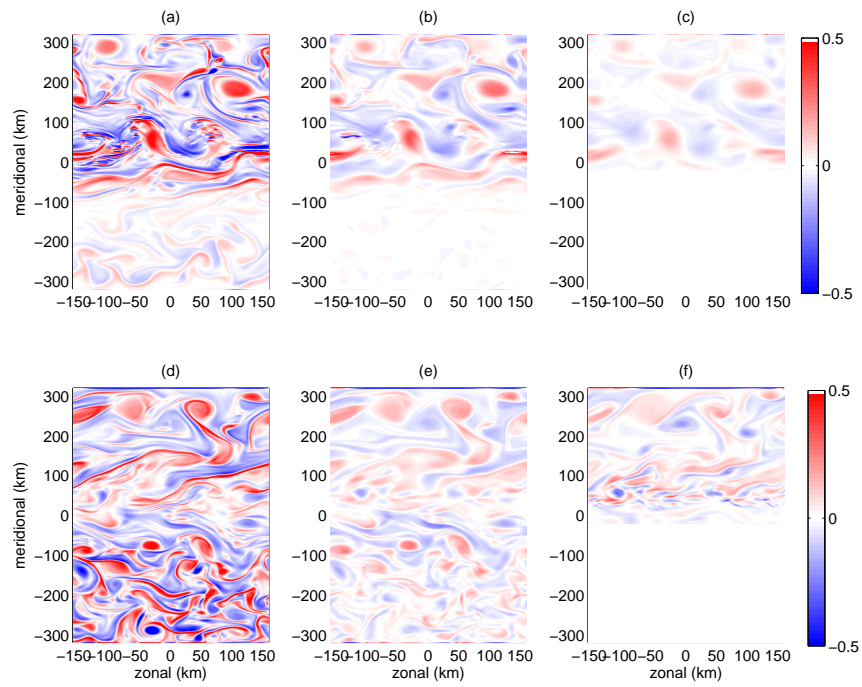


Figure 11: Vertical structure of Ro at day 900 for Experiment DF-S (a-c) and Experiment UF-S (d-f). Cross sections at 10m, 150m, and 300m depth are shown. White areas in (c) and (f) are associated with topographic slope interception.